



Three-Dimensional Printing of Neuron-inspired Structures by Direct Laser Writing

A thesis submitted in fulfilment of the requirements for the degree of Doctor of Philosophy

Haoyi Yu

Master's degree, School of Physics, Nankai University

Senior supervisor:

Distinguished Professor Min Gu – RMIT University

Associate Supervisor:

Dr. Qiming Zhang– RMIT University

School of Science

College of Science, Engineering and Health

RMIT University

June 2019

Dedicated to My Beloved Family.

Declaration

I, Haoyi Yu, certify that, except where due acknowledgement has been made, the work is that of the author alone; the work has not been submitted previously, in whole or in part, to qualify for any other academic award; the content of the thesis is the result of work that has been conducted since the official commencement date of the approved research program; any editorial work, paid or unpaid, carried out by a third party is acknowledged; and ethics procedures and guidelines have been followed.

The development of the hydrogel and the structures designed and fabricated in Figure 5.12 are provided by Dr. Haibo Ding.

Haoyi Yu

June 2019

Acknowledgements

I am grateful for getting a chance to acknowledge the people who helped me in my journey towards the completion of this degree.

My foremost thanks go to my senior supervisor Professor Min Gu for giving me the opportunity to work in a world-class facility and for constantly supporting me throughout my research study. He always has shown great enthusiasm for my research project and stood by me whenever I was stuck on problems. I appreciate the numerous conversations we had about my research project and the lessons he taught me about the real professionalism in research.

Thanks goes to my second supervisor, Dr. Qiming Zhang, who has helped me a lot during the past years. I also would like to express my sincere gratitude also to Dr. Ben Cumming, who introduced me to the wonderful world of three-dimensional direct laser writing system. Many thanks go to Dr. Zengji Yue for teaching me his experience in becoming a PhD researcher. I would like to thank the Royal Melbourne Institute of Technology (RMIT) University for providing me the amazing environment for my research.

Especially, I would like to thank Mr. Simone Lamon for spending a lot of time together during the past years. I have been enjoying every day with his company and I look forward to many more days together.

Finally, I would express my unconditional gratefulness to my parents and my brother.

Haoyi Yu

June 2019, Melbourne, Australia

Table of Contents

Declaration	i
Acknowledgements	iii
Table of Contents	v
List of Figures	ix
List of Tables	xv
List of Abbreviations	xvii
Abstract	xix
Chapter 1: Introduction	1
1.1 Background	1
1.2 Objectives of this PhD Project	5
1.3 Organisation of the Thesis	7
Chapter 2: Literature Review	11
2.1 Introduction	11
2.2 Review of the Structural Features of Biological Neural Networks	12
2.3 Review of Neuron-inspired Structures.....	13
2.3.1 Neuron-inspired structures in two dimensions	13
2.3.2 Neuron-inspired structures in three dimensions	15
2.3.3 Materials for building neuron-inspired structures.....	16
2.4 Biomimetic Design	18
2.4.1 Introduction.....	19
2.4.2 Design principles of biomimetic structures	19

2.5 Three-dimensional Direct Laser Writing	23
2.5.1 Introduction.....	23
2.5.2 Principles of three-dimensional direct laser writing	24
2.5.3 Schemes of three-dimensional direct laser writing	26
2.5.4 Practical constraints of three-dimensional direct laser writing.....	27
2.5.5 Recent developments in three-dimensional direct laser writing	29
2.5.6 3D DLW of bioinspired microstructures	34
2.6 Summary	35
 Chapter 3: Three-dimensional Direct Laser Writing of Biomimetic Neuron	
Structures.....	37
3.1 Introduction.....	37
3.2 Concept of Three-dimensional Direct Laser Writing of Biomimetic Neuron Structures.....	38
3.3 Branch Features of Individual Neurons	39
3.4 Challenges in Fabricating 3D Biomimetic Neuron Structures Using 3D DLW	40
3.5 Influence of Fabrication Conditions on Fabrication Feature Size in 3D DLW	41
3.6 Influence of Fabrication Conditions on the Stability of 3D Biomimetic Structures in 3D DLW.....	44
3.6.1 Branch model	45
3.6.2 Influence of elastic-capillary force in fabricating a single branch structure	46
3.6.3 Quantitative study of the stability of single branch structures.....	48
3.6.4 Fabrication of multiple branch structures	50
3.7 Fabrication of Biomimetic Neuron-tracing Structures	51
3.8 Optical Characterisation of Biomimetic Neuron-tracing Structures.....	52
3.9 Experimental Set Up	54
3.10 Conclusion	55

Chapter 4: Three-dimensional Direct Laser Writing of Ultralow-density Neuron-inspired Steiner Tree Structures	57
4.1 Introduction.....	57
4.2 Neuron-inspired Steiner Tree Structures.....	59
4.2.1 Shortest connection distance in biological neural networks	59
4.2.2 History of Steiner tree structures	59
4.2.3 Analytical calculation of relative density of a 3D Steiner tree structure	61
4.3 Galvo-dithering Direct Laser Writing.....	63
4.4 Fabrication of 3D Neuron-inspired Steiner Structures Using Galvo-dithering 3D DLW	65
4.4.1 Standard process of fabrication of 3D microstructures using DLW.....	66
4.4.2 Fabrication path design	67
4.4.3 Fabrication results	68
4.5 Characterisation of Mechanical Properties of 3D Steiner Tree Structures	71
4.5.1 Theoretical discussion of mechanical properties of Steiner tree structures.....	72
4.5.2 Theoretical discussion of the rigidity of Steiner tree structures	73
4.5.3 Finite element simulation of the Young's modulus of Steiner tree structures.....	74
4.5.4 Experimental characterisation of Steiner tree structures	76
4.5.5 Comparison between experimental results and FEM simulation	80
4.6 Conclusion	82
Chapter 5: Design, Fabrication and Characterisation of Hydrogel Microstructures Using Three-dimensional Direct Laser Writing.....	85
5.1 Introduction.....	85
5.2 Selection of Photoinitiator and Hydrogel Precursors.....	86
5.2.1 Selection and characterisation of photoinitiators	87
5.2.2 Selection of hydrogel precursors	89
5.3 Biocompatible Hydrogel Synthesis.....	91
5.4 Two-photon Polymerisation Process	92
5.5 Experimental Confirmation of Two-photon Polymerisation	92
5.6 Characterisation of Mechanical Property of HMPP + PEGDA Hydrogel.....	95

5.7 Characterisation of Swelling Property of HMPP + PEGDA Hydrogel	97
5.7.1 Swelling behaviour of hydrogel.....	97
5.7.2 Design of reversible ‘octagon to square’ structure	98
5.7.3 Fabrication of reversible ‘octagon to square’ microstructures using 3D direct laser writing	99
5.7.4 Fabrication results	100
5.7.5 Characterisation of the swelling behaviour of HMPP + PEGDA hydrogel.....	102
5.8 Fabrication of Neuron-inspired Fractal Tree Structures	104
5.8.1 Design and fabrication of neuron-inspired fractal tree model	104
5.8.2 Fabrication results.....	106
5.9 Conclusion	107
Chapter 6: Conclusions	109
6.1 Thesis Conclusions	109
6.2 Future Outlook	112
6.2.1 Three-dimensional direct laser writing for large-scale fabrication of neuron-inspired structures	112
6.2.2 Enhancing the mechanical properties of Steiner tree microstructures at the ultralow-density scale	114
6.2.3 Developing a hydrogel material for two-beam super-resolution direct laser writing	116
6.3 Summary	116
Appendix A: Synthesis of the Zirconium-based Organic–inorganic Photoresist	117
Appendix B: Mechanical Characterisation of Zirconium-based Photoresist	118
Appendix C: Properties of Low-density 3D Microstructures.....	120
References.....	123

List of Figures

Figure 1.1: Examples of 2D and 3D neuron-inspired structures fabricated by different methods.....	2
Figure 1.2: Photon polymerisation techniques.....	4
Figure 1.3: Concept of the thesis.	7
Figure 2.1: Illustration of multiple scales of structural features of BNNs.....	12
Figure 2.2: 2D neuron-inspired structures fabricated by different techniques.	13
Figure 2.3: Nature-inspired 2D microstructures for neuron tissue engineering.	15
Figure 2.4: A modular design of bioengineered brain-like cortical tissues fabricated by 3D additive printing in []......	16
Figure 2.5: Nature as a model.	20
Figure 2.6: Nature as a mentor and nature-inspired low-density structures from mathematically defined ‘minimal surface’.....	21
Figure 2.7: Various microstructures fabricated using 3D DLW for different application purposes.	23
Figure 2.8: Diagrams showing the principle of 3D DLW based on two-photon polymerisation (TPP).	24
Figure 2.9: Two schemes of 3D DLW.....	27
Figure 2.10: Two-beam super-resolution photoinduction-inhibited nanolithography (SPIN).	30
Figure 2.11: Two-photon fabrication technique in inorganic materials.	32
Figure 2.12: 3D Biocompatible PEGDA hydrogel structures fabricated by 3D DLW. SEM image of a 3D PEGDA hydrogel scaffold colonised by neuron cells [153]......	33
Figure 2.13: Bioinspired microstructures fabricated by 3D DLW.	35
Figure 3.1: Concept of 3D DLW of biomimetic neuron structures.	38
Figure 3.2: The branch tree of biological neurons and the morphological represented model in micromorphology research.	39

Figure 3.3: Two-photon fabrication linewidth as a function of laser power and the top view of the SEM images of suspended polymer lines fabricated at constant writing speed of 10 $\mu\text{m/s}$ with laser power ranging from 0.50 mW to 4.50 mW.....	42
Figure 3.4: Two-photon fabrication linewidth as function of writing speed and the top view of the SEM images of suspended polymer lines fabricated at a constant laser power of 1 mW with the writing speed ranging from 5 $\mu\text{m/s}$ to 50 $\mu\text{m/s}$	43
Figure 3.5: Branch models inspired by biological neurons.	45
Figure 3.6: Illustration of the elastic-capillary behaviour of single branch structures.	46
Figure 3.7: Quantitative study of the deformation behaviour of single branch structures fabricated by 3D DLW.	48
Figure 3.8: Quantitative study on critical boundary of single branch structures with different branch angles as a function of laser power and writing speed.	49
Figure 3.9: Fabrication results of multiple branch structures with different branching angles.....	50
Figure 3.10: Fabrication results of biomimetic neuron structures with different average branching angles.	51
Figure 3.11: Synthesis of fluorescent photoresist (Rhodamine 6G added into zirconium-based photoresist).	52
Figure 3.12: Confocal fluorescent microscope images of biomimetic neuron-tracing structures obtained using a Nikon confocal microscope.....	53
Figure 3.13: Experimental set up for our 3D DLW system.	54
Figure 4.1: 2D minimum Steiner tree (left) and a solution to the Fermat–Torricelli problem (right) for a set of four points $N = [a, b, c, d]$ on a unit square.	59
Figure 4.2: 3D Steiner tree structure connecting eight points calculated using the algorithm from reference [102].	61
Figure 4.3: Analytical comparison of the relative densities between a 3D Steiner tree structure and other well-known lattice structures as a function of beam diameter.	62

Figure 4.4: Schematic diagrams showing the writing voxel formation process in galvo-dithering DLW using circular dithered correction applied by galvo mirrors.	63
Figure 4.5: Effect of galvo-dithering diameters on fabrication linewidth in the x-y plane.	64
Figure 4.6: Microstructure fabrication process.	66
Figure 4.7: Design of fabrication path for the Steiner tree structure (viewed from an oblique angle).	67
Figure 4.8: Fabrication results showing SEM images of Steiner tree networks without and with galvo-dithering.	68
Figure 4.9: SEM image of Steiner tree structures fabricated by 3D DLW with galvo-dithering in the zirconium photoresist, showing the advantageous influence of galvo-dithering in reducing the shrinkage effect.	69
Figure 4.10: SEM image of Steiner tree structures in the zirconium photoresist demonstrating the advantageous influence of galvo-dithering on the reduction of fabrication feature size.	70
Figure 4.11: Fabrication results of Steiner tree structures with different relative densities.	71
Figure 4.12: Simplified 5×1 unit structure modelled by Solidworks used in FEM and illustration of the simulation set up of the force and constraint on the simplified 5×1 unit structure.	74
Figure 4.13: Finite element analysis of a 5×1 simplified structure with the beam diameter of 430 nm with relative density of 15%.	75
Figure 4.14: Illustration of the measurement of Steiner tree microstructures.	77
Figure 4.15: Experimental characterisation results of microstructures.	78
Figure 4.16: Measured Young's modulus of Steiner tree microstructures as a function of relative density.	81
Figure 4.17: Yield strength of fabricated 3D Steiner tree microstructures as a function of relative density.	82
Figure 5.1: Absorption spectrum of photoinitiator HMPP measured using a UV-visible spectrometer.	88

Figure 5.2: Illustration of the measurement of two-photon cross-section using the Z-scan method.	88
Figure 5.3: Diagram showing components and volume ratio in synthesising HMPP + PEGDA hydrogel.	91
Figure 5.4: Illustration of TPP process in HMPP + PEGDA hydrogel.	92
Figure 5.5: Experimental confirmation of the fabrication conditions of the HMPP + PEGDA hydrogel.	93
Figure 5.6: Optical images of fabricated woodpile structures with different periods in air to confirm optimal fabrication conditions for the HMPP + PEGDA hydrogel.	94
Figure 5.7: Illustration of the measurement of hardness of the HMPP + PEGDA hydrogel using nanoindentation.	95
Figure 5.8: Measured hardness of PEGDA hydrogel as a function of laser power in air.	96
Figure 5.9: Representation of hydrogel stimuli responsive swelling and unswollen with water content.	97
Figure 5.10: Design of ‘octagon to square’ reversible structure.	98
Figure 5.11: Design and fabrication of reversible ‘octagon to square’ microstructures.	99
Figure 5.12: Transmissive optical images of reversible shaped microstructures fabricated by 3D DLW.	100
Figure 5.13: Quantitative study of reversible behaviours of ‘octagon to square’ microstructures fabricated by 3D DLW.	101
Figure 5.14: Shrinking and swelling behaviour of the PEGDA hydrogel.	103
Figure 5.15: Diagrams showing the design of neuron-inspired fractal structures.	104
Figure 5.16: Design and fabrication results of neuron-inspired fractal structures.	106
Figure 6.1: Illustration to fabricate Steiner tree structures with ultralow-density using SPIN lithography.	115
Figure B.1: Illustration of fabrication and measurement of the Young’s modulus of the photoresist.	118
Figure B.2: The influence of laser parameters on the Young’s modulus of the organic–inorganic photoresists in air.	119

Figure C.1: Four typical low-density lattice structures..... 120

List of Tables

Table 1.1: Comparison between the performances of the different fabrication techniques used in manufacturing neuron-inspired structures.	3
Table 2.1: Materials applied for building neuron-inspired structures.....	17
Table 2.2: Comparative analysis of various photoinitiators in water solubility and biocompatibility.	34
Table 4.1: FEM simulation results of the Young's modulus of the microstructures ...	76
Table 4.2: Obtained Young's modulus and yield strength data from compression test for 3D Steiner tree microstructures with different relative densities.....	79
Table C.1: Summary of the scaling constant (m and n) and proportionality constants (B and C) of the Young's modulus and the yield strength scaling relationships respectively for each lattice structure made of polymers.	121
Table C.2: Summary of the mathematical formulas of relative densities of different lattice structures.....	122

List of Abbreviations

1D	One-dimensional
2D	Two-dimensional
3D	Three-dimensional
BNNs	Biological neural networks
EBL	Electron beam lithography
W	Unit cell size
t	Beam diameter
ALD	Atomic layer deposition
DLW	Direct laser writing
fs	Femtosecond
nm	Nanometre
μm	Micrometre
MHz	Mega Hertz
A	Galvo-dithering amplitude
D	Galvo-dithering diameter
GD-DLW	Galvo-dithering direct laser writing
I	Photoinitiator
I*	Intermediate state of the photoinitiator
IC	Integrated circuit
L	Length
LBL	Layer-by-layer
M	Monomer
Q*	Quencher
R*	Radical
n	Refractive index
NA	Numerical aperture
OA	Optical activity

P	Laser power
s	Writing speed
mW	Micro watt
SEM	Scanning electron microscope
TPA	Two-photon absorption
TPP	Two-photon polymerization
UV	Ultraviolet
HMPP	2-hydroxy-2-methylpropiophenone
PEGDA	Poly (ethylene glycol) diacrylate
E	Modulus
F	Force
GPa	Giga Pascal
MPa	Mega Pascal
Pa	Pascal
GM	Goeppert-Mayer ($10^{-50} \text{ cm}^4 \text{ s photon}^{-1}$)
AFM	Atomic force microscope
PDMS	Polydimethylsiloxane
PEG	Poly (ethylene glycol)

Abstract

Neuron-inspired structures are 2D or 3D artificial structures that emulate the structural features in biological neural networks (BNNs). Due to their inherent varied characteristics, such as geometrical characteristics, mechanical properties and biocompatibility, these neuron-inspired structures not only provide structural supports and direct neuron shapes and affect neuron differentiation, migration and proliferation in the field of neuron tissue culturing but have proved to reflect their involvement in different neuron functional tasks in neuroelectronic interfacing applications and neuromorphic computing purposes.

The design, fabrication and characterisation of neuron-inspired structures has received considerable attention over the past decades, with many fabrication techniques, including electron beam lithography (EBL) and three-dimensional (3D) additive printing, utilised in fabrication of two-dimensional (2D) or 3D neuron-inspired structures.

In addition, future applications of neuron-inspired structures require development in the fabrication of 3D neuron-inspired structures at the sub-micrometre scale with high biocompatibility as well as emulation of the structural features in BNNs.

However, owing to the fact that BNNs possess extraordinary complexity and connectivity at the sub-micrometre scale in 3D space, traditional fabrication of neuron-inspired structures cannot emulate the complexity in BNNs. One reason is the constraints rooted in the fabrication technologies used in the fabrication of neuron-inspired structures, such as EBL, mask lithography and other recent developments in 3D fabrication techniques. These techniques are generally limited to fabrication in either 2D substrate or 3D space lacking resolution. Another reason is the lack of emulation of the structural features in BNNs. Neuron-inspired structures that have been fabricated are generally very simple, such as microholes or micro-grooves.

These structures cannot emulate geometrical features such as the branching structures in BNNs.

The solution lies in the combination of 3D direct laser writing (DLW), biomimetics and recently developed biocompatible hydrogel materials. 3D DLW based on two-photon absorption (TPA) is a cost-effective fabrication technique that can fabricate 3D arbitrary structures down to the 9 nm feature size. Biomimetics is a multidisciplinary field that has provided numerous solutions in the fields of physics, chemistry and engineering.

In this PhD project, we propose and demonstrate the use of 3D DLW to fabricate biomimetic neuron-inspired structures with a sub-micrometre feature size. In the main, we focus on four aspects of research:

1. discovery of unique structural features in BNNs networks and mathematical definition of the corresponding structures based on biomimetics
2. investigating the challenges in the fabrication of these structures and identifying solutions to tackle these challenges using 3D DLW
3. understanding the relationship between structure and properties (such as mechanical properties) based on experimental and theoretical study, revealing the physics principles and underlying mechanisms
4. developing a biocompatible photosensitive material suitable for 3D DLW.

3D biomimetic neuron-tracing structures can be directly fabricated using 3D DLW with a sub-micrometre feature size, tenfold smaller than biological counterparts. By introducing the mathematical model behind the elastic-capillary phenomenon, stable 3D biomimetic neuron-tracing structures can be fabricated by tuning fabrication conditions such as laser power and writing speed. This work solves the fabrication challenge faced in the fabrication of 3D neuron-tracing structures at the sub-micrometre scale.

Inspired by the mathematical formula for the ‘shortest connection distance’ in BNNs, biomimetic 3D Steiner tree microstructures were introduced and fabricated using galvo-dithering DLW. The mechanical properties of the fabricated 3D Steiner tree microstructures are theoretically and experimentally studied, and the power-law scaling relationships between relative density and Young’s modulus / yield strength confirmed. 3D Steiner tree microstructures have the smallest relative density compared with traditional low-density structures, rendering them potential candidates in many fields, including biomedical engineering and mechanical metamaterials.

A novel biocompatible hydrogel suitable for 3D DLW for future applications in biomedical science was developed. Demonstration of the properties of our selected components were performed using z-scan methods. The range of the Young’s modulus of the hydrogel material was studied by fabricating hydrogel microcubic structures with different laser powers. Further experimental fabrication and theoretical study showed the reversibility of the hydrogel microstructures resulted from the swelling and shrinking effect of hydrogels. A series of neuron-inspired fractal tree structures were fabricated using optimised conditions in the hydrogel. This chapter demonstrated the properties of the biocompatible hydrogel for 3D DLW.

Chapter 1: Introduction

1.1 Background

Since the early 21st century, there has been ongoing interest in brain science, resulting in several nation-wide brain projects, such as BRAIN initiative in USA [1], Human Brain Project in European Union [2], Brain/MINDS project in Japan [3], the China Brain Project [4] and the Australian Brain Alliance [5].

As one of the research fields among these brain projects, design, fabrication, and characterisation of neuron-inspired structures mimicking the structural features in biological neural networks (BNNs) has been an active area over the last decades [6].

Neuron-inspired structures are two-dimensional (2D) or three-dimensional (3D) structures that emulate the structural features in BNNs. In line with the varied characteristics of these structures, such as geometrical characteristics, mechanical properties and biocompatibility, these neuron-inspired structures not only provide structural supports [7] and direct neuron shapes [8], and affect neuron differentiation [9], migration and proliferation [10-12] in the field of neuron tissue engineering, but reflect their involvement in different neuron functional tasks [13] in neuroelectronic interfacing [14] and neuromorphic computing systems [15], among others. Several examples of 2D and 3D neuron-inspired structures are shown in Figure 1.1.

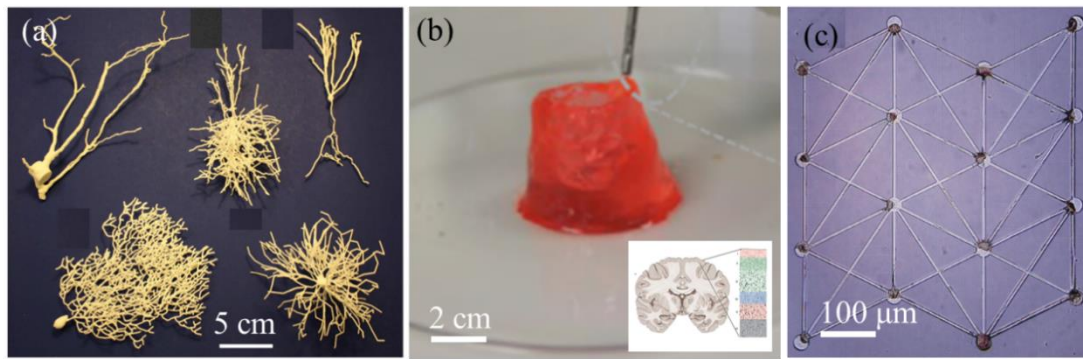


Figure 1.1: Examples of 2D and 3D neuron-inspired structures fabricated by different methods. (a) Visualisation of neuron structures using 3D additive printing [16], scale bar is 5 cm. (b) Brain-like structures fabricated using 3D ink jet printing, scale bar is 2 cm. (c) A typical 2D neuron-inspired structure fabricated on a silicon chip, scale bar is 100 μm .

To date, as shown in Table 1.1, the methodologies employed to manufacture neuron-inspired structures include 2D and 3D fabrication techniques. Traditional fabrication techniques, such as electron beam lithography (EBL) and ultra-violet (UV) mask lithography, despite drawing on a wide range of materials and nanometre feature size [17], lack the possibility to create true 3D architectures, leaving the neuron-inspired structures on 2D surfaces. While those platforms attempt to mimic the *in vivo* environment, they do not truly resemble the three-dimensional (3D) microstructure of neuronal tissues. Development of an accurate *in vitro* model of the brain remains a significant obstacle to our understanding of the functioning of the brain at the tissue or organ level.

The recent development of 3D additive printing, also called ‘ink jet printing’, has been shown capable of fabricating neuron-inspired structures in 3D space, with many biocompatible materials used in building 3D large-scale neuron-inspired structures [18]. Different from 2D structures, 3D neuron-inspired structures could be able to recapitulate the environment in. However, the resolution of this technique is limited to the millimetre size.

More recently, increasing interest has been devoted to fabricating 3D neuron-inspired structures using 3D light-assisted photopolymerisation techniques [19], such as stereolithography (SLA), selective laser sintering and digital light projection, where the 3D structures are realised by exploiting a layer-by-layer approach from a series of

transverse-plane image slices. However, these approaches can reach a resolution of only a few micrometres, and there is a more limited availability of materials capable of featuring biocompatibility and photosensitive properties simultaneously [20].

Table 1.1: Comparison between the performances of the different fabrication techniques used in manufacturing neuron-inspired structures.

Dimension	Techniques	Minimum feature size	Available Materials	Fabrication method
2D	Electron beam Lithography [17]	<20 nm	Polymers, metals, semiconductor	Point by point
	UV mask Lithography[19]	25 μm	Polymers, metals, semiconductor	Layer by layer
3D	Stereolithography [19]	100 μm	Polymers	Layer by layer
	Digital light projection [20]	25 μm	Polymers	Layer by layer
	3D additive printing [18]	0.5 mm	Polymers, hydrogels	Point by point
	3D direct laser writing [23] based on TPP	9 nm	Polymers, hydrogels	Point by point

However, because BNNs possess extraordinary connectivity and complexity in 3D space at the sub-micrometre scale [21], previous neuron-inspired structures fabricated by these techniques are either limited to a 2D surface or lack resolution in 3D space, and most are generally very simple 2D structures, such as microholes, micro-cages, micro-grooves, woodpile structures or random large-scale structures in 3D. These 2D or 3D structures do not represent the structural complexity of BNNs.

This has prompted discussion on the fabrication of ideal neuron-inspired structures [22], which requires innovation in fabricating 3D neuron-inspired structures at the sub-micrometre scale from three aspects:

1. Neuron-inspired structures should have 3D features that emulate the structural features of BNNs at the micrometre scale.
2. Neuron-inspired structures should provide tuneable mechanical properties ranging from several Pa to several GPa.

3. Neuron-inspired structures should be biocompatible.

As shown in Table 1.1, among fabrication techniques, 3D direct laser writing (DLW) based on two-photon absorption (TPA) [23] is attracting interest because it is a promising and versatile tool in fabricating precise and arbitrary 3D structures with a sub-micrometre feature size (see Figure 1.2b). Most importantly, 3D DLW is the only method that can fabricate 3D neuron-inspired structures at the sub-micrometre scale.

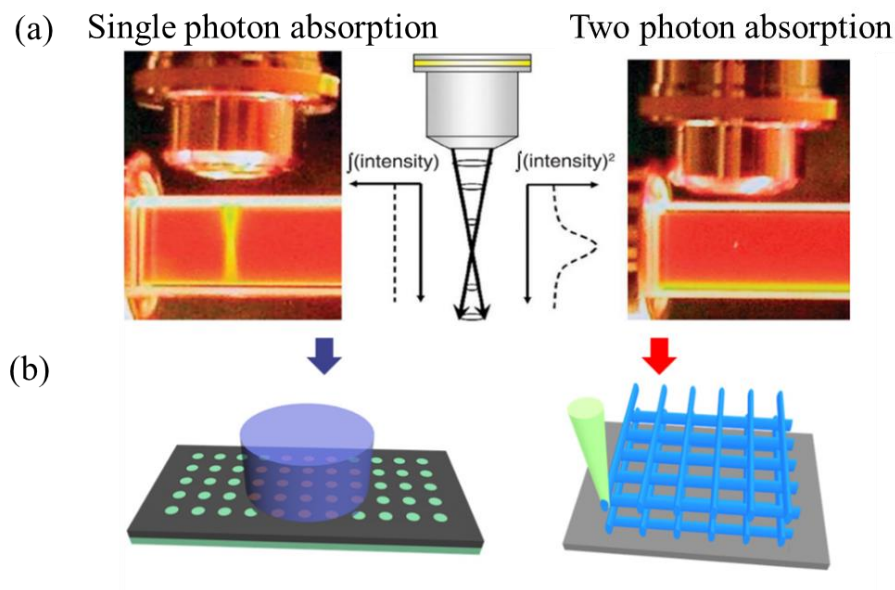


Figure 1.2: Photon polymerisation techniques. (a) Experimental figures showing single-photon absorption and TPA [24, 25]. (b) Schematic diagram showing single-photon polymerisation and two-photon polymerisation.

3D DLW based on TPA [26, 27] employs a femtosecond laser source that is able to pass through a transparent photosensitive material (transparent to the wavelength that is used and highly absorptive at corresponding wavelength) where, by controlling the direction of the laser beam and/or using a motorised stage, it is possible to ‘write’ directly inside the material in extremely confined regions (hundreds of nanometres) called voxels. Development of 3D DLW has offered many solutions in varied fields, such as photonics [28], biomedical science [29], solar energy [30] and optical data storage [31].

Apart from the advantage of high fabrication resolution in 3D space, 3D DLW also embraces a wide range of photosensitive materials, which can be used in 3D DLW for

different applications, such as dedicated polymers [32,33], composite materials [34] and biocompatible materials [35].

Recent research utilising 3D DLW in building biomimetic structures includes red cell structures [36] and gecko feet structures [37]. However, none of these focus on emulating the complexity structures in BNNs in brain science. Therefore, there is an urgent need to introduce novel models in 3D DLW to fabricate 3D neuron-inspired structures at the sub-micrometre scale.

1.2 Objectives of this PhD Project

The objectives of this PhD project can be summarised into four aspects:

1. Discovery of unique structural features in BNNs and mathematically defining the corresponding structures
2. Identifying the challenges in the fabrication of these structures and finding solutions to tackle these using 3D DLW
3. Exploring the relationship between structure and properties (such as mechanical properties) based on experimental and theoretical study, to reveal the physics principles and underlying mechanisms
4. Developing a biocompatible material suitable for 3D DLW.

The first motivation is to introduce ‘biomimetic design’ in neuron-inspired structures. Biomimetic designs have recently received special attention because of their reported adaptability in a wide range of applications [38]. The internal structures in BNNs possess high complexity and connectivity, such as dendritic branch angles, branch lengths and branch diameters from the millimetre down to the nanometre scale [39]; these are given particular attention in this thesis for their potential in the design of biomimetic neuron-inspired structures. Several novel neuron-inspired biomimetic designs are introduced in each chapter.

The second motivation of this PhD project is to fabricate 3D neuron-inspired structures at the sub-micrometre scale that emulate the structural features in BNNs based on the 3D DLW technique, by making use of the fundamental understanding of light–matter interactions under different fabrication conditions, such as laser power and writing speed in photosensitive polymers and hydrogels. As the interaction of laser beams with photosensitive materials is highly dependent on the conditions used for the irradiation, it is the intent of this thesis to undertake a thorough investigation into the influence of the different physical phenomena involved in the polymerisation process as accessed by studies in the laser fabrication process, such as writing speed, laser power, feature size and mechanical properties.

Another motivation of this thesis is to study the mechanical properties of neuron-inspired structures fabricated by 3D DLW at the sub-micrometre scale. When the feature size of microstructures decreases to the sub-micrometre scale, gravitational force is negligible compared with capillary force and elastic strength of the microstructures [40]. This size effect is a critical factor in determining the mechanical stability of microstructures during the developing process in 3D DLW.

In addition, size effect also has a major impact on the mechanical performance of neuron-inspired structures at the sub-micrometre scale [41]. When the feature sizes of structures reduce to micrometre or nanometre scales, the mechanical properties of these structures will undergo a size-affected transition. These properties include the power-law scaling relationship among low-density microstructures [42], which is a prevalent feature in biological materials. The mechanical properties of these structure can be enhanced due to the size effect, such as Young's modulus, stiffness, and yield strength. Therefore, it is necessary to investigate mechanical properties, such as Young's modulus and yield strength of neuron-inspired structures fabricated by 3D DLW at different scales.

Moreover, further studies in this thesis focus on developing a biocompatible hydrogel suitable for 3D DLW, which can fulfil the requirement of future applications of 3D DLW in biomedical science, and a detailed analysis to characterise the properties of our hydrogel material specially designed for 3D DLW is performed.

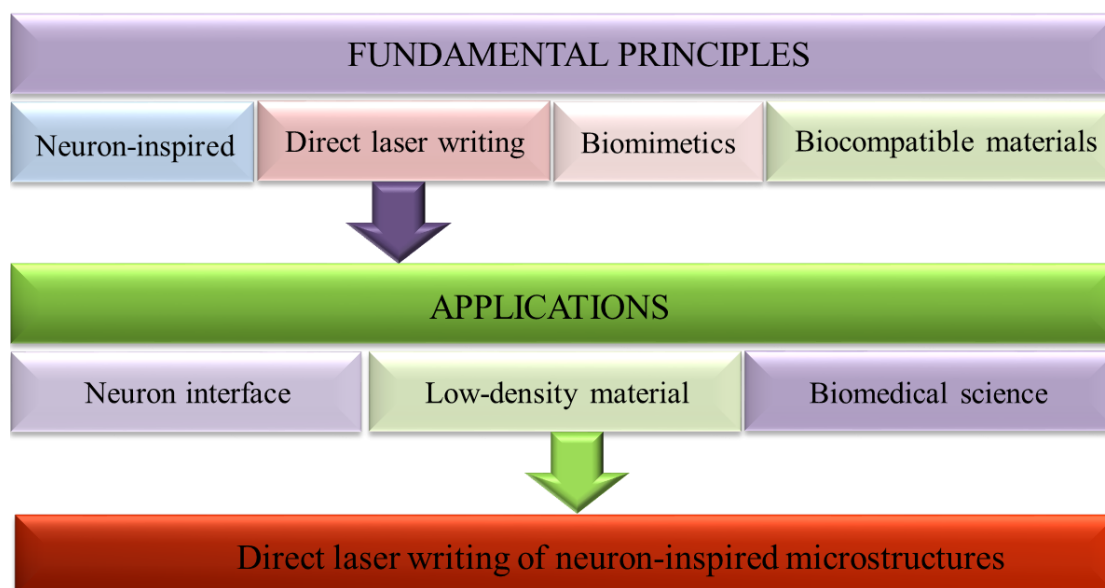


Figure 1.3: Concept of the thesis.

In summary, the concept of the thesis is shown in the flow chart in Figure 1.3. By combining the fundamental principles of 3D DLW, biomimetic design and neuron-inspired structures, the research work conducted in this thesis demonstrates that 3D DLW is a powerful tool for fabricating neuron-inspired structures at the micrometre scale. The knowledge obtained is of great potential for future applications in many fields, such as biomedical engineering, biomimetic design for low-density materials and future applications in biomedical engineering.

1.3 Organisation of the Thesis

The research work presented in this thesis explores both theoretically and experimentally the fabrication of neuron-inspired structures using 3D DLW. Three main research projects are presented.

Before beginning the main body of the thesis, a review of the major works related to neuron-inspired structures and biomimetic design is provided in Chapter 2. Detailed review and discussion of 2D and 3D neuron-inspired structures is presented in Sections 2.2 and 2.3, to develop an understanding of the application of neuron-inspired structures in different communities. Section 2.4 offers a discussion on biomimetic designs. Two principles of biomimetic design adopted in scientific research related to 3D DLW are discussed in this section, with a focus on ‘nature as

model' and 'nature as a mentor'. The basics, practical limitations of and recent developments in the 3D DLW technique are discussed in Section 2.5.

The fabrication conditions used during laser fabrication not only affect the fabrication feature size of the 3D neuron-inspired structure, but also have a crucial influence on the mechanical stability of neuron-inspired structures through the drying process after the laser fabrication. Chapter 3 performs a detailed study to understand the mechanism behind the phenomenon by introducing a novel mathematical model to describe the capillary force effect. Section 3.1 discusses the concept of the project, in which BNNs are directly used as biomimetic models. Section 3.2 discusses the effect of fabrication conditions on feature size in 3D DLW. Section 3.3 introduces a branching model to describe the capillary effect during the developing process. Section 3.4 argues that branching structures can be fabricated under optimised fabrication conditions, and that several 3D biomimetic structures can be fabricated. Characterisation of the fabricated structures is performed using a scanning electron microscope (SEM) and an optical fluorescent microscope.

In Chapter 4, BNNs are introduced as a mentor. A novel biomimetic design is introduced, inspired by the 'shortest connection distance' in biological neurons. The history of Steiner tree structures and the relationship between the structural features of BNNs are discussed in Sections 4.1 and 4.2. An analytical discussion of the relative density of the Steiner tree structures is provided in Section 4.3. In Section 4.4, the influence of laser fabrication conditions, such as laser power (P), writing speed (s) and galvo-dithering) on the feature size, relative density and mechanical properties of microstructures are studied. The mechanical properties of the fabricated 3D Steiner tree microstructures are theoretically and experimentally studied in Sections 4.5 and 4.6. Section 4.7 compares the theoretical and experimental results. A conclusion for the chapter is given in Section 4.9.

Chapter 5 introduces a novel biocompatible hydrogel suitable for 3D DLW in future applications in biomedical science. Section 5.2 introduces the principles in the selection of the photoinitiator and hydrogel precursor. Section 5.3 demonstrates the properties of our selected components for the photosensitive hydrogel. Section 5.4

focuses on the confirmation and study of laser fabrication conditions by experimentally characterising the optimised laser power and writing speed. Section 5.5 concerns the demonstration and characterisation of the reversibility of the hydrogel microstructures fabricated by 3D DLW. Section 5.6 introduces a neuron-inspired fractal structure fabricated under optimised conditions. Section 5.7 concludes with a discussion of the characteristics of our novel biocompatible hydrogel.

The thesis concludes with Chapter 6, which summarises the work presented in the previous chapters. An outlook for future work related to this topic is provided, with three aspects nominated as potential future projects.

Chapter 2: Literature Review

2.1 Introduction

Design, fabrication and characterisation of neuron-inspired structures has been a very active research field over past decades. Neuron-inspired structures are 2D or 3D structures that emulate the structural features in BNNs. Much effort has been made to design, fabricate and characterise various kinds of neuron-inspired structures in different materials using different fabrication technologies. In this chapter, we first review the structural features of BNNs, and summarise recent developments in 2D and 3D neuron-inspired structures. In addition, biomimetic design is discussed in this chapter, because it has been widely investigated and studied for different applications in different fields, in line with the diversity and complexity of nature. Principles and practical limitations of and recent developments in 3D DLW are also discussed in this section.

2.2 Review of the Structural Features of Biological Neural Networks

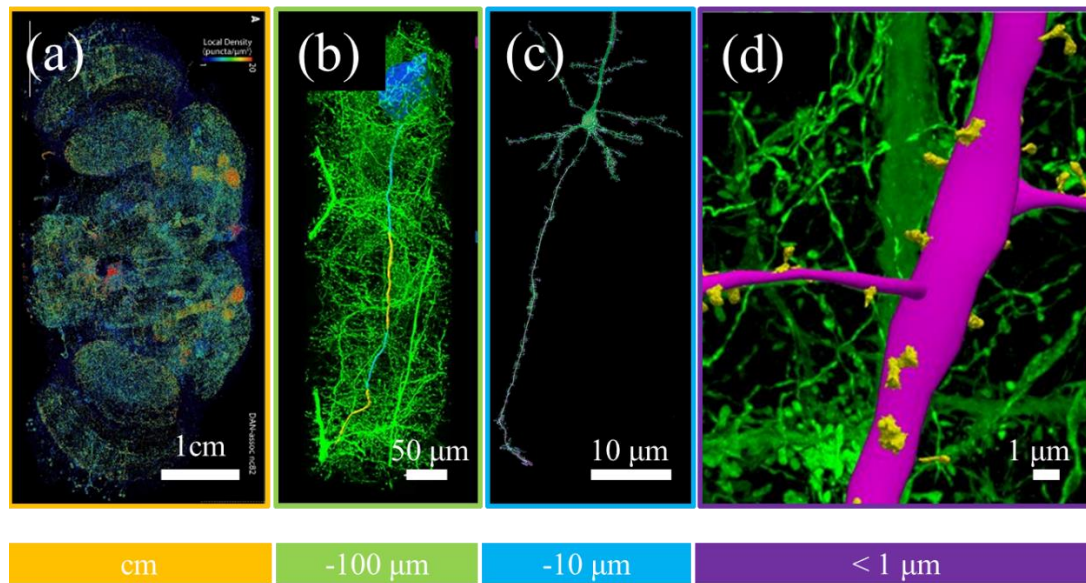


Figure 2.1: Illustration of multiple scales of structural features of BNNs. (a) The macroscale (mm^3): fluorescent image of brain regions and pathways. (b) The mesoscale: fluorescent image showing neuronal circuitry consisting of neurons connected with each other. (c) and (d) The microscale (nm - μm): fluorescent images of individual neurons and synapses.

The brain, also technically a BNN, is regarded as the information processing centre in animals [43]. It collects information, react towards the information and store the information as memory reference, therefore, various life can be possible. The first studies on structural features of BNNs were conducted in 1899 by a Spanish neuroscientist Santiago Ramon y Cajal [44]. Figure 2.1 (c) is a typical fluorescent image of a single neuron, which consists of multiple branch structures, called dendritic structures (axons and dendrites), made of membrane. Diameters of axons and dendrites range from several hundreds of nanometres to 2~5 micrometres [45].

BNNs are complex 3D network structures organised on multiple spatial scales [46]. Generally speaking, BNNs consist of millions of individual neurons connected to each other. Taking the human brain as an example, it consists of 10^{11} neurons, with each neuron connected to at least 10,000 other neurons through synapses. Typically, three scales of organisation may be distinguished (see Figure 2.1): from the macroscale to the mesoscale, and down microscale of single neurons and synapses. The scale ranges

from mm^3 (distinct brain areas) to μm^3 (neuronal circuit), and to nm scale (single neurons and synapses).

2.3 Review of Neuron-inspired Structures

2.3.1 Neuron-inspired structures in two dimensions

2D neuron-inspired microstructures were first introduced with the development of soft lithography or 2D fabrication techniques based on EBL or UV mask lithography. Many kinds of 2D structures have been designed and fabricated with different materials.

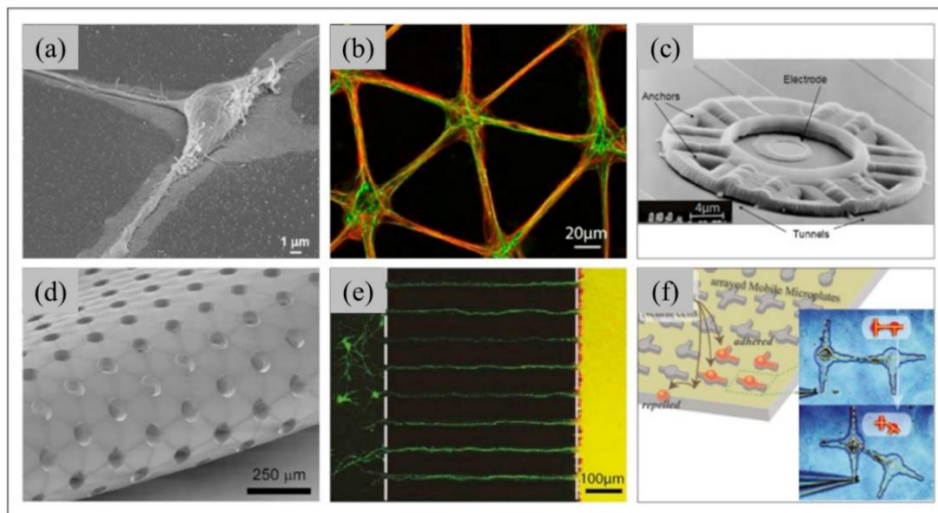


Figure 2.2: 2D neuron-inspired structures fabricated by different techniques. (a) SEM image of a single neuron on a pattern of extracellular matrix proteins deposited via microcontact printing [47]. (b) Fluorescent image of a triangle neuron network structure made of micro-holes providing an environment for neuron growth and neuron connection [48]. (c) Neuro-cage manufactured on an electrode [49]. (d) A PDMS network structure made of micro-holes [50]. (e) Micro-walls fabricated to polarise the growth of axons for microfluidic culture platform [50]. (f) Microplates structures fabricated in constructing arbitrary neuronal networks [51].

The most frequently used neuron-inspired structures are micro-holes, micro-grooves, openings and wells. These structures can be etched into a 2D substrate [52] with different connection patterns. A triangle neuron network of micro-holes with closest neighbour interconnections has been manufactured using mask lithography [53] to entrap neurons and guide their neurite growth. With structures such as micro-holes

[54], immobilisation of neuron cells can be achieved using micro-tunnels. Examples are shown in Figure 2.2.

Other 2D microstructures such as barriers have also been fabricated and have proven very effective in neuron culturing for neural axonal connection repair, regeneration and transport with the help of microfluidic technologies [55]. Depending on the design of microfluidics, these 2D microstructures can also facilitate independent biochemical analyses of these components [47]. Single neurons can also be isolated at given spots with the help of these simple 2D microstructures [50]. In addition, these 2D microstructures can be fabricated with different degrees of roughness [49], or different shapes as physical barriers interconnecting larger components [50]. Unidirectional connections of biological neurons can also be achieved by tuning the compartment sizes [51]. Nanowires are a good candidate in providing better nutrient flow diffusion in the surrounding environment in neuron culturing. Such physical guidance of neuron growth can also be achieved using microplates [52].

Recent developments in neuron-inspired structures include those designed and fabricated by nature forms, such as the vein structure in leaves [56] (see Figure 2.3). Recent work [57] focuses on design and fabrication of multichannel microstructures inspired by other natural structures such as kites, snow and stomachs. These microstructures are fabricated by micropatterning or micro-moulding, generally based on mask lithography. Even though these structures are complicated, they are generally limited to 2D substrates.

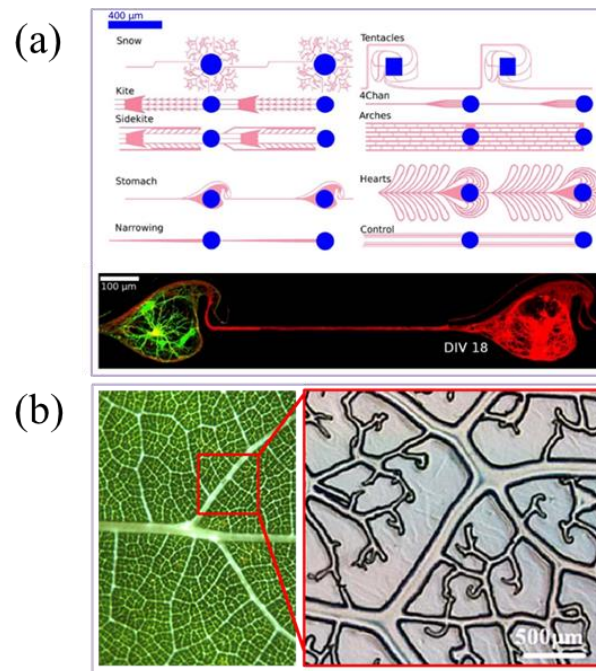


Figure 2.3: Nature-inspired 2D microstructures for neuron tissue engineering. (a) The 10 different PDMS channel structures investigated in [57]. Multichannel structures inspired by snow, kites, side kites, and so on, fabricated by EBL. (b) Perusable network structures in the hydrogels inspired by natural leaves [58], using micro-moulding or micropatterning technique based on UV mask lithography.

2.3.2 Neuron-inspired structures in three dimensions

As summarised above, traditional methods for fabricating neuron-inspired structures for neural tissue engineering are generally limited on 2D surfaces. One obvious disadvantage is that 3D spatial extensions of axons and dendrites during neuron tissue engineering could not be achieved. Consequently, the development of 3D fabrication techniques that facilitate 3D neuron-inspired structures is of great importance in mimicking the structural features in BNNs.

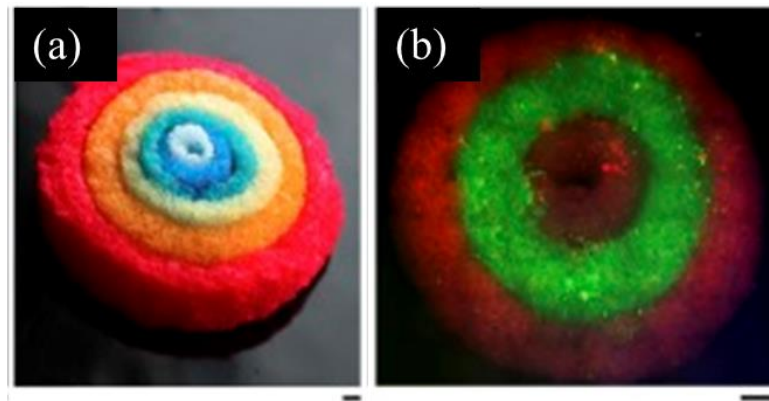


Figure 2.4: 3D additive printing of bioengineered brain-like cortical tissues fabricated in [58]. (a) 3D assembled tissue structures made of several concentrically doughnuts made of silk scaffolds dyed with food colour. Scale bar is 1 cm. (b) Fluorescent images of layered structures cultured with different primary rat cortical neurons, live-stained with DiI in red and DiO in green. Scale bar is 1.5 cm.

Recent developments in 3D additive printing techniques have demonstrated its great potential in building large-scale 3D neuron-inspired structures in the field of neuron tissue engineer (Figure 2.4 (a) and (b)). Hydrogel-made 3D brain-like structures consisting of primary neurons have been created with a peptide-modified biopolymer [59, 60]. This technique has been used for the creation of intricate functionalised 3D brain-like modulators formed from cortical tissue, kept alive for months *in vitro*. 3D architectures that compartmentalise biological tissues have also been achieved by 3D additive printing using silk-collagen protein scaffolds and hydrogels, which have then been used to build 3D brain-like tissue seeded with primary cortical neurons. One obvious disadvantage of these 3D neuron-inspired structures is that the connections between neurons are randomly patterned. The fabrication resolution of traditional 3D additive printing limits its capability to create 3D neuron-inspired structures with micrometre- or nanometre-scale resolution.

2.3.3 Materials for building neuron-inspired structures

This section presents a brief overview of new advances in biomaterials for building neuron-inspired structures for neuron tissue engineering. Materials that have been used in neural tissue engineering include organic or inorganic polymers; traditional inorganic nontoxic materials and natural materials (see Table 2.1). Generally, these materials focus on emulating the stiffness in BNNs, from several Pa to several GPa.

Comparisons of these materials across several factors are also shown in this table, such as biodegradability, mechanical strength (Young's modulus) and fabrication methods.

Table 2.1: Materials applied for building neuron-inspired structures.

Biomaterials	Biodegradable	Fabrication method	Mechanical strength
PDMS [62-66]	low	2D mask lithography/EBL	MPa
Silicon wafer [67-69]	no	EBL	GPa
PLA [70]	low	2D mask lithography	MPa
hydrogel [76,77]	high	2D mask lithography/3D DLW	Pa-kPa
Collagen gel [73,74]	high	3D additive printing	Pa-kPa
Gelatin [75]	high	3D additive printing	kPa
SU-8 polymer [71]	no	2D mask lithography/3D DLW	GPa
Parylene [72]	low	3D additive printing	kPa

Polydimethylsiloxane (PDMS) is the most widely used material in building neuron-inspired structures for neuron tissue engineering [61-64] due to its advantage of easy processing in fabrication and biocompatibility. Several works have been published using 2D lithography to fabricate PDMS microstructures to promote spatially resolved adhesion of neuron cells.

Nontoxic and inorganic materials such as silicon wafer [65-67] have been used to fabricate neuron networks with well-defined geometries on semiconductor substrates, enabling a non-invasive observation and detection of neuron activity at an individual neuron scale. These structures enabled the outgrowth of neurons and the formation of synapses inside structures fabricated by 2D mask lithography.

Photocurable polymers such as 4-arm photocurable poly-lactid acid (PLA) [68] and SU-8 [69] (a commonly used epoxy-based negative photoresist) are both used in

fabricating microstructures for neuron tissue engineering, such as micro wells and woodpile structures. Parylene [70] has also been used for the fabrication of microstructures in neuron tissue engineering.

Using 3D additive printing, collagen gel [71,72] was also used to build novel implantable devices to deliver a tethered aligned collagen guidance conduit containing Schwann cells into a peripheral nerve injury site. The advantage of collagen is that few people possess humeral immunity against it, and a simple serological test can verify if a patient is susceptible to an allergic reaction in response to this collagen-based biomaterial. Similar materials such as gelatine [73] can also be used in creating substrate for neuron tissue engineering. And, collagen can be easily obtained from mammals, such as rats, bovines and humans.

Biodegradable hydrogels [74,75] have attracted significant attention over the past five years because they have favourable characteristics for neuron tissue engineering, such as easiness in processing, a highly hydrated environment similar to that in biological cases for biological tissue growth, the ability to construct *in vivo*, and especially, recent development of fabricating hydrogel microstructures using 3D DLW. Many other properties are of great importance to the design of a hydrogel scaffolds, such as stimulus swelling, tuneable mechanical properties, and bio-degradation. These characteristics are a result from the crosslinked network structures of the hydrogel molecules, which can be tailored via adjusting the processing conditions during the fabrication process.

2.4 Biomimetic Design

As discussed in Chapter 1, novel models in designing of neuron-inspired structures are urgently required. The solution lies in the field of 'biomimetics'. Here, a discussion of biomimetic design is given, from which two important design principles can be generalised.

2.4.1 Introduction

Inspired by natural/biological solutions at macro and nanoscales, biomimetics is a multidisciplinary field that has given rise to new understanding of fundamental science and technologies. The primary goal of biomimetics is to conduct an in-depth understanding of the solutions and strategies that have evolved over time in nature and their potential implementations in science and technology practices. Therefore, the scope of biomimetics focuses on the design, fabrication and characterisation of nature-inspired structures for different application purposes.

In line with the diversity and complexity of nature, biomimetic design has been widely investigated and studied for applications in different fields, such as construction and architecture [76], structural materials [77], self-healing materials [78], surface science [79], nanophotonics [80], biomedical engineering [81], solar cell design [82] and energy storage [83]. For instance, the generation of colour in natural photonic crystals that reflect light at certain wavelengths can be found in various species, including butterfly wings [84]; the artificial replication of this biomimetic structure, called a 'gyroid' lattice, shows a circular dichroism in the near-UV wavelength region, shorter than that exists in the natural butterfly wings of *C. rubi*.

2.4.2 Design principles of biomimetic structures

Many review papers and articles discuss the propositions put forward to categorise the families and design principles of biomimetic structures. The first codification of biomimetic structures was introduced by Janine Benyus, a science writer and lecturer in environmental science. Her 1997 book entitled 'Biomimicry: Innovation Inspired by Nature' summarises recent findings in a variety of fields, from science to engineering, that could be traced to investigations into the designs and processes found in nature. A number of propositions are put forth in the book to effectively illustrate the current trends and principles of biomimetic structures and related research fields.

In general, the design of biomimetic structures must incorporate knowledge of features of natural forms. There are generally two design principles that have been widely used in the design of biomimetic structures [85,86]:

- *Nature as a model*: Biomimicry is a science that studies the models in nature and emulates or takes inspiration from their designs and processes to solve human problems.
- *Nature as a mentor*: Biomimicry is also a novel way of viewing and valuing nature, based not only on what we can extract from the natural world, but also on what we can learn from it.

2.4.2.1 Nature as a model

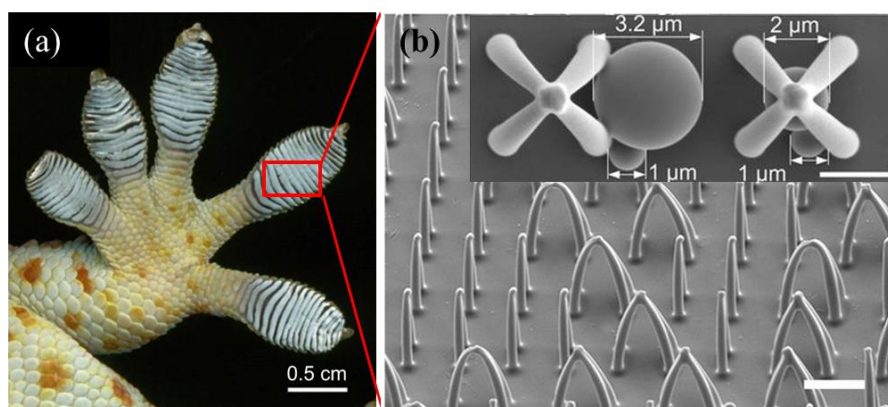


Figure 2.5: Nature as a model. (a) Gecko feet structure. (b) Bio inspired gecko feet structures to selectively trap and release micro objects (shown in the inset) fabricated by 3D DLW. Scale bar is 10µm.

Natural structures can directly use as models for artificial counterparts. For example, as shown in Figure 2.5, by directly mimicking the self-assembly structures in gecko feet structures, a micro pillar system fabricated by 3D DLW [87] can be used to selectively trap and release micro objects; this has many potential applications in the fields of biomedical research and tissue engineering. In addition, biomimetic red blood cells fabricated by 3D DLW that directly emulate the structure of biological red blood cells have also been fabricated [36]. These biomimetic structures directly mimic

the structural features in biological parts at the scale of the micrometre to the nanometre and have proved to be very useful in various fields.

2.4.2.2 Nature as a mentor

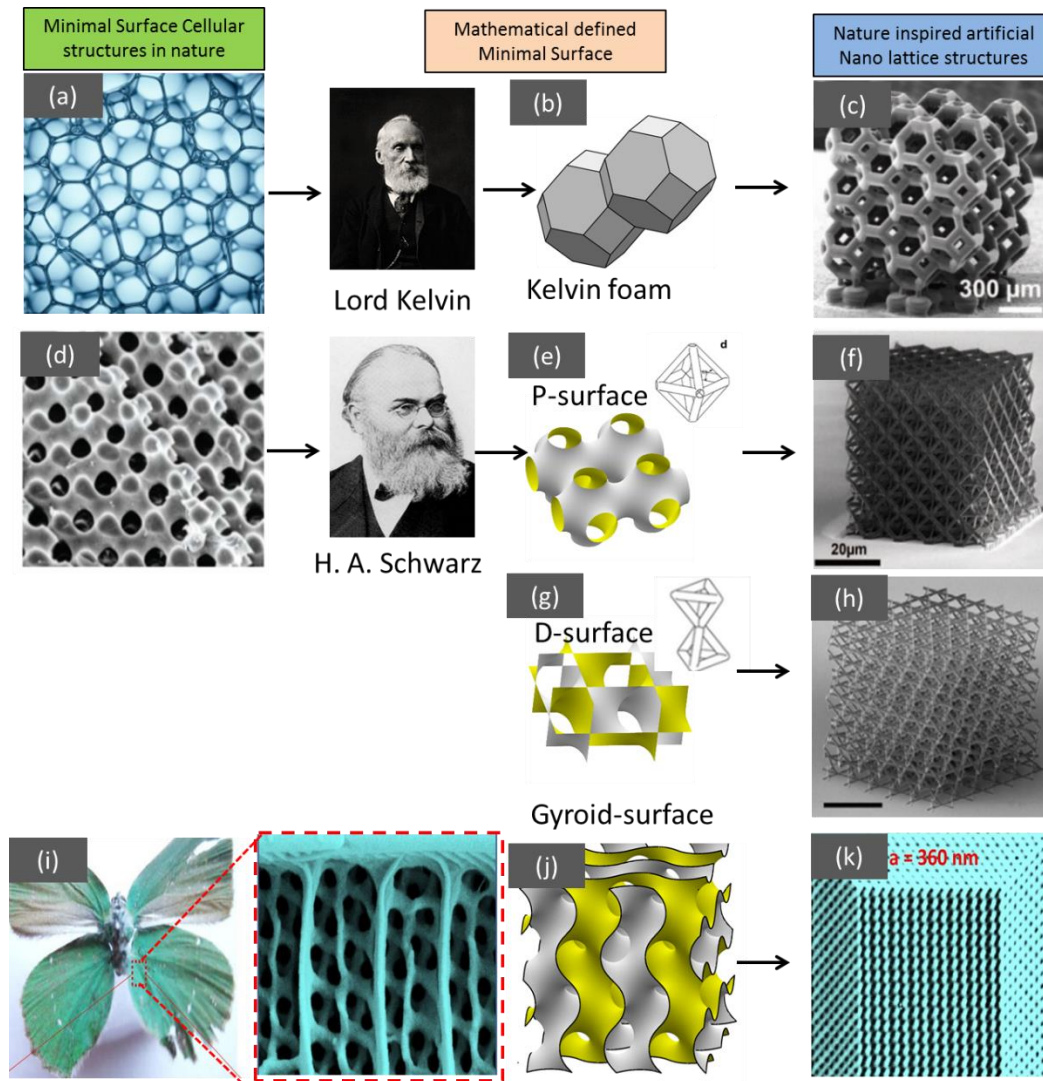


Figure 2.6: Nature as a mentor and nature-inspired low-density structures from mathematically defined ‘minimal surface’. (a)–(c) A natural bubble system, mathematical formula of Kelvin foam introduced by Lord Kelvin, and artificial Kelvin foam structures. (d)–(f) and (g)–(h) A natural bubble system between water and oil with minimal surface area, triply minimal surface area structures of P-surface introduced by HA Schwarz, artificial octet-truss structure and Kagome trusses. (i)–(k) Natural butterfly wing structure (SEM image), mathematically defined gyroid surface and artificial gyroid lattice structures.

Evolution in nature has also found a way to achieve high efficiency in various aspects, such as a high surface area to volume ratio, maximum structural strength, maximum enclosed volume, high strength-to-weight ratios and self-similar fractal structures [87]. Inspired by these features, biomimetic devices or structures have been designed with high efficiencies, such as high capacity in energy storage [88], ultra-light and ultra-stiff mechanical metamaterials [89] and architecture [90].

Natural foams such as honeycomb, wood, trabecular bone, coral and artificial synthesised polymer foams not only have low weight density (in a given application) [91], but also exhibit outstanding strength-to-weight ratios (see Figure 2.6). Inspired by these natural foams, various biomimetic lightweight/ low-density structural materials with feature sizes ranging from micrometres to nanometres have been manufactured using advanced manufacturing methods, such as gyroid lattice [92], ultra-light metallic micro lattices [93], ultra-light and ultra-stiff mechanical metamaterials [94] and ceramic Nano lattices [95]. Compared with the natural lightweight foams, biomimetic lightweight structural materials have better properties, such as higher mechanical strength, better recoverability [96], longer range of optical response [84] and better thermal conductivity and electric conductivity. Because of this better performance, these lightweight materials have shown great importance as filters, catalyst carriers, metamaterials, photonic crystals and scaffolds for tissue engineering [97].

Other work has used fractals for the design of supercapacitors [98]. In 2015, inspired by the fractal structures of fern leaves and characterised by the geometric family of space-filling curves of fractals, a new design for biomimetic laser scribed graphene electrodes for solar energy storage was introduced. By using the fractal design, the ratio of active surface area to volume of the electrodes was significantly increased, removing the limit of conventional planar supercapacitors.

2.5 Three-dimensional Direct Laser Writing

2.5.1 Introduction

Compared with traditional advanced manufacturing techniques, 3D DLW is a cost-effective, single-step nanofabrication technique. It has been developed over the past two decades [99], with several commercial systems in the market. The technology enables the fabrication of complicated 2D and 3D structures with resolutions as small as 9 nm via the use of advanced techniques [100] such as STED-based laser fabrication.

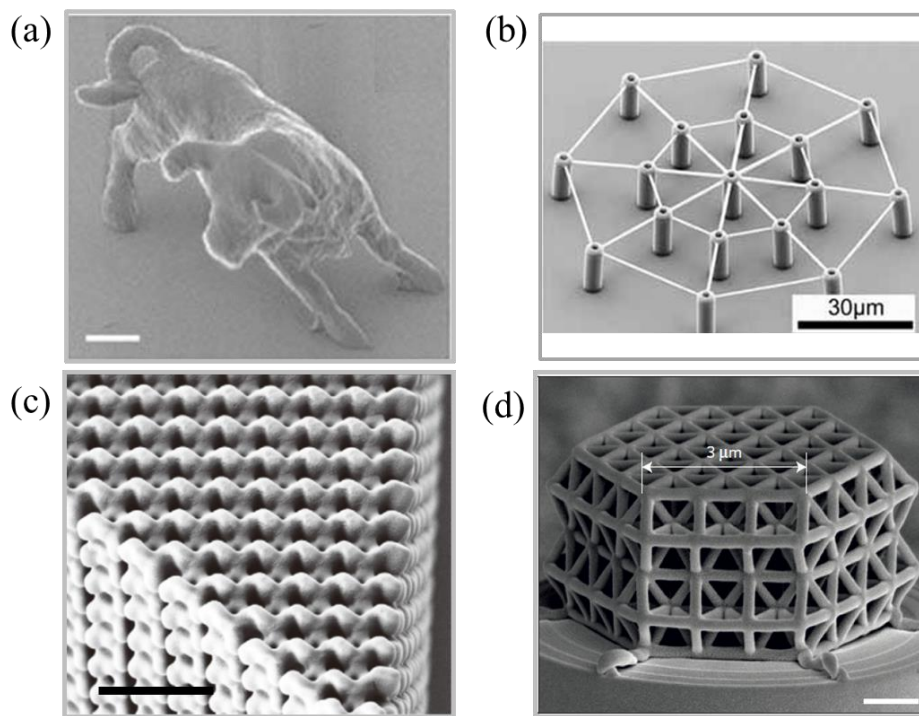


Figure 2.7: Various microstructures fabricated using 3D DLW for different application purposes. (a) Bull sculpture produced by 3D DLW, scale bar is 2 μm . (b) Elastic fully 3D microstructure scaffolds for cell force measurements fabricated by 3D DLW. (c) Photonic crystal fabricated by 3D DLW, scale bar is 5 μm . (d) Ultra-strong material made of hexagons fabricated by 3D DLW, scale bar is 1 μm .

The vast range of applications of 3D DLW includes biomedical [101], telecommunication [102], micro-optics [103], optical data storage [89], photonics [104], the fabrication and patterning of low-dimensional materials [91] and micro-electronics [105].

2.5.2 Principles of three-dimensional direct laser writing

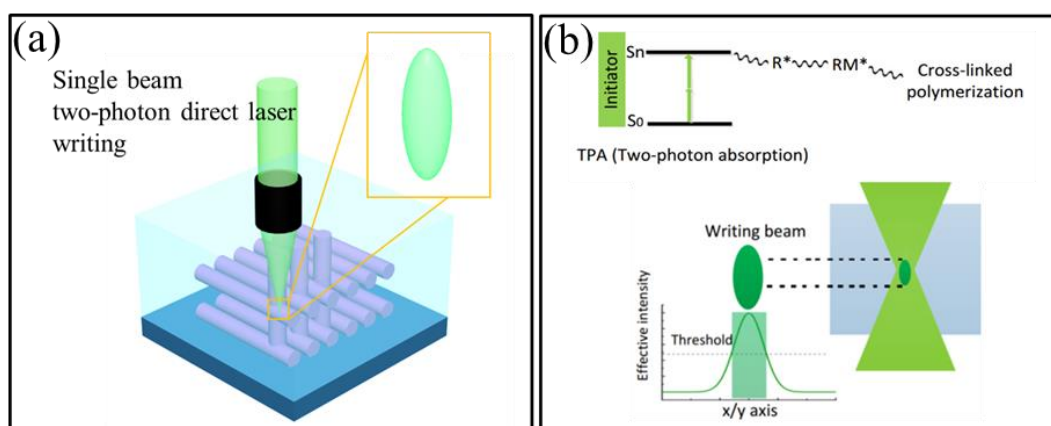


Figure 2.8: Diagrams showing the principle of 3D DLW based on two-photon polymerisation (TPP). (a) Schematic diagram showing the fabrication process of 3D DLW. (b) Diagram showing the TPP process during 3D DLW.

The 3D DLW method generally uses an ultrafast laser, such as femtosecond or picosecond laser beams [106]. The laser beam source is tightly focused on a diffraction-limited focal spot, using an objective made of different numerical apertures (NAs) to form a tightly focused intensity of light (see Figure 2.8 (a)). Transparency at the wavelength of the involved laser beam and uniformity of the sample are necessary to obtain high-quality structures. However, because of the tight focus condition, when high intensity is achieved, within this region, nonlinear reactions such as TPA [23] arise (see Figure 2.8 (b)), which triggers reactions such as crosslinked photo-polymerisation, or photo-reduction of inorganic materials. Because of the nonlinearity of these photo-reactions, nonlinear reactions can only take place within the focal region in which effective intensity stays the highest, leaving the surrounding material comparably intact. Therefore, by introducing a 3D translation stage, the sample can be moved with the focal spot drawn inside it while designed 3D structures can be traced out. In this sense, 3D DLW is regarded as a low-cost fabrication technique capable of fabricating 3D microstructures at a very fast speed [107].

Line width (feature size) and writing resolution are the two most significant features determining the dimensionality and feature size of the microstructures in 3D DLW.

The line width and the writing resolution fabricated by 3D DLW are sensitively determined by the joint contribution of the following three factors in a 3D DLW system [108]:

- laser source and equipped optics,
- photoresist or photosensitive material,
- photoinitiator and monomers (precursors).

In case of the laser source, two types of laser sources can be used in 3D DLW: CW or pulsed laser. Parameters such as excitation wavelength of the laser source and repetition rate of the laser pulse are of great significance to the performance of the system. This is because all of these parameters have an impact on the final characteristics of the microstructures [109]. Performances of optics devices that are used in the fabrication system are also critical for the feature size; for instance, the focusing distance (focal length) and numerical aperture (NA) of the objective lenses will influence the beam quality and focusing quality of the laser. The properties of the photoresist also play an important role because of the polymerisation mechanisms (typically radical polymerization or cationic polymerization), degree of crosslinking between the polymer molecules, which is related to the subsequent change in the physical phase of the resist. And the propagation and termination of the active polymeric chains between one another are also very important in 3D DLW [110].

The nature of TPA process greatly helps the reduction of the fabrication feature size in 3D DLW [111]. Nonlinear absorption of photons in TPA depends on the square of the illumination intensity (see Figure 2.8 (b)), and therefore, the profile of the exposure dose is different compared with the shape of the focal intensity volume, as it is in the traditional one-photon DLW case. The size of the exposure dose in x-y plane equals to that of the focusing volume, which is smaller than the full width at half maximum, by a factor of $\sqrt{2}$ [112],

$$\text{line width (nm)} = \frac{\lambda}{2\sqrt{2}NA} \quad (2.1)$$

Therefore, photosensitive reactions occurred in the polymerisation of the photoresist, along with the crosslinking of the polymer molecules, a threshold effect can be observed (see Figure 2.8). Hence, when the crosslinked polymerisation concentration increases over a certain value, an irreversible phase change in the photoresist (e.g., from liquid to solid) will occur in the middle part of the focal region. In contrast, in those parts of the focal region where illumination intensity is lower (surrounding area of the focal region), the density of the crosslinked polymerisation is below the required threshold for incomplete phase change to occur; this is removed later during the developing process (bath in a certain kind of developing solvent). Since the value of polymerisation threshold is determined already for a given photoresist, it is necessary to slowly decrease the illumination intensity of the laser source until the illumination intensity goes slightly higher than the value of the threshold, where the smallest feature size (under the diffraction limit compared with single-photon polymerisation) can be obtained (please refer to Equation (2.1)).

2.5.3 Schemes of three-dimensional direct laser writing

3D DLW is a well-developed technique in the fabrication of 3D structures with nano- and micrometre feature sizes. In general, in 3D-DLW, a (pulsed) laser is tightly focused on a diffraction-limited spot within the volume of a thick-film photoresist. Taking advantage of a super-linear effect (e.g., two photon absorption), the exposed volume can be restricted to a small volume element, the voxel, which is then scanned in 3D to obtain arbitrary structures. Typically, two schemes of 3D DLW are used in this field (see Figure 2.9).

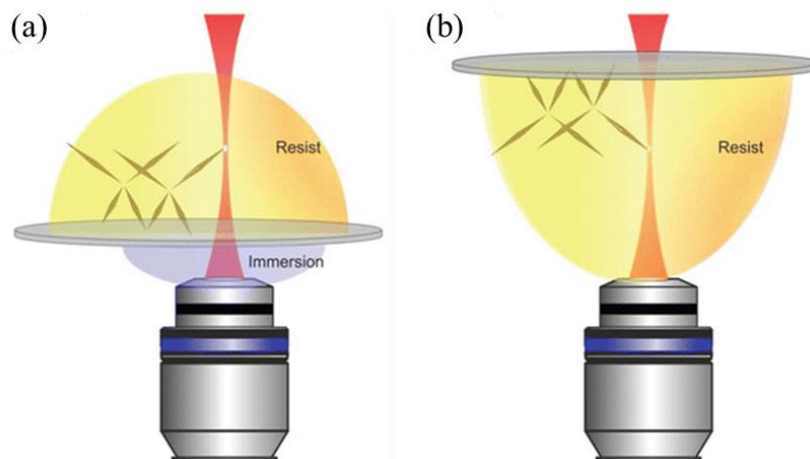


Figure 2.9: Two schemes of 3D DLW. (a) Focusing scheme of traditional 3D DLW optical lithography. (b) Focusing scheme of dip-in 3D-DLW approach. Figures are from [113].

Traditional 3D DLW (see Figure 2.9 (a)) involves a high NA objective lens, emersion oil, substrate and photoresist. However, with the limited working distance of the microscope objective lens and the aberrations arising from the refractive index mismatch between glass substrate and photoresist, this method has a limited obtainable height. Typically, the overall height of 3D DLW using this scheme is only tens of micrometres.

Recent developments in 3D DLW have utilised a novel method named ‘dip-in’ 3D DLW (see Figure 2.9 (b)). A liquid photoresist is used as the immersion medium between the focusing lens and the sample (photoresist), which does not necessarily need to be transparent. Therefore, structures with height even up to millimetres along with sub-micrometre feature sizes can be easily fabricated.

2.5.4 Practical constraints of three-dimensional direct laser writing

2.5.4.1 Voxel formation

While theoretically speaking, 3D arbitrary microstructures could be fabricated utilising 3D DLW, there are several practical constraints. First, the 3D writing voxel (or pixel) that is used to trace out and fabricate the microstructures has a fundamental limitation on this feature size. As discussed above, the exact minimum feature size that can be achieved in 3D DLW depends on the photosensitive material and

wavelength/frequency of the laser in use. For instance, commercially available photosensitive polymers such as IP-L [114], Ormocer [115] and SU-8 [116] generally have comparably small voxel size, about 100 nm in the x-y plane and 300 nm in the z-direction. The inequality of sizes in the x-y plane and z-direction of the voxel is a result of the unavoidable elongation from the focusing of the lens in the focusing region [117]. This elongation is even worse when the refractive index of the photosensitive materials increases, such as in chalcogenide glass, or when unexpected spherical or birefringent aberrations are introduced in the system [103].

2.5.4.2 Structural integrity and shrinkage

The second practical constraint is integrity of the microstructures; in other words, the mechanical stability of the 3D microstructures. An inevitable drawback related to 3D DLW of any photoresist is lack of mechanical strength to form stable structures and resulting deformation such as shrinkage [118,119]. This lack of mechanical strength results from reducing the laser power (intensity) when fabricating smaller feature sizes. For each design of 3D microstructure, these mechanical requirements must be taken into consideration; fabrication conditions and strategies should be carefully designed corresponding to their unique structural features, such as square [120] or circular cross-section [121] structures to provide enough mechanical support for the stability of the microstructure.

2.5.4.3 Crosslinking density

As we discussed above, the shrinkage of 3D microstructures poses a huge challenge in 3D DLW. This can occur both during and after the laser fabrication process and both are related with the crosslinking density during the fabrication. During the laser fabrication or polymerisation process, the mass density of the photoresist is increased due to the phase change (from the liquid to the solid, larger volume to smaller volume), therefore, the generated 3D microstructures have the potential to shrink [122]. Additional shrinkage happens during the developing process to remove the un-polymerised materials [123]. This additional shrinkage originates from the laser fabrication process and is highly dependent on fabrication conditions. During the developing process, capillary forces experienced by the structures during drying

process can easily exceed the elastic strength of the fabricated 3D microstructures [121]. Eiffel-tower-like deformation can be generally observed, in which the shrinkage leads to more volume loss further from the solid surface.

Various commercial photosensitive materials, such as Epon and SU-8, have been introduced to minimise shrinkage or with optimisation for low shrinkage purposes. Some other strategies in compensating for shrinkage are focused on the 3D design of the structure appropriately; for example, by using inverse shrinkage volume, the shrinkage of woodpile-like structures can be almost eliminated [124]. In addition, increased shrinkage can also be used to enhance the fabrication resolution, when the microstructure is designed appropriately.

2.5.5 Recent developments in three-dimensional direct laser writing

In regard to solving the practical limitations of 3D DLW based on single-beam fabrication, recent developments in 3D DLW have witnessed several technical improvements to tackle the problems discussed in Section 2.5.4.

2.5.5.1 Reduce feature size beyond diffraction limit

Traditional single-beam two-photon DLW requires a high energy dose to polymerise the materials; therefore, by adjusting the laser energy dose and exposure time, the size of polymerisation can be changed. However, this method sacrifices the polymerisation rate during fabrication, resulting in a microstructure with very low-level mechanical properties. Inspired by the invention of the stimulated depletion (STED) microscope [125], super-resolution two-beam laser fabrication has been developed based on similar mechanisms.

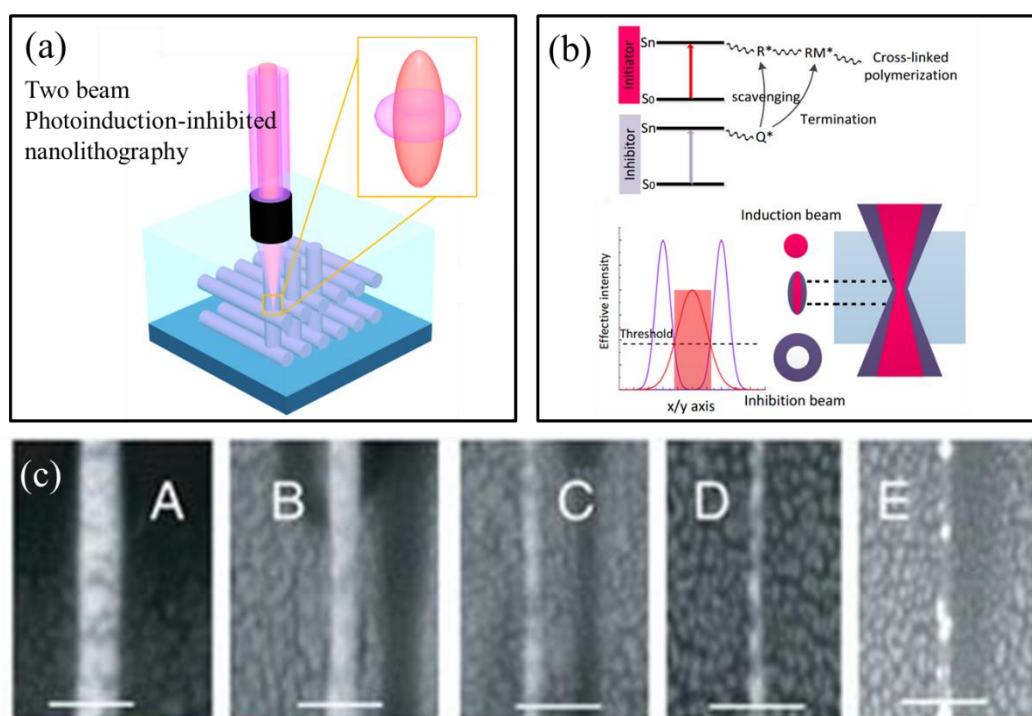


Figure 2.10: Two-beam super-resolution photoinduction-inhibited nanolithography (SPIN). (a) Illustration of the principle of two-beam SPIN lithography [84]. (b) Decrease of the fabricated feature size by increasing the inhibition beam power. Smallest feature size 9 nm. Scale bar 100 nm.

Fourkas [126], McLeod [127], Menon [128] and their research groups proposed and experimentally achieved super-resolution laser fabrication technique based on STED mechanism in 2009. The principle of two-beam super-resolution laser fabrication is that during the laser-induced polymerisation process, a second laser beam, called the ‘inhibition beam’, is introduced to inhibit the polymerisation. Because the second beam is a doughnut shape, effective polymerisation can only be achieved in the centre part of the two laser beams (see Figure 2.10 (a) and (b)). This method not only effectively reduces the laser fabrication feature size but maintains a very high polymerisation rate and correspondingly high mechanical properties. In 2013, Gu [129] and his research group achieved a world record with a single line feature size of 9 nm (see Figure 2.10 (c)) and two-line resolution 52 nm. The super-resolution laser fabrication technique pushes the fabrication resolution of the TPP technique from the sub-micrometre scale to the nanometre scale. It has been demonstrated that two-beam SPIN lithography can not only achieve super-resolution feature size, but also has

stronger mechanical capability compared with single-beam DLW because of the induction and inhibition process.

2.5.5.2 Compensate the elongation of writing voxel

As discussed above, the elongation of the writing voxel in DLW is a problem resulting from the high NA of the objective, refractive index difference in the optical system, and the polarisation state difference in the laser beam [104]. Several methods have been proposed and tested to compensate for the elongation of the writing voxel in laser fabrication. Some groups use mechanical compensation methods, such as parallel superposition [102] and galvo-dithering [84]; others have proposed optical compensation methods, such as optical slit [130] and adaptive optics [131] to tune the beam profile before the objective. All these have been shown to have a great influence on compensation for the elongation in the writing voxel and have been very useful in different applications [132].

2.5.5.3 Improve fabrication efficiency

In general, the smallest feature size in 3D DLW is around 200 nm. By using the point-by-point fabrication method, target microstructures can be achieved using nano movement stages. Therefore, the fabrication efficiency and fabrication scale are all limited by the nanostage. To speed up fabrication, Braun [133] and his group proposed using scanning dithering mirror systems to achieve small scale of high-speed fabrication. Instead of using a mechanical movement of the stage to fabricate, the use of the rotation of a reflection mirror achieves the highest speed of 19 cm/s. Other methods are also proposed to achieve parallel fabrication. Micro lens arrays [134], optical diffraction devices [135] and spatial light modulators [136] have been utilised to achieve multiple focusing fabrications. In particular, the use of spatial light modulators not only achieves multiple focusing, but dynamically tunes the focusing positions, intensities and polarisation states at each focusing point. In 2015, Gu [137] and colleagues combined super-resolution laser fabrication and the multi-focus technique to realise a writing and reading speed at KB/s with capacity of 30 TB in an optical data storage device.

2.5.5.4 Expand the material library

2.5.5.4.1 Inorganic materials for 3D DLW

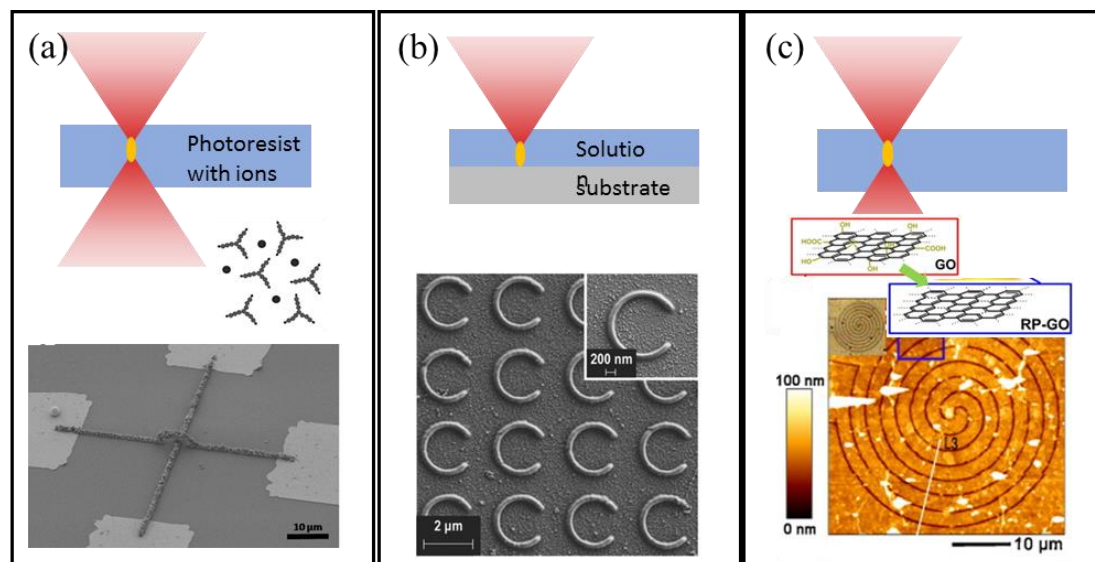


Figure 2.11: Two-photon fabrication technique in inorganic materials. (a) Fabrication of conductive structures using a femtosecond laser beam used in photoresist doped with ions. (b) Fabrication of microstructure arrays based on two-photon reduction in metal ion solution. (c) Fabrication of a conductive graphene structure using two-photon reduction of graphene oxide.

Traditional 3D DLW based on the TPP technique can only fabricate structures in polymers. Processing of inorganic materials or metals can only be achieved using atomic layer deposition and spin coating on the polymer structures. Recent development of reduction of metal ions using a femtosecond laser based on TPA has shown potential for many applications [138]. As shown in Figure 2.11 (a), metal ions are first dispersed in the photoresist. After, with the illumination of the femtosecond laser beam, photoresist in the focusing region polymerises, while the metal ions experience photo-reduction. Thus, a conductive microstructure can be realised. Pure metal microstructures can be also achieved if metal ions are dispersed in water [105], with the aid of surfactant (see Figure 2.11 (b)). In addition, reduction of graphene oxide can also be achieved using a femtosecond laser [139] to reduce the oxygen groups on graphene oxide film (see Figure 2.11 (c)).

2.5.5.4.2 Biocompatible hydrogels for 3D DLW

Biocompatible hydrogels have been utilised for many applications in biomedical science, such as biosensors [101], self-healing materials [140] and contact lens [141] because of their highly absorbent property in water, high flexibility and high biocompatibility. Technically, hydrogel materials are a kind of organic material composed of macro-molecules of polymer gel, constructing of a network of crosslinked polymer chains.

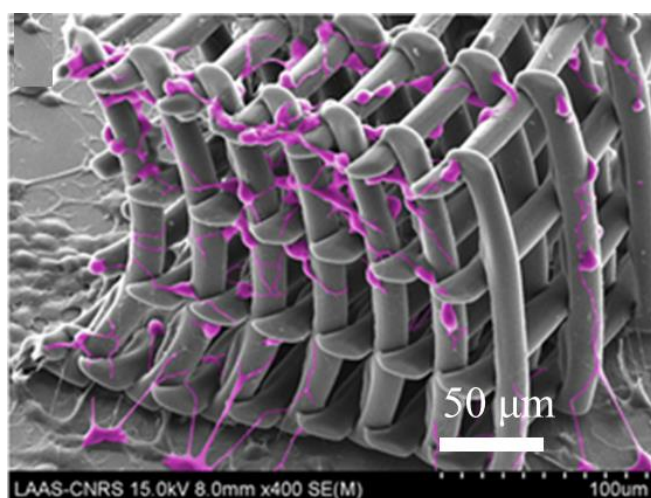
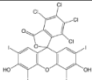
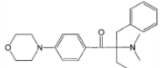
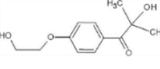
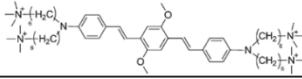
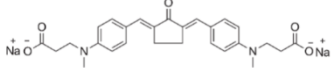

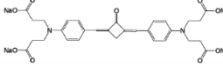


Figure 2.12: 3D Biocompatible PEGDA hydrogel structures fabricated by 3D DLW. SEM image of a 3D PEGDA hydrogel scaffold colonised by neuron cells [153].

Recent development of hydrogels focuses on the selection of photoinitiators that are compatible with hydrogels for 3D DLW based on TPP. As shown in Table 2.2, various types of photoinitiators [142-147] have been proposed and utilised in fabrication of hydrogels based on TPP. Due to the high biocompatibility of the materials, 3D scaffolds have been fabricated for cell cultures in tissue engineering [148]. The high resolution of the TPP approach allows the creation of free-standing microstructures, providing the effective development of a cell network throughout the 3D microstructure, promoting the formation of regeneration neurotic extensions for individual neuron cells [149].

Table 2.2: Comparative analysis of various photoinitiators in water solubility and biocompatibility.

Year	PI	Chemical Structure	σ_{TPA} (GM)	Water Soluble	Cytocompatible
2000	Rose Bengal (Commercial)		10	Yes	No
2010	Irgacure 369 (Commercial)		7	No	Yes
2011	Irgacure 2959 (Commercial)		/	Yes	Yes
2012	WSPI from J. Stampfl		120	Yes	No
2013	G2CK from R. Liska		136	Yes	Yes
2014	WI from M. Duan		200	Yes	No
2017	T3 from Y. Zhao		231	Yes	Yes

2.5.6 3D DLW of bioinspired microstructures

Recent developments in 3D DLW have also been proposed and utilised in fabrication of complicated bio inspired microstructures, such as red blood cell structures [36] and ovarian cancer cells [150] (see Figure 2.13), which genuinely emulate the structural features of their natural counterparts and have proved very useful in generating a variety of cell-matrix studies in biology, providing insight into generating scaffolds for tissue engineering. Another group fabricated biocompatible microstructures by means of 3D DLW, demonstrating that these microstructures can be rhythmically deformed by single beating cardiomyocytes [151].

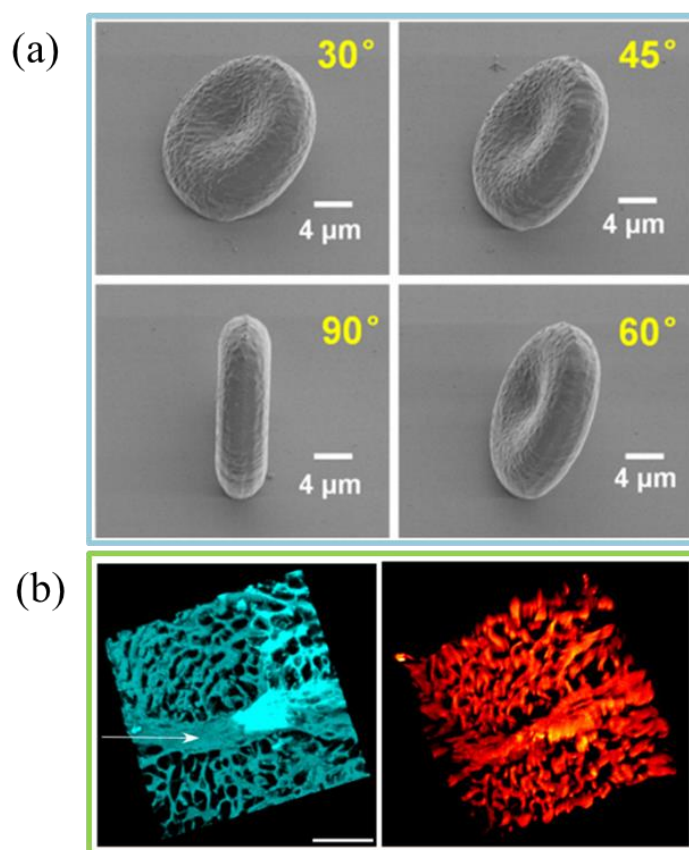


Figure 2.13: Bio inspired microstructures fabricated by 3D DLW. (a) Hydrogel red blood cell microstructures of varied geometries fabricated using 3D DLW. (b) 3D blood vessel structure (right) fabricated by laser renderings based on the model (left) derived from mouse ventricle. The large feature indicated by the arrow is a blood vessel.

2.6 Summary

In this chapter, we provided an overview of the structural features of BNNs and current state-of-the-art development of neuron-inspired structures, biomimetic design, material development and 3D DLW.

A general introduction to the structural features of BNNs was given in the beginning of the chapter. Other neuron-inspired structures were also compared and summarised. Dimensionality and scale for 2D and 3D neuron-inspired structures were discussed. In addition, recent developments in nature-inspired structures were also discussed because these are also utilised in neuron-related research. All these reviews provide us a detailed understanding of the development of neuron-inspired structures.

Biomimetic designs are considered a solution to many human-related issues, and a detailed discussion of nature as a model and nature as a mentor was provided. We utilise this concept to assist the design of neuron-inspired structures in this thesis. When we regard neurons as a model, the branch structures of neurons can be used as a biomimetic design. Chapter 3 focuses on fabrication of biomimetic neuron structures based on this concept. However, if neurons are regarded as a mentor, a mathematical model can be generalised as a biomimetic design for neuron-inspired structures. Chapter 4 introduces a novel neuron-inspired structure based on this concept (Steiner tree structures). A comprehensive study of the design, fabrication and characterisation of this structure is given in Chapter 4.

The state of art development of 3D DLW discussed in this chapter showed the principles and limitations of 3D DLW. As a generalisation of the challenges for our fabrication of neuron-inspired structures at the sub-micrometre scale, we focus on solving fabrication challenges for different fabrication designs.

Recent developments in using biocompatible hydrogels in 3D DLW show that hydrogel is a promising material for fabrication of neuron-inspired structures. Chapter 5 introduces and develops a hydrogel suitable for 3D DLW. The TPP process is studied, and optimal laser power and writing speed confirmed. Based on the swelling behaviour of hydrogel, in Chapter 5, reversible shape microstructures are fabricated, and characterised, and neuron-inspired fractal structures are also fabricated.

Chapter 3: Three-dimensional Direct Laser Writing of Biomimetic Neuron Structures

3.1 Introduction

Reproducing the structure of BNNs to create optimised biomimetic structures has been an active area of research over the last decade, with many fabrication approaches, such as EBL and soft lithography developed to build 2D biomimetic neuron structures in a variety of materials including hydrogels [152] and silicon wafer [153]. The recent development of 3D additive manufacturing has shown potential to produce 3D large-scale biomimetic neuron structures using biocompatible inks [154,155]. These biomimetic structures not only provide structural supports [156] and direct neuron shapes [157], affect neuron differentiation [158], migration and proliferation [159-161], but also have proved to reflect involvement in different neuron functional tasks [162] because these structures provide varied mechanical and biochemical cues. However, because BNNs possess extraordinary connectivity and complexity with different dendritic branch angles, branch lengths and branch diameters from the millimetre down to the nanometre scale [163,164], previous methods to reproduce the topological features of BNNs are either limited to 2D or lack fabrication resolution in building 3D structures. 3D DLW based on multiphoton absorption, such as single-beam two-photon DLW [165] and two-beam SPIN [166], has been widely studied and utilised to produce 3D micro and nano structures [167].

In this chapter, we demonstrate the ability of 3D DLW to generate 3D biomimetic neuron structures with various geometrical features of a sub-micrometre feature size. We theoretically and experimentally demonstrate a semi-empirical theory, modelling the capillary force induced during the developing process after laser fabrication. Based on our theoretical model, complicated biomimetic neuron structures are fabricated by directly implementing the neuron structural database of biological neurons with optimum laser fabrication conditions. The size of our fabricated biomimetic neuron structures is 10 times smaller than biological counterparts. This work is published in Optics Express [168].

3.2 Concept of Three-dimensional Direct Laser Writing of Biomimetic Neuron Structures

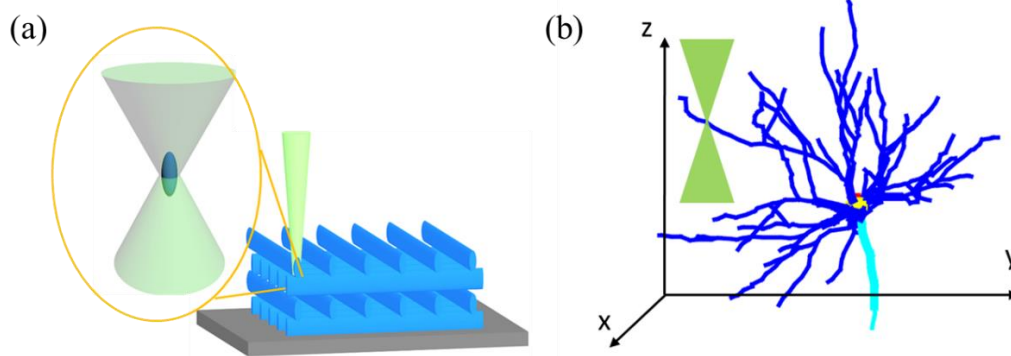


Figure 3.1: Concept of 3D DLW of biomimetic neuron structures. (a) Illustration of fabrication process of a typical 3D DLW system. (b) Diagram demonstrating the process of building biomimetic neuron structures using 3D DLW.

The concept of using 3D DLW to fabricate biomimetic neuron structures is shown in Figure 3.1. The structural data of biomimetic neuron structures are obtained from the online neuron database *neuromorph.org*. After being processed by MATLAB, the neuron structures are written by translation of the sample on the piezoelectric nano-translation stage to trace out the structure in the sample (see Figure 3.1 (b)).

3.3 Branch Features of Individual Neurons

Individual neurons are the basic topological and functional elements in BNNs. Famous as a dendritic branching structure, the structural features of individual neurons have been widely studied in neuro-morphology because of their unique contribution between topological and functional relationships in BNNs [169-173]. Recent studies in neuronal morphology show that neurons come with different branching angles ($0^\circ\sim 90^\circ$), branching diameter ($< \mu\text{m}$), and branching length ($\sim \mu\text{m}$) and branching orders [174, 175] (see Figure 3.2). The branching features of neurons are regarded as fractal and self-similar using mathematical analysis methods to describe the branching structure [176-178]. Branching features also been studied using path optimisation theory [179, 180], which shows that neuron branching structures pursue the shortest connection distance between each neuron. Further, topological features of individual neurons also play an important role in neuron information processing and their involvement in neuron-environment interactions, such as angiogenesis and metabolic exchange, has been studied.

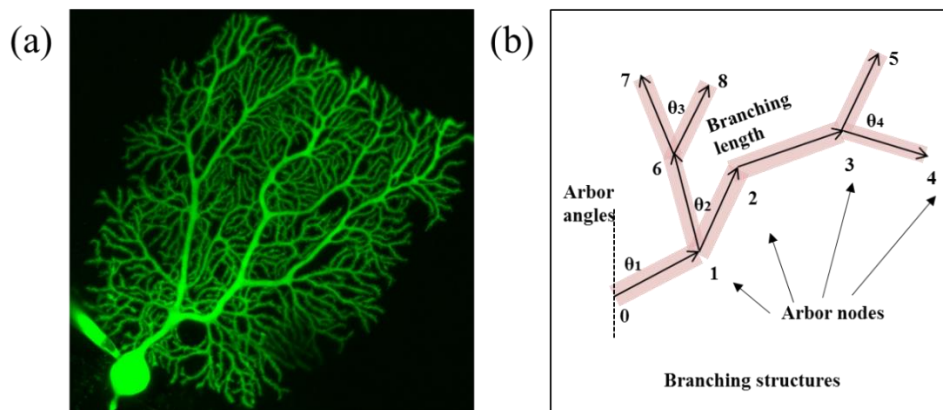


Figure 3.2: The branch tree of biological neurons and the morphological represented model in micromorphology research. (a) A rat Purkinje neuron injected with a fluorescent dye. Purkinje neurons are the major output neurons of the cerebellum. (b) Branch structures consist of different branch angles (arbor angles), branch length and branch order (arbor nodes).

3.4 Challenges in Fabricating 3D Biomimetic Neuron Structures

Using 3D DLW

As we can see from the branching structures of biological neurons, fabrication of 3D a biomimetic neuron structure using 3D DLW to emulate the branching features of biological neurons faces several fabrication challenges.

First, the fabrication feature size needs to be smaller than 1 μm . Biological neuron structures possess feature sizes ranging from several micrometres to down to hundreds of nanometres; therefore, it is necessary to understand the formation of the writing voxel in 3D DLW, and the influences of fabrication conditions, such as laser power and writing speed, on the feature size in 3D DLW.

Second, the branch structures of biological neurons are microstructures with high aspect ratio. The stability of these high-aspect ratios of branch structures are greatly influenced by the capillary force induced during the drying process after the laser fabrication. In particular, when a thin elastic structure comes in contact with a liquid interface, capillary forces can be sufficiently large to induce elastic deformations. This effect becomes particularly relevant at small scales where capillary forces are predominant, for example in microsystems (micro-electromechanical systems or microfluidic devices) under humid environments, and thus much effort has been made to eliminate its negative effects.

Therefore, when high aspect ratio biomimetic neuron structures are fabricated using 3D DLW, the dominant capillary force will drive them to collapse, cluster or be destroyed. This detrimental phenomenon is highly dependent on the condition of the scanning beam, and well within the scope of optical technology as part of applied optics. However, previous studies in 3D DLW, such as the simple pillars model [181] and a supercritical-point dryer [182], which focus on eliminating the detrimental effects of capillary force, are not suitable for complicated neuron structures (being either too complicated or too expensive). Novel model and theory must be introduced to consider the effect of capillary force in 3D DLW and the effect of fabrication conditions on capillary force during the developing process. Sections 3.5 and 3.6

investigate the prospects for tackling the challenges in fabrication of 3D biomimetic neuron structures.

3.5 Influence of Fabrication Conditions on Fabrication Feature Size in 3D DLW

To fabricate biomimetic neuron structures that emulate the branch features in biological neurons at the sub-micrometre scale, our first task is to understand how to control the fabrication feature size in 3D DLW. 3D DLW, based on TPP, is a popular nano fabrication method, where nonlinear TPA by the photoinitiators in the photoresist starts the polymerisation reaction. The polymerisation reaction can be confined into a small volume around the focal spot given that the excitation probability of a single photoinitiator molecule via TPA depends on the square of the incident light intensity.

Theoretically, given a 3D DLW system and a certain material used in 3D DLW, the writing feature sizes in single-beam DLW based on TPP are defined by Equation (3.1) in x-y plane and Equation (3.2) in the z-direction:

$$l_{xy} = \frac{\lambda}{2\sqrt{2} \times NA} \quad (3.1)$$

$$l_z = \frac{2.5 \times \lambda}{2\sqrt{2} \times NA} \quad (3.2)$$

in which λ is the wavelength of the laser used and NA is the numerical aperture of the objective. Therefore, for our experimental set up, the smallest linewidth that we can achieve using the single-beam DLW system is approximately 150 nm in the x-y plane and 375 nm in the z-direction.

Practically, the feature size produced by single-beam DLW is influenced by various experimental parameters in the fabrication system, such as laser power, writing speed and threshold of the photosensitive material.

Following an experimental model describing the linewidth formation in 3D DLW [188], we present the fabrication of suspended polymer lines using our home-built 3D DLW system in our zirconium-based organic–inorganic photoresist to investigate the

influence of laser power and writing speed on the linewidth. This is because, in 3D DLW based on TPP, the polymer line consists of the voxel. The width of the polymer line is the diameter of the voxel in the x-y plane and the height of the line is the height of the voxel in the z-direction.

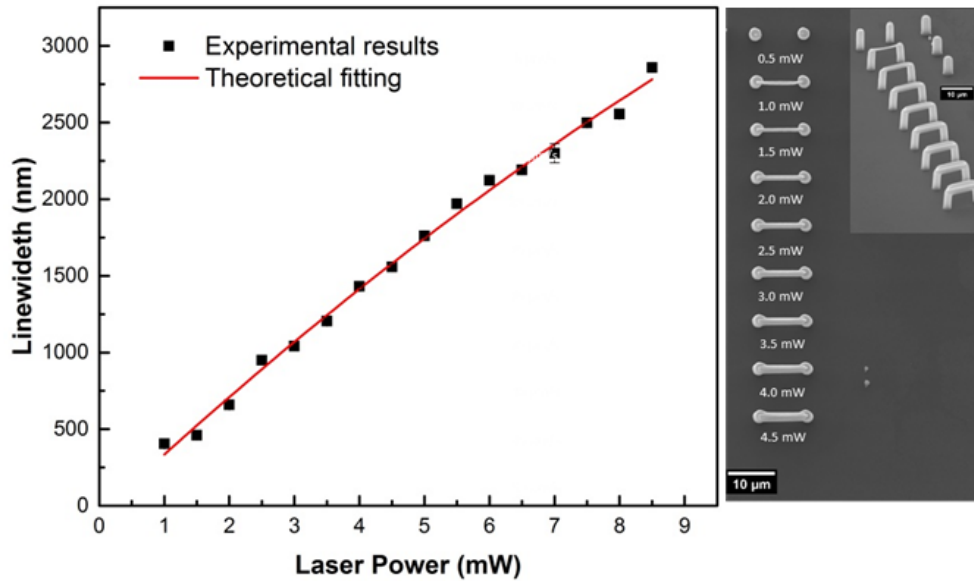


Figure 3.3: Two-photon fabrication linewidth as a function of laser power and the top view of the SEM images of suspended polymer lines fabricated at constant writing speed of $10 \mu\text{m/s}$ with laser power ranging from 0.50 mW to 4.50 mW . The side view of the lines in the inset.

To determine the laser threshold and linewidth of the as-prepared photoresist, polymer lines were fabricated at a constant writing speed of $50 \mu\text{m/s}$. The relationship between the linewidth and laser power at a linear writing speed of $10 \mu\text{m/s}$ was confirmed by adjusting the laser power from 0.5 mW to 4.5 mW . As shown in Figure 3.3, it can be observed that the resolution improves as laser power decreases, which is consistent with previous results reported by our and other groups [189]. In the laser threshold of 1.0 mW , the line width is around 300 nm (Figure 3.4). When the laser power is 8.0 mW , the line width is larger than $2,500 \text{ nm}$. It can be found that the height of the lines is 2.5–2.6 times the width, in accordance with previous studies [190].

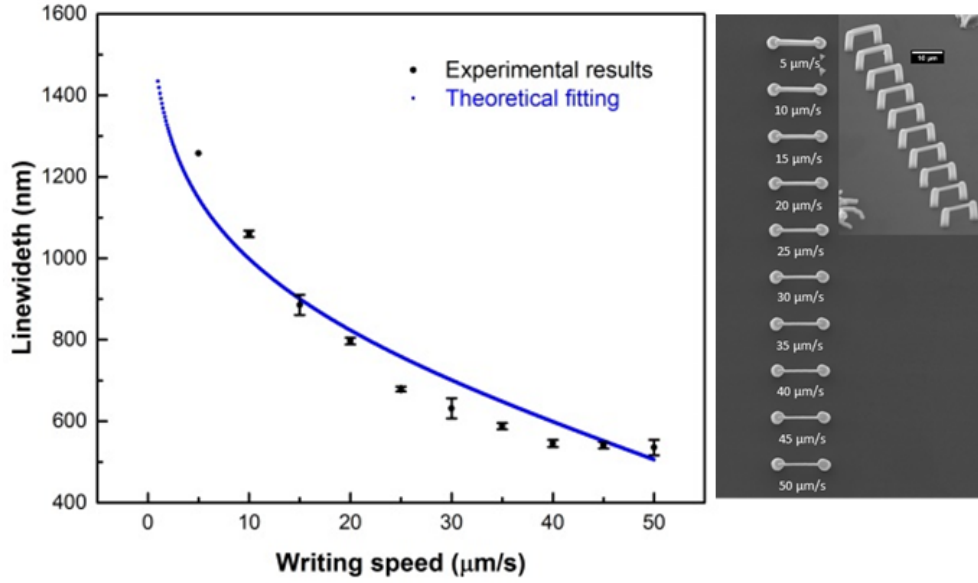


Figure 3.4: Two-photon fabrication linewidth as function of writing speed and the top view of the SEM images of suspended polymer lines fabricated at a constant laser power of 1 mW with the writing speed ranging from 5 $\mu\text{m/s}$ to 50 $\mu\text{m/s}$. The side view of the lines in the inset.

Similarly, the relationship between the line width and writing speed at the given laser power of 1 mW was confirmed by adjusting the writing speed from 5 $\mu\text{m/s}$ to 50 $\mu\text{m/s}$. As shown in Figure 3.4, resolution falls as the writing speed increases. At the writing speed of 50 $\mu\text{m/s}$, the line width is 475 nm, and the height of the lines is 2.5–2.6 times the width.

Our experimental results were fitted to the formula in reference [183]. According to this formula, $L(P, s)$ is the line width in 3D two-photon DLWs, P is the average power of the beam, w_0 is its half width at $1/e^2$ of the intensity maximum, and s is writing speed. I is the incident energy (in J/m^2) at a distance d from the middle of the propagation direction. Thus, I_{MAX} is the incident energy at the waist ($d = 0$; $I_{max} = \sqrt{\frac{2}{\pi}} \frac{P}{\omega_0 s}$) and I_{th} is the polymerisation threshold energy of the photoresist.

$$L(P, s) = \omega_0 \sqrt{2 \ln \frac{I_{max}}{I_{th}}} \quad (3.3)$$

$$I(d) = \sqrt{\frac{2}{\pi}} \frac{P}{\omega_0} e^{-2d^2/\omega_0^2} \quad (3.4)$$

Here, in our experimental set up, the beam waist of the femtosecond laser is 480 nm, laser power ranges around several microwatts, and writing speed is around 1 millimetre per second. The threshold energy of our photoresist is about 73.9 J/cm², and 39.5 J/cm², which is in agreement with results in previous research [184]. The spatiotemporal polymerisation behaviour described by Equation (3.4) is further confirmed by studying the relationship between fabrication line width and laser power / writing speed (shown in Figures 3.3 and 3.4).

3.6 Influence of Fabrication Conditions on the Stability of 3D

Biomimetic Structures in 3D DLW

As discussed in Section 3.3, another challenge in fabrication of 3D biomimetic neuron structures using 3D DLW is the detrimental effect induced by the capillary force during the developing process. Controlling the stability of 3D structures at the scale of the micrometre is challenging. Previous methods that have been used are either too simple (such as single pillar theory) or too difficult to achieve (such as the critical dryer).

It is well known that the capillary force exerted by the developing process is significantly influenced by the geometrical characteristics of the microstructures, such as aspect ratio, suspended angle between liquid and the structure, length of the microstructure, diameter of the structure and the spatial arrangement of the microstructures. For our task of fabrication of 3D biomimetic neuron structures, the geometrical characteristics of our 3D biomimetic neuron structures, such as branch diameter, branch angle and branch length, are influenced by fabrication conditions, such as laser power and writing speed. Therefore, it is convenient to introduce a model that can describe the impact that fabrication conditions have on the stability of our microstructures.

In Sections 3.6.1 and 3.6.2, a simplified branch model is introduced that is able to relate the fabrication conditions, such as laser power and writing speed, to the

geometrical characteristics of 3D biomimetic neuron structures at the micrometre scale.

3.6.1 Branch model

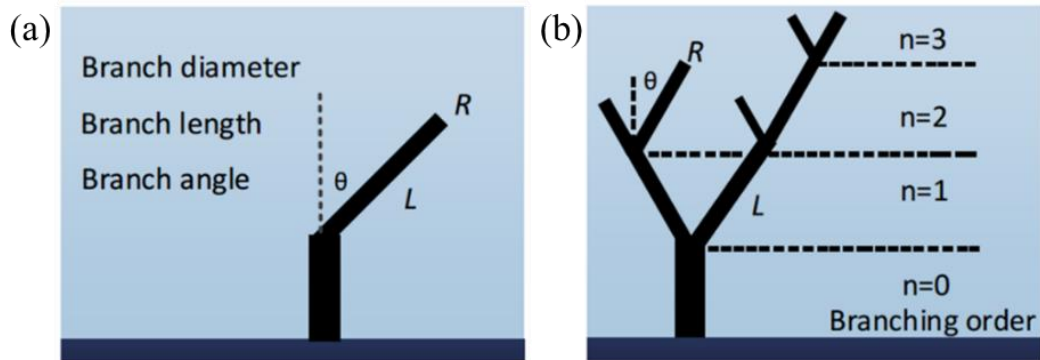


Figure 3.5: Branch models inspired by biological neurons. (a) Single branch model of biomimetic neuron structures. (b) Multiple branch structure models of biomimetic neuron structures.

As shown in Figure 3.5, a branching model is introduced to study the mechanical properties of biomimetic neuron structures and investigate fabrication conditions using 3D DLW.

Biological neuron structures are constructed with individual single branch structures, such that each single branch structure has a certain dendritic branch angle and dendritic branch length. Similarly, our branching model constitutes both single branch structures and multiple branch structures. A single branch structure, as shown in Figure 3.5 (a), corresponds to a single branch beam posing a certain angle θ on top of a stronger beam, at a certain branch length L . In multiple branch structures, as shown in Figure 3.5 (b), single branch structures stack into a multiple branch structure, with different branch orders ($n=0, 1, 2, \dots$), branch diameters R , branch angles θ and branch lengths L .

Thus, to construct biomimetic neuron structures using 3D DLW, we start by studying the mechanical properties of single branch structures, then move to extrapolate the knowledge to multiple branch structures, and eventually demonstrate biomimetic

neuron-tracing structures emulating from the biological neuron structures with different average branch angles and topologies.

3.6.2 Influence of elastic-capillary force in fabricating a single branch structure

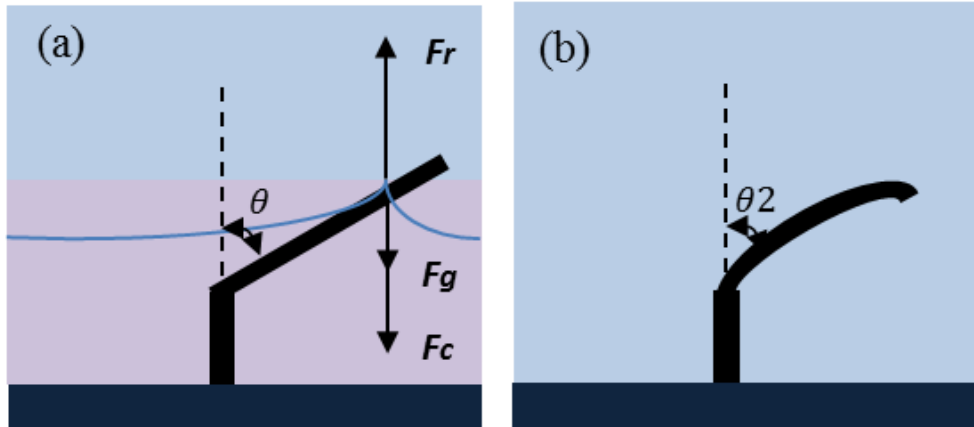


Figure 3.6: Illustration of the elastic-capillary behaviour of single branch structures. (a) Illustration of the forces interacting on the single branch structure. (b) Single branch structure deformed by capillary force.

Consider a single branch structure with branch length L , branch diameter R and branch angle θ , fabricated by 3D DLW (shown in Figure 3.6 (a)). After the laser writing, fabricated structures are dipped into a solvent to remove unpolymerised materials. According to the semi-empirical theory discussing the stability of a piercing branch structure in [23], when the solvent (1-propanol) of the photoresist evaporates to the level of the freestanding branch tips during the developing process, capillary force F_c is yielded on this single branch structure, and given by

$$F_c \sim 2\pi\gamma \times R(P, s) \times \cos^2\alpha \times 1/|\cos\theta| \quad (3.5)$$

which is proportional to the interfacial tension γ (for liquid 1-propanol, $\gamma = 25.26 \text{ mN/m}$), the branch diameter R and the cosine of the contact angle α (typical value: 60°) between the solvent and the surface of the branch, and disproportional to the cosine of the branch angle θ .

Resistance to the capillary force is the elastic restoring force F_r , which is proportional to the Young's modulus of the material E ($1-2 \text{ GPa}$) and the branch diameter R , in proportion to the branch length L , given by

$$F_r \sim \left(\frac{\pi}{2}\right)^2 \times E \times R^4 / L^2 \quad (3.6)$$

When $F_c = F_r$, a balance between the capillary force and the elastic restoring force reaches the undeformed shape of the single branch structures. By combining Equation (3.5) and Equation (3.6), a critical diameter $R_{critical}$ can be derived given a single branch structure with branch angle θ and branch length L , and can be expressed as

$$R_{critical}(\theta, L) \sim \sqrt[3]{1/\pi \times \gamma \times 1/E \times \cos^2 \alpha \times L^2 \times 1/|\cos \theta|} \quad (3.7)$$

The branch diameter corresponding to the fabrication line width in 3D DLW, which is a parameter relying on laser power P and writing speed s described by [18], is expressed as

$$R_{critical}(\theta, L) = \omega_0 (\sqrt{2} \ln(\sqrt{\frac{2}{\pi}} \times \frac{P}{\omega_0 \times s \times I_{th}}))^{1/2} \quad (3.8)$$

in which I_{th} is the polymerisation threshold energy of the photoresist and ω_0 is the half width of the laser beam in the focusing region. For the convenience of our discussion and experiments, branch length is fixed at 10 μm , both in our theoretical discussion and experiments.

According to this theory, stable single branch structures can be fabricated by controlling the laser power and writing speed to tune the size of branch diameter that satisfies the balance between capillary force and elastic restoring force. The criteria that we use in qualifying the deformed and undeformed structures (shown in Figure 3.6 (b)) depend on the displacement of the tip of a branch. The structure is regarded as undeformed if the displacement is less than the branch diameter.

3.6.3 Quantitative study of the stability of single branch structures

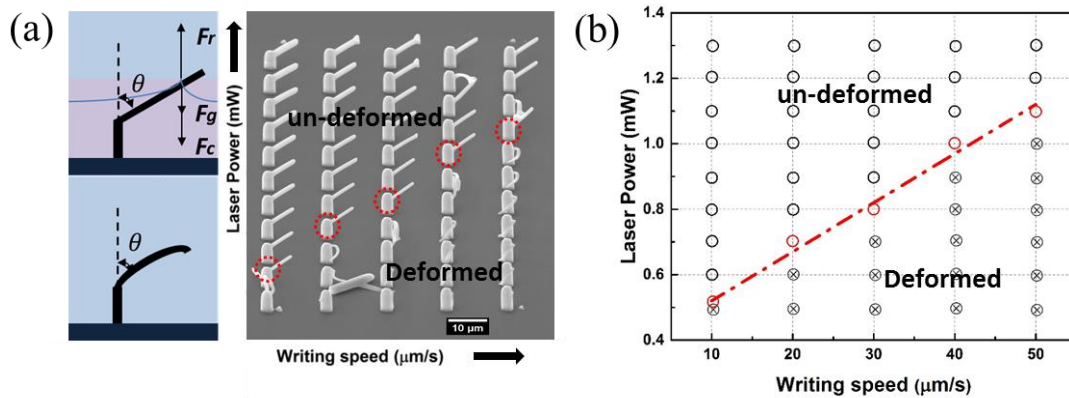


Figure 3.7: Quantitative study of the deformation behaviour of single branch structures fabricated by 3D DLW. (a) Side view of SEM images (tilting angle of 30°) of single branch structures with branch angle of 45° fabricated at varied writing speed and laser power; inset top: illustration of the forces interacting on the single branch structure; bottom: single branch structure deformed by capillary force. (b) Quantitative study on critical boundary of single branch structures with different branch angles. ‘+’ and ‘o’ are experimental results; solid lines are theoretical fitting.

First, given a single branch structure, faster writing speed requires larger laser power when fabricating stable single branch structures. This is confirmed by fabricating arrays of single branch structures with varied branch angles (branch length of $10\ \mu\text{m}$) at different laser powers (from $0.5\ \text{mW}$ to $2.0\ \text{mW}$) and writing speeds (from $10\ \mu\text{m/s}$ to $50\ \mu\text{m/s}$). As shown in Figure 3.7 (a), a single branch structure with the branch angle of 45° is fabricated by scanning laser power and writing speed. A critical line is shown in Figure 3.7 (b) with red circles, and quantitatively summarised and fitted theoretically in Figure 3.7 (b). Above this critical line, un-deformed single branch structures can be achieved; below this, a deformation resulting from the capillary force would occur. This is in agreement with the theory discussed above. The position of this line is influenced by the critical branch diameter $R_{critical}$ of the structure itself and the laser dose required in the fabrication.

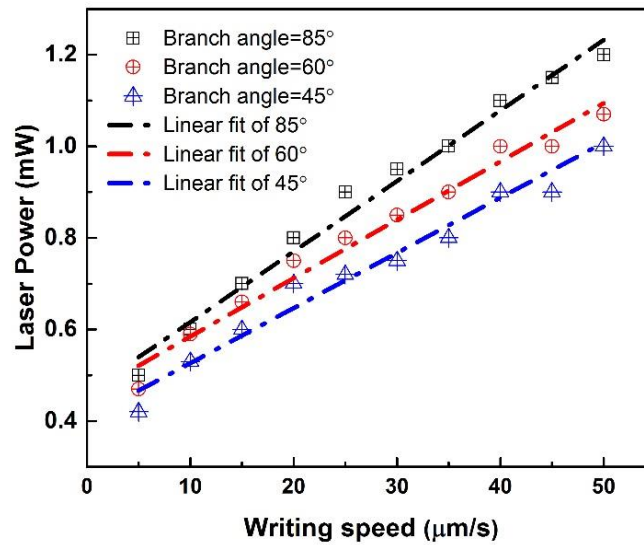


Figure 3.8: Quantitatively study on critical boundary of single branch structures with different branch angles as a function of laser power and writing speed.

Second, for a fixed writing speed, single branch structures with larger branch angles require larger critical branch diameters to achieve balance between capillary force and elastic restoring force, which corresponds to higher laser power during fabrication. Further experiments were also performed to confirm our theory by fabricating single branch structures with different branch angles. As shown in Figure 3.8, single branch structures with different branch angles have unique critical fabrication condition lines. As discussed above, the position of this line is influenced by the critical branch diameter required. As seen from Figure 3.8, for a given fabrication speed of $50 \mu\text{m/s}$, a single branch structure with a branch angle of 85° requires a fabrication laser power of 1.2 mW , while the former laser power is 1.0 mW to fabricate a single branch structure with branch angle of 30° . Because the photoresist in the fabrication area is only exposed once by the laser beam, the phenomenon of deformation seen in the laser power / writing speed matrix presented in Figure 3.8 can be explained by Equation (3.4).

3.6.4 Fabrication of multiple branch structures

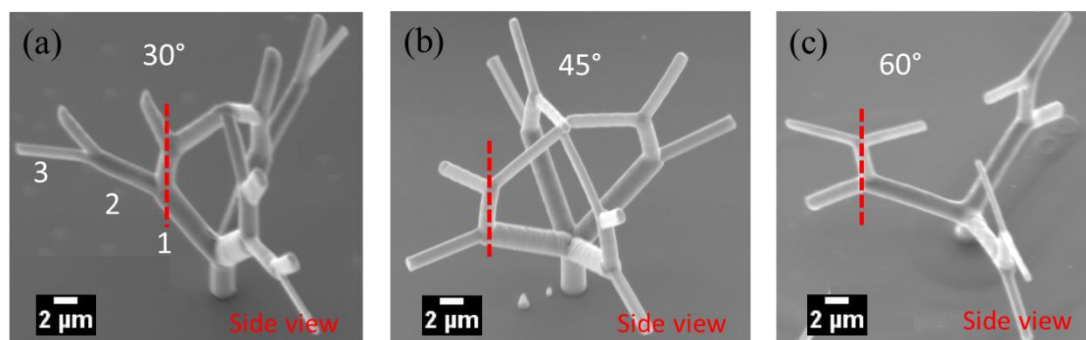


Figure 3.9: Fabrication results of multiple branch structures with different branching angles. Side view of the SEM images (tilting angle of 30°) of multiple branch structures with average branch angles of 30° , 45° , and 60° fabricated at varied writing speed and laser power (corresponding to panels (a), (b) and (c)).

Based on the study on maintaining mechanical stability in building single branch structures, we demonstrate that multiple branch structures with average branch angles of 30° , 45° and 60° can be fabricated under optimised fabrication conditions with laser power of 0.8 mW, 1.1 mW and 1.2 mW at the writing speed of $50 \mu\text{m/s}$. We note that subtle changes in our fabrication resulted from an uncontrollable microenvironment change during the drying process.

3.7 Fabrication of Biomimetic Neuron-tracing Structures

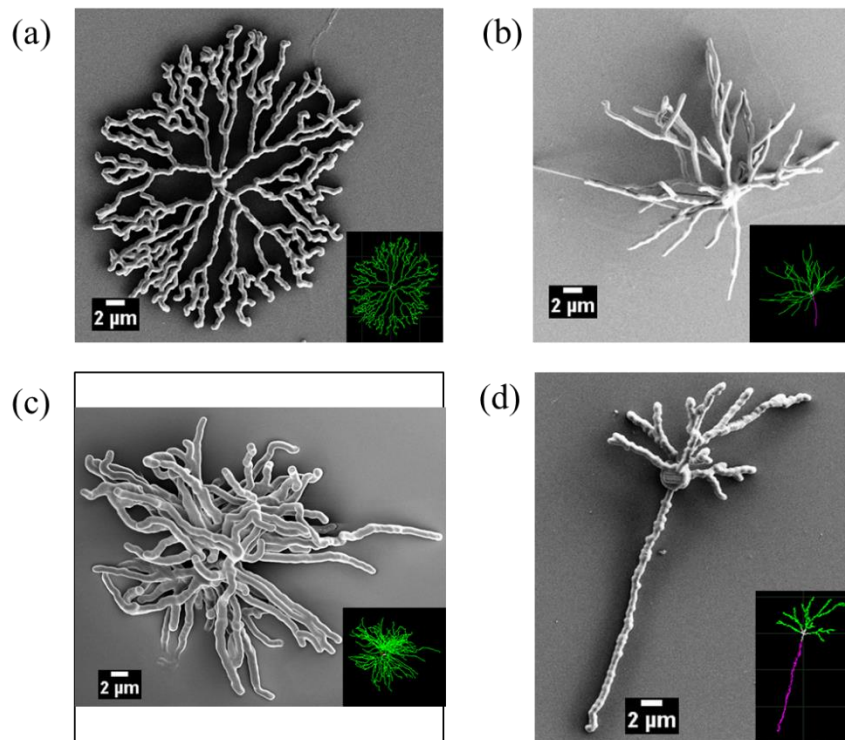


Figure 3.10: Fabrication results of biomimetic neuron structures with different average branching angles. (a), (b), (c) and (d) are the top view of the SEM images of 3D biomimetic neuron structures with different average branch angles fabricated under optimised conditions. Insets in each figure are the 3D digital reconstruction of biological tracing structures.

The feasibility of 3D DLW in producing biomimetic neuron structures with high mechanical stability and desired structural features is further demonstrated by building biomimetic neuron-tracing structures.

We begin by extracting the morphology data of various kinds of neurons from an online database [20]. The morphology data are processed by a custom MATLAB code and a LabVIEW system to create 3D printable neuron models for our home-build 3D DLW system. By tracing out the topology of neuron structures, biomimetic neuron structures with different branch angles, branch lengths and branch diameters can be generated through 3D DLW. The topology of neuron structures from raw neuron morphology data and our fabricated 3D biomimetic neuron structures are shown in Figure 3.10. Four selected biological neuron structures from different parts of neuron

system in an animal body are shown in the insets of Figure 3.10, respectively: (a) Ganglion neuron cell from the retina of a rabbit, with biological neuron size: height $302.16 \mu\text{m}$, width $257.57 \mu\text{m}$, depth $13 \mu\text{m}$; (b) Pyramidal neuron cell from the neocortex of a human, with biological neuron size: height $383.18 \mu\text{m}$, width $141.25 \mu\text{m}$, depth $51.41 \mu\text{m}$; (c) Pyramidal neuron cell from the dorsal thalamus of a rat brain, with biological neuron size: height $232.39 \mu\text{m}$, width $256.21 \mu\text{m}$, depth $177.1 \mu\text{m}$; (d) Pyramidal neuron cell from the retina of a human, with biological neuron size: height $245.77 \mu\text{m}$, width $189.62 \mu\text{m}$, depth $90.56 \mu\text{m}$. Biomimetic neuron structures were created with sizes 10 times smaller than their original biological counterparts; SEM of biomimetic neuron structures are shown in Figure 3.10.

3.8 Optical Characterisation of Biomimetic Neuron-tracing Structures

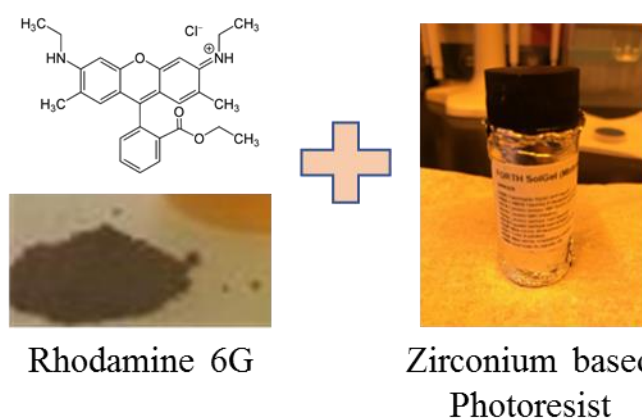


Figure 3.11: Synthesis of fluorescent photoresist (Rhodamine 6G added into zirconium-based photoresist).

To visualise the 3D feature of our fabricated biomimetic neuron structures with optical method, Rhodamine 6G was added into our photoresist before laser fabrication to create 3D fluorescent biomimetic neuron structures. Synthesis of the fluorescent photoresist is shown in Figure 3.11. Rhodamine 6G power is added into our zirconium-based photoresist to achieve an evenly mixed solution with 0.002 mg/ml of Rhodamine 6G.

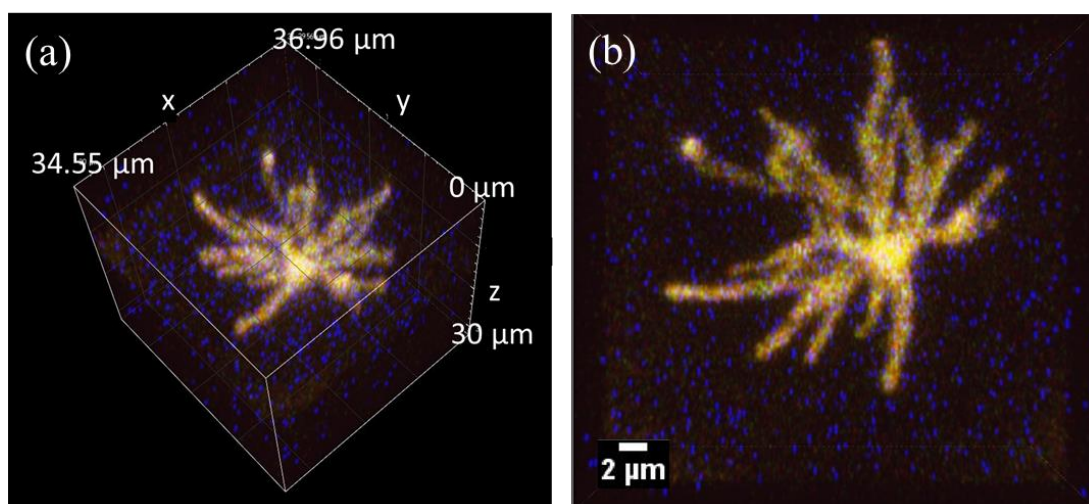


Figure 3.12: Confocal fluorescent microscope images of biomimetic neuron-tracing structures obtained using a Nikon confocal microscope. The excitation wavelength is 444 nm and the detection wavelength is 550 nm. (a) Perspective view of the fluorescent image. (b) View from the x-y plane.

A Nikon confocal microscope was used to image the fluorescent structures. A continuous wave (CW) laser source operating at the wavelength of 444 nm was used as the excitation beam to excite the Rhodamine 6G. The detection wavelength of 550 nm was chosen to obtain the fluorescent signal in our microstructures. 3D confocal fluorescent images of biomimetic neuron structure (d) were taken after the fabrication and shown in Figure 3.12 (a) and (b). Different from scanning electron microscope, confocal fluorescent microscope can give us a real 3D view of the structures by slicing the structure into different layers and reconstruct the 3D structures, which reveals that these biomimetic neuron structures maintained outstanding 3D features at the micrometre scale. This is of great significance for future applications in engineered neural networks.

3.9 Experimental Set Up

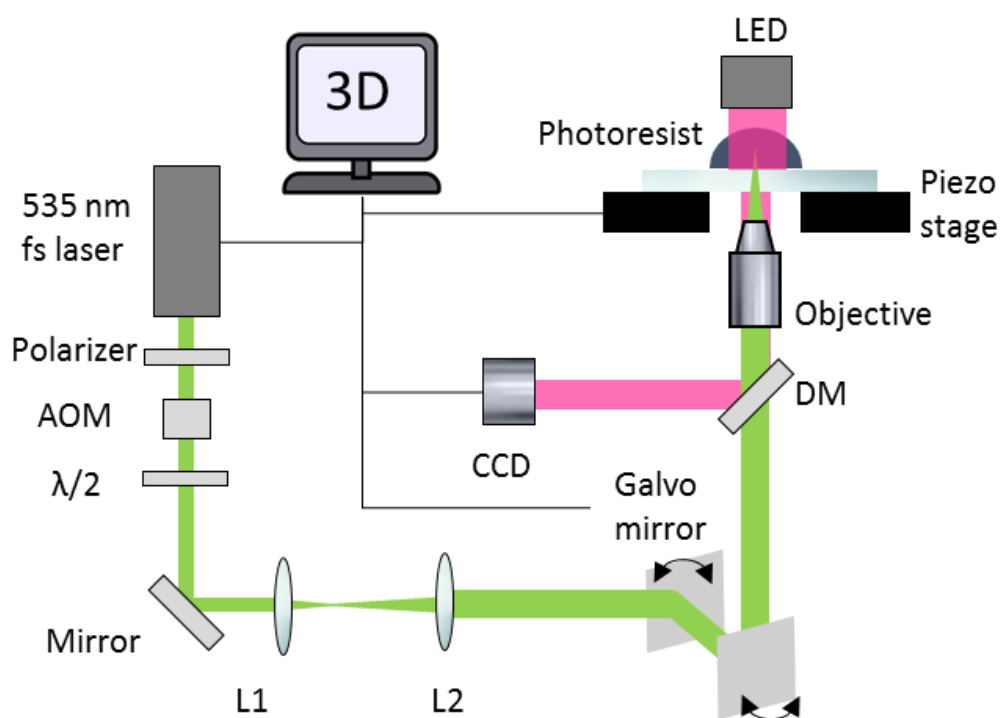


Figure 3.13: Experimental set up for our 3D DLW system.

The experimental set up of the 3D DLW is illustrated in Figure 3.13. A femtosecond laser beam operating at a wavelength of 535 nm (Fidelity), with a pulse width of 270 fs and a repetition rate of 50 MHz, was steered by a combination of a 4f imaging system and 2D galvo mirrors (Thorlabs) into a 1.4 NA $\times 100$ oil immersion objective (Olympus); beam delivery and power were controlled by an acoustic optical modulator. Within the focus of the laser beam, polymerisation occurred when the effective laser intensity was above the threshold of the photoresist (a zirconium-based hybrid organic–inorganic photoresist (see Appendix A). Biomimetic neuron structures were fabricated by translation of the sample on the piezoelectric nano-translation stage (Physik Instrumente). The measurement of the laser power was achieved using a power meter before the objective. The material synthesis process and mechanical property characterisation of our photoresist are discussed and shown in Appendices A and B.

3.10 Conclusion

In summary, we have demonstrated the fabrication of biomimetic neuron structures using 3D DLW and evaluated the influence of laser power and writing speed in fabricating biomimetic neuron structures with varied topologies.

First, the influence of the laser power and writing speed on the feature size of biomimetic neuron structures was studied and confirmed both experimentally and theoretically. The feature size during the fabrication depends on the fabrications such as laser power and writing speed.

Second, a model was introduced to study the influence of fabrication conditions on the capillary force experienced in the microstructures during the developing process. The quantitative experiment results revealed that neuron structures with different average branch angles require different fabrication conditions, such as laser power and writing speed.

Based on these understandings, the first experimental realisation of a micrometre scale biomimetic neuron structure 10 times smaller than biological neurons has been achieved using two-photon DLW in this work.

This result provides a potential method to replicate the topological features of BNNs and opens a new avenue for a higher level of understanding the structure–function relationship in engineered neural networks. Combining galvo-scanning devices, long-range translational stages and nano-translation stages can provide a potential method to replicate the topological features of BNNs to a larger scale and form a new optical technology platform for applications using 3D DLW in engineered neural networks.

Chapter 4: Three-dimensional Direct Laser Writing of Ultralow- density Neuron-inspired Steiner Tree Structures

4.1 Introduction

The neuron-tracing structures fabricated in Chapter 3 were designed when the structural features of biological neurons were directly regarded as models. In this chapter, an advanced mathematical formula was derived from the biological neurons following the design principle in biomimetics of ‘nature as a mentor’, producing a novel neuron-inspired biomimetic low-density structure.

The design and fabrication of biomimetic low-density microstructures has been a hot topic for two decades. Because of their unique topographical, mechanical and biochemical characteristics, these biomimetic structures have potential applications in thermal insulation, shock damping and catalyst support, especially in neuron tissue engineering. Many fabrication techniques have been utilised to enable the creation of microstructures with controllable architectures that have structural features that can span from the μm to the nm scale. These techniques include micro-stereolithography, holographic lithography and 3D DLW. Combined with other advanced fabrication techniques, the development in this field has led to series of novel low-density

materials with unprecedented mechanical characteristics, such as ultra-light, ultra-stiff metal or ceramic-based micro lattices.

Traditionally, these biomimetic low-density structures are inspired by the prevalent features in nature: minimal surface or triply minimal surface, such as Kelvin foam, gyroid structures, octet trusses, Kagome trusses and the recently proposed Shelluar structures. Consequently, the question arises of whether a minimal surface is the only option available in designing ultralow-density microstructures. It has been demonstrated that the structures of BNNs have the ‘shortest connection distance’, which corresponds to the ‘Steiner tree problem’ in mathematics, described in 1876 by a Swiss mathematician, Jakob Steiner [185] (1796–1863).

Therefore, the work in this chapter investigates the design, fabrication, mechanical characterisation and theoretical calculation of a new type of low-density microstructure fabricated by 3D DLW: neuron-inspired Steiner tree structures. First, inspired by the geometrical features in BNNs, a new type of low-density microstructure is introduced in this part of the PhD project. It is further shown that neuron-inspired Steiner tree structures have the lowest relative density compared with traditional microstructures. Steiner tree structures with sub-micrometre feature sizes were fabricated with different relative densities using our home-built galvo-dithering DLW system. In situ nanomechanical deformation experiments showed that the biomimetic neuron-inspired Steiner tree microstructures fabricated in this work have tenable Young’s modulus and yield strength along with relative density. Based on rigidity theory, the mechanical properties of Steiner tree structures are also discussed. The mechanical properties of the Steiner tree structures fabricated by 3D DLW are investigated both experimentally and theoretically. At the end of this chapter, a conclusion is introduced. Theoretical study and finite element simulations were performed to further elucidate the mechanical properties of the microstructures.

Our work demonstrates that 3D DLW is a versatile tool in creating mechanically tuneable biomimetic microstructures for future applications in neuron tissue engineering. The introduction of neuron-inspired Steiner tree structures opens a new

family of design where microstructures with different mechanical properties can be designed and adjusted by designing the architecture geometry.

4.2 Neuron-inspired Steiner Tree Structures

4.2.1 Shortest connection distance in biological neural networks

Biological neurons often possess complicated axonal and dendritic structures spinning in 3D space, as shown in Chapter 3. It is believed that the shape of neurons reflects their function in neuron signal communication and information processing. By introducing dendritic branching structures, it has been proved that BNNs evolve according to the mechanism of optimisation in connection length, signal propagation speed and surface area [169]. One of the most important characteristics of BNNs is ‘pursuing the shortest connection distance’ [174]. Neuron optimisation of dendritic and axonic arbores can be evaluated using a generalisation of the Steiner tree concept from combinatorial network optimisation theory [175].

Therefore, inspired by the geometrical characteristic of biological neurons, a new type of low-density biomimetic structure is introduced: Steiner tree structures.

4.2.2 History of Steiner tree structures

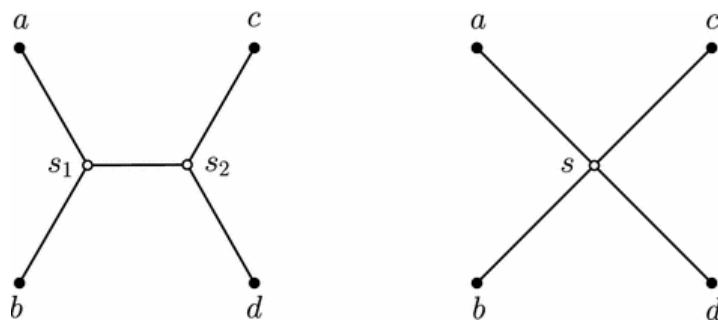


Figure 4.1: 2D minimum Steiner tree (left) and a solution to the Fermat–Torricelli problem (right) for a set of four points $N = [a, b, c, d]$ on a unit square. The minimum Steiner tree has two Steiner points, s_1 and s_2 , and length of $1 + \sqrt{3}$. The network resulting from the solution to the Fermat–Torricelli problem has length $2\sqrt{2}$.

The history of Steiner tree structure can be dated back to the Euclidean Steiner tree problem, on constructing the shortest possible network interconnecting a set of given

points in 2D or 3D space, which goes back to Gergonne in the early nineteenth century [186]. The Euclidean Steiner tree problem looks for the shortest possible network interconnecting n points in a 2D plane or 3D space. As a classic example of problems that are easy to state and understand, but very difficult to solve, an increasingly sophisticated mathematical theory of minimal networks has been developed to solve this problem since the 1960s. These theories are based on a combination of techniques from combinatorics, geometry and data analysis. The interest in solving Steiner tree problem stems not only in the challenge that it represents mathematically, but also from its wide range of potentials in areas such as telecommunications, city infrastructure network design and computer chip design [171]. Figure 4.1 shows an example of 2D minimum Steiner tree structure (left) compared with a Fermat–Torricelli problem (right) connecting four points in 2D space. By introducing two Steiner points, s_1 and s_2 , the Steiner tree structure achieves the shortest connection distance compared with other connection patterns.

Inspired by this similarity between biological neurons and Steiner tree structures, we introduce 3D Steiner tree structures as a novel biomimetic model. For the case of 3D Steiner tree structures, we follow research published in a PhD thesis in the 19th century [187]. A more detailed discussion of 3D Steiner tree structures is given in Section 4.2.3.

4.2.3 Analytical calculation of relative density of a 3D Steiner tree structure

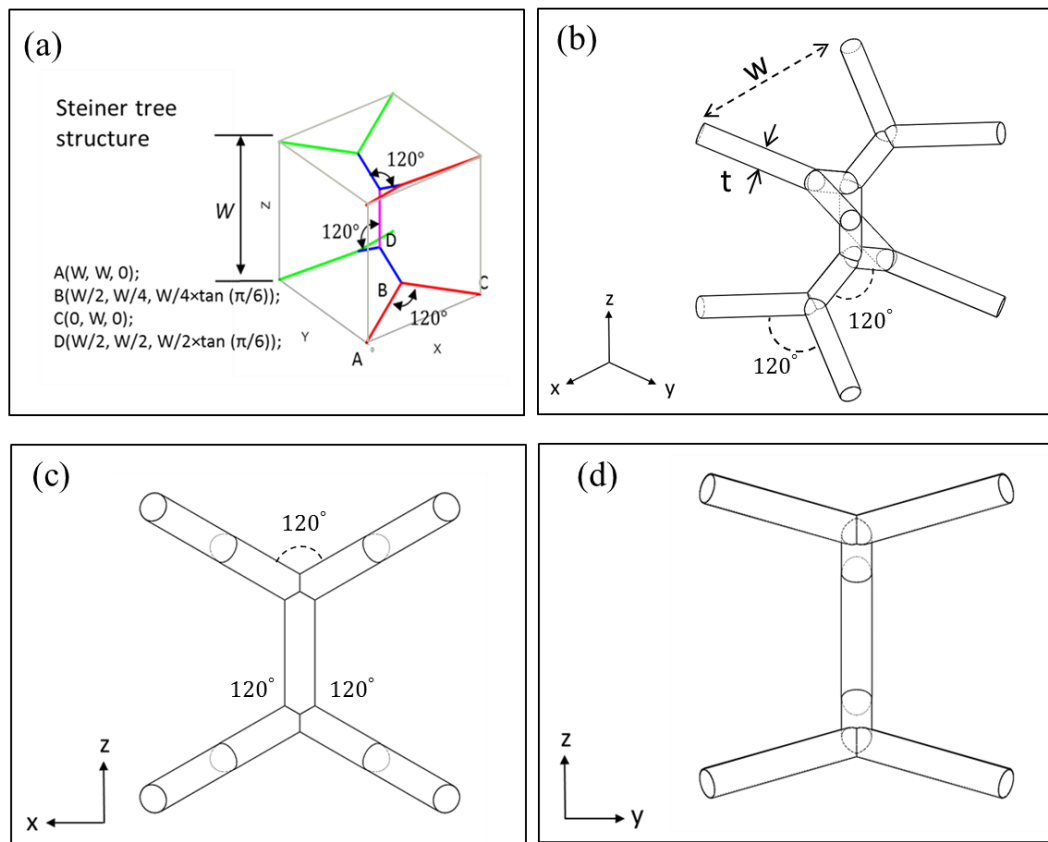


Figure 4.2: 3D Steiner tree structure connecting eight points calculated using the algorithm from reference [102]. (a) Single unit of Steiner tree structure. (b) Steiner tree structure model constructed with circular-shaped cross-section beams and built by CAD software Solidworks. (c) x-z plane view. (d) y-z plane view.

A Steiner tree structure with eight points of connection is calculated using MATLAB code [102]. In this cubic unit (unit size W), four groups of beams are shown in Figure 4.2 (a). The angles between each beam are 120° . The length of each of the red and green colour beams is $\frac{1}{2 \cos \pi/6} W$. The length of the blue colour beams is $\frac{1}{4 \cos \pi/6} W$. The length of the purple beams is $(1 - \frac{1}{\cos \pi/6}) W$.

Here, an analytical expression for the relative density of a 3D Steiner tree structure can be derived. Consider a 3D Steiner tree structure made of circular-shaped cross-section beams with beam radius R within a cubic unit cell with a width of W , as is shown in Figure 4.2. For a unit cell of a Steiner tree structure, we define the relative

density of the solid beam lattices, respectively, to be $\rho = \frac{v}{V} \times \rho_s$. Therefore, the relative density of the 8-points Steiner tree structure can be written as

$$\rho = \left(\frac{3\sqrt{3}+1}{4} \right) \pi \times \frac{t^2}{W^2} \times \rho_s \quad (4.1)$$

in which v is the volume of constructed beams, V is the volume of the cubic unit, and ρ_s is the density of the constituent material.

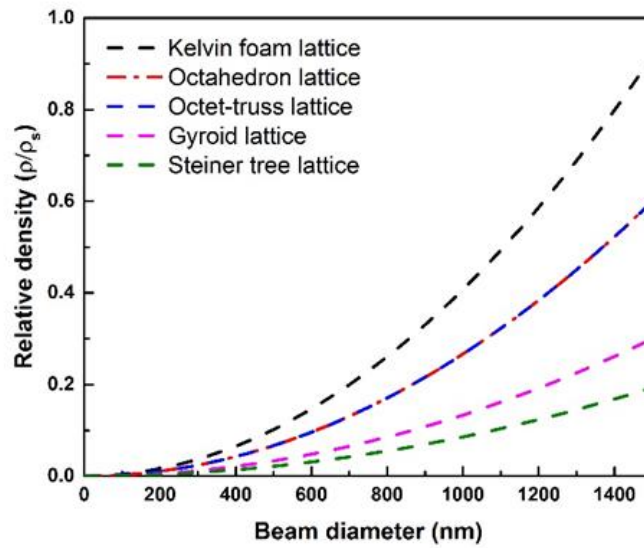


Figure 4.3: Analytical comparison of the relative densities between a 3D Steiner tree structure and other well-known lattice structures as a function of beam diameter. Black dashed line: Kelvin foam lattice; red dashed line: Octahedron lattice; blue: Octet-truss lattice, purple: Gyroid lattice. Detailed mathematical formulas are provided in Appendix. C.

Compared with other widely studied lattice structures, neuron-inspired Steiner tree structures have the smallest relative density; in other words, highest porosity among all structures. This structural feature is very advantageous for potential applications such as low-density construction materials and scaffolds for biomedical engineering.

In Sections 4.3 and 4.4, we explore the fabrication of neuron-inspired 3D low-density Steiner tree microstructures using galvo-dithering DLW.

4.3 Galvo-dithering Direct Laser Writing

As discussed in previous sections, the aim of this chapter is to fabricate neuron-inspired 3D low-density Steiner tree microstructures and characterise the mechanical properties. The galvo-dithering fabrication technique is very important to produce 3D microstructures consisting of circular-shaped cross-section beams [121]. Here, the writing voxel formation of galvo-dithering DLW is studied theoretically and experimentally. With this in mind, Steiner tree structures with various relative densities can be fabricated by tuning fabrication conditions such as laser power P , writing speed s and galvo amplitude D_{xy} .

Accurate control of writing voxel through galvo-dithering is very complicated because of the complexity of thermal effects and diffusion phenomenon in the photoresist [188]. However, it is possible to explain the effect of galvo-dithering via an empirical theory [189] in our case.

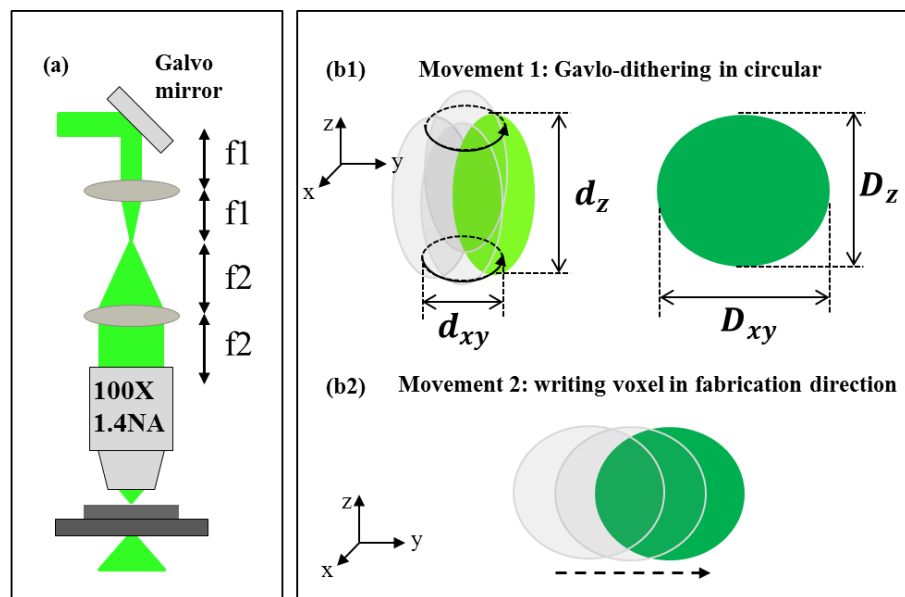


Figure 4.4: Schematic diagrams showing the writing voxel formation process in galvo-dithering DLW using circular dithered correction applied by galvo mirrors. (a) Schematic of the GD DLW set up consisting of a 2D galvo mirror and 4f imaging system to dither the laser focus. (b1) Illustration of circular dithering applied by the galvo mirrors: step 1, galvo-dithering in circular. (b2) Effect of the galvo-dithering on the fabrication voxel greatly reducing the aspect ratio. Step 2, movement in the fabrication direction. Figures redrawn from [190].

As shown in Figure 4.4, during the galvo-dithering fabrication process, the writing voxel of the laser beam inside the photoresist can be described as two movements: movement along a circular pathway by dithering of the galvo mirror, and movement along the z-direction of fabrication pathway. This simplified assumption is reasonable because the speed of galvo-dithering is much faster than the speed of movement in the z-direction. For instance, the frequency of galvo-dithering in our experiment is 1000 Hz, corresponding to a speed of $1570 \mu\text{m/s}$ (galvo-dithering diameter $0.500 \mu\text{m}$), while the speed of movement in the z-direction is only $20 \mu\text{m/s}$. A theoretical discussion on the relationship between galvo-dithering voltage and galvo-dithering diameter can be found in reference [193].

To investigate the effect of galvo diameter D_{xy} , a series of suspended polymer lines were fabricated at laser power of 0.4mW and laser fabrication speed of $20 \mu\text{m/s}$. The diameter of the polymer lines in the x-y plane were characterised using a SEM (see Figure 4.5, right panel).

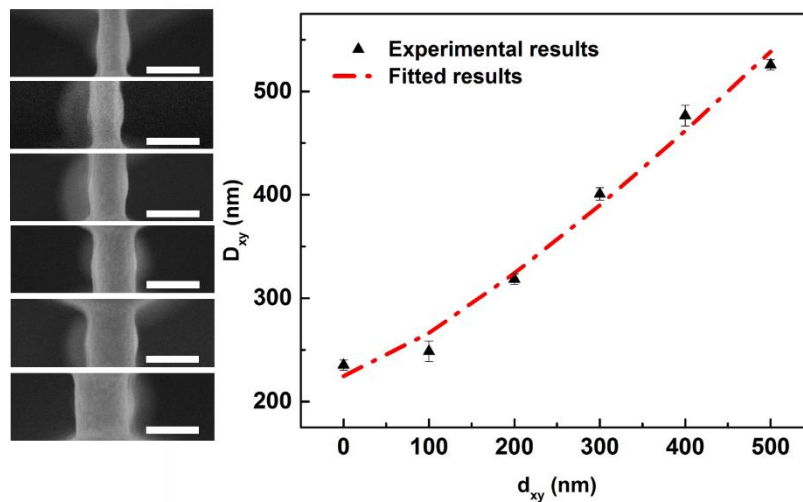


Figure 4.5: Effect of galvo-dithering diameters on fabrication linewidth in the x-y plane. Right: Fabrication linewidth as a function of galvo-dithering diameter. Black dots are experimental results; red dashed line is theoretical fitting according to Equation (4.2). left: SEM images of fabricated polymer lines with different galvo-dithering diameter. Scale bar is 500 nm.

As shown in Figure 4.5 right, given a fixed power and laser speed, the experimental results can be fitted theoretically into an empirical formula,

$$D_{xy} = \alpha \times d_{xy}^{\beta} + D_{min} \quad (4.2)$$

where $\alpha=0.1278$, $\beta=1.2560$, and $D_{min}=224.74$ nm. Here, D_{min} is the minimum fabrication voxel diameter in the x-y plane for a fixed laser power and writing speed, and α and β are coefficients related to fabrication conditions and photoresists.

By tuning the applied galvo-dithering diameter, laser power and writing speed, accurate control of the aspect ratio of the writing voxel can be achieved (refer to Section 4.4.3), and fabrication of micro-lattice structures with circular-shaped cross-section beams with high accuracy can be accomplished.

4.4 Fabrication of 3D Neuron-inspired Steiner Structures Using Galvo-dithering 3D DLW

In this section, we investigate the fabrication of low-density 3D Steiner tree structures using galvo-dithering 3D DLW. Our fabricated method involves a galvo-dithering DLW fabrication system. In contrast to the traditional 3D DLW, the galvo-dithering technique has been widely studied and utilised in 3D DLW fabrication systems and has proved very effective in improving the fabrication resolution of 3D microstructures. In addition, the compensation of writing voxel in the x-y plane and the z-direction can have a significant impact on the cubic symmetry of photonic crystals, influencing transmission and optical activity. Further, it is also demonstrated that the galvo-dithering technique enhances the mechanical properties of the microstructures.

4.4.1 Standard process of fabrication of 3D microstructures using DLW

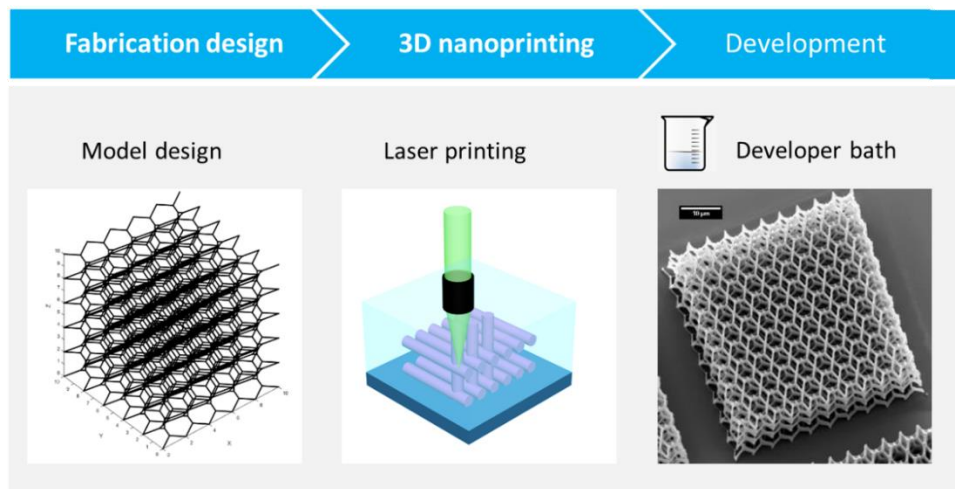


Figure 4.6: Microstructure fabrication process. Step 1: Design of fabrication path. Step 2: Import the fabrication path 3D DLW fabrication system. Step 3: Post-fabrication developing process. After these three steps, the sample is characterised using a SEM.

Nanolattices in this chapter were created using a multi-step 3D DLW in a zirconium-based organic–inorganic negative photoresist (refer to Appendix. A) synthesised in our lab. First, the fabrication path controlling the laser movement was designed using MATLAB. The codes were then transferred to the 3D DLW system to accomplish the laser fabrication. After fabrication, the samples were dipped into a developing solution (Isopropanol solution) for one hour and dried at room temperature in air. The characterisation of the feature sizes of the fabricated results were performed using a high-resolution FEI Verios 460L SEM in the RMIT Microscopy and Microanalysis Facility (RMMF), RMIT University.

4.4.2 Fabrication path design

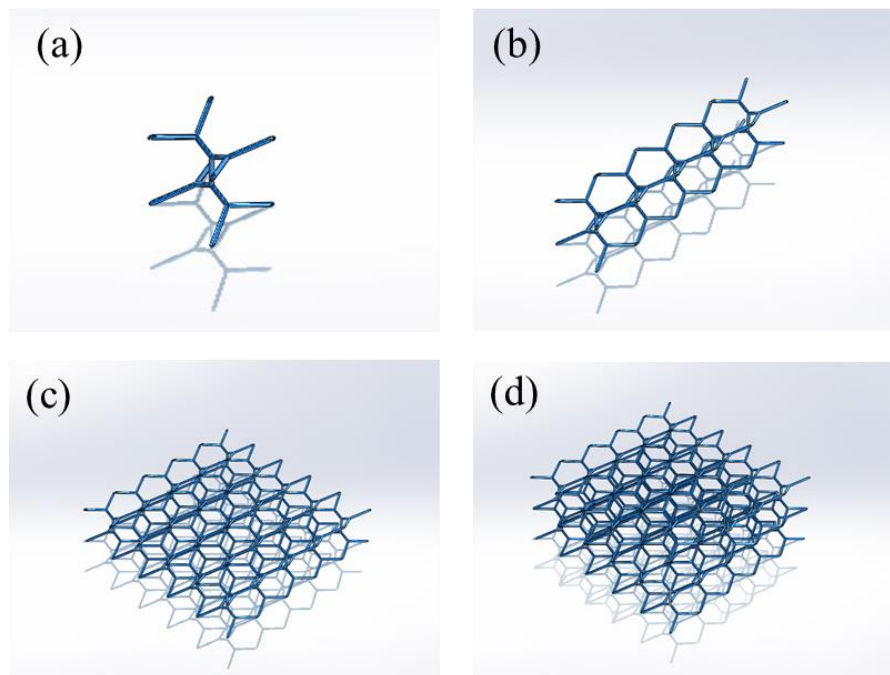


Figure 4.7: Design of fabrication path for the Steiner tree structure (viewed from an oblique angle). Note all of the axes are created in dimensionless unit cells. (a) A single unit cell of the Steiner tree structure. (b) Single unit cell of the Steiner tree network but with rods moved to neighbouring unit cells to form a fully connected unit cell. (c) and (d) $5 \times 5 \times 3$ -unit cells of the Steiner tree network.

The fabrication capabilities provided by our home-built 3D DLW system enable several methods of fabrication of 3D microstructures, such as the layer-to-layer fabrication of most 3D printing systems, and line-by-line methods. In this PhD project, we use a line-by-line fabrication method. As such, periodic lattices created with this system can be fabricated in a unit by unit fashion. Firstly, single unit cells are taken and patterned according to their symmetry directions (see Figure 4.7 (a) and (b)). Secondly, more unit cells can be fabricated along another direction (shown in Figure 4.7 (c)). Finally, the whole 3D structures can be fabricated by fabricating the upper layers of structures. Compared with other fabrication methods [104], this is the most convenient and efficient fabrication method for our Steiner tree structures with simple cubic symmetry, and very versatile because any unit cell can easily be substituted in for fabrication.

4.4.3 Fabrication results

In this section, the fabrication results of our Steiner tree structures are shown from different aspects.

4.4.3.1 Compensation in the x - y plane and z -direction of the writing voxel

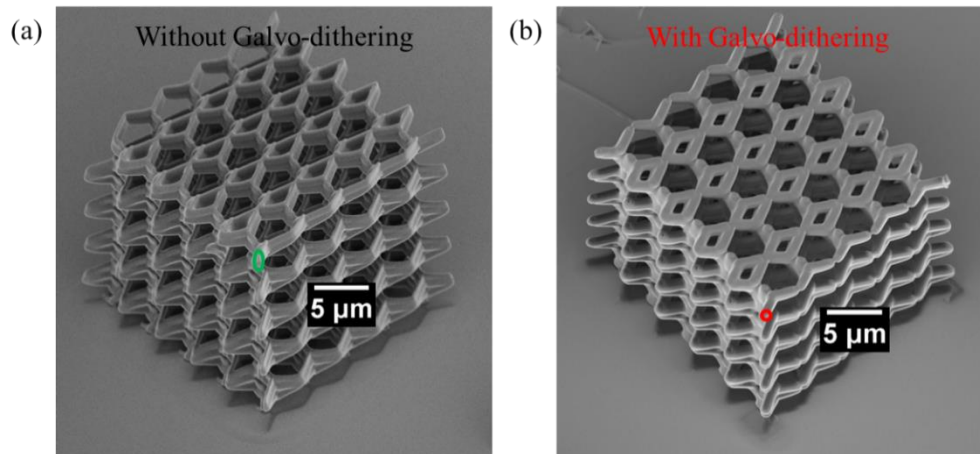


Figure 4.8: Fabrication results showing SEM images of Steiner tree networks without and with galvo-dithering. Each microstructure contains a rectangular $5 \times 5 \times 5$ array of unit cells with unit cell size $5 \mu\text{m}$. (a) Steiner tree structure fabricated without galvo-dithering. (b) Steiner tree structure fabricated with galvo-dithering.

The impact of GD DLW on the cross-section of 3D microstructures can be seen in Figure 4.8, which shows SEM images of two fabricated structures, both fabricated with laser power of 0.5 mW and writing speed of $50 \mu\text{m/s}$.

First, galvo-dithering produces a smoother structure with a better circular-shaped cross-section. This effect is marked in Figure 4.8 (a) and (b) using two different colours. Quantitatively, we measured the cross-section aspect ratio of the structure to compare the effect. Figure 4.8 shows a SEM image of a Steiner tree structure without galvo-dithering by traditional DLW. The z -direction and x - y plane linewidths of the structure are $D_z = 1150 \text{ nm}$ and $D_{xy} = 398 \text{ nm}$, producing an aspect ratio of $e = 2.889$. In comparison, Figure 4.8 (b) shows the corresponding SEM image for a Steiner tree structure fabricated with GD DLW. Z -direction and x - y plane line widths of the structure are $D_z = 954 \text{ nm}$ and $D_{xy} = 968 \text{ nm}$ respectively, corresponding to an aspect ratio of $e = 0.985$.

4.4.3.2 Improvements in mechanical properties and fabrication feature size

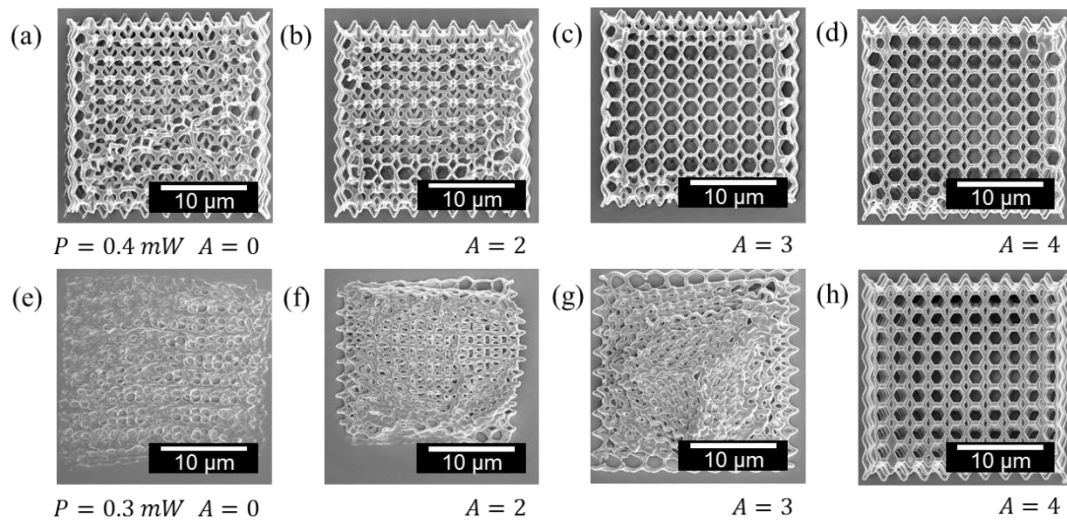


Figure 4.9: SEM image of Steiner tree structures fabricated by 3D DLW with galvo-dithering in the zirconium photoresist, showing the advantageous influence of galvo-dithering in reducing the shrinkage effect. (a)–(d) and (e)–(h): with laser power fixed to $P = 0.40$ mW or 0.3 mW, shrinkage in microstructures dramatically reduces as the galvo-dithering amplitude increases. In particular, when we use the lowest laser power of $P = 0.30$ mW, microstructures fabricated by DLW without galvo-dithering (where $A = 0$) could not sustain the shrinkage (Figure 4.9 (e)). Introducing galvo-dithering to the fabrication, 3D microstructures become stronger and are able to balance the shrinkage effect (Figure 4.9 (e)–(h)).

In addition to capability in achieving circular-shaped cross-sections, the use of GD DLW enables improvements in mechanical stability and fabrication feature size. Parameters, such as laser power (P), writing speed (s) and galvo-dithering amplitude (A), are very important in this process. To demonstrate the effect of galvo-dithering, microstructures were fabricated by varying two parameters (laser power (P) and galvo-dithering amplitude (A)). When laser power increases, shrinkage of the microstructures reduces (see Figure 4.9)-this is because the polymerisation ratio increases along with the laser energy dose, and increases the filling fraction of the microstructures, leading to stronger mechanical strength. For the lowest power of 0.3 mW, the effect of galvo-dithering helps to increase mechanical stability by introducing more energy dose in fabrication and reducing the shrinkage effect for very slender microstructures.

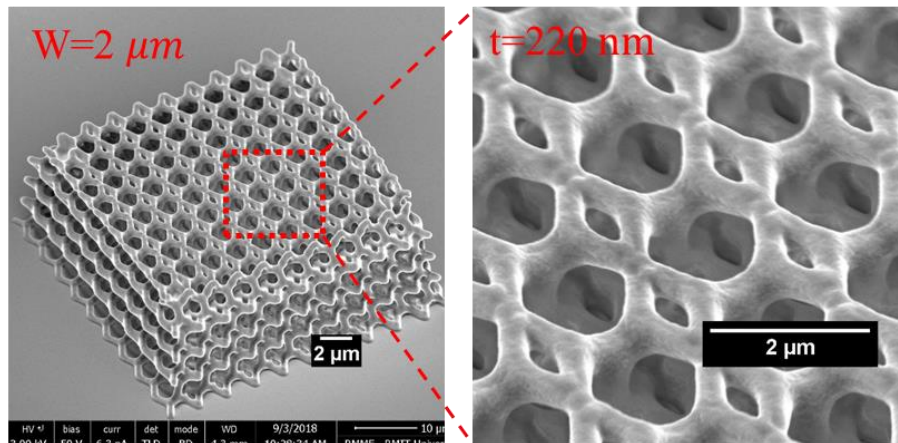


Figure 4.10: SEM image of Steiner tree structures in the zirconium photoresist demonstrating the advantageous influence of galvo-dithering on the reduction of fabrication feature size. Laser powers of $P = 0.30$ mW, laser speed of 15 $\mu\text{m/s}$ and galvo-dithering diameter 150 nm (corresponding to galvo amplitude of $A = 3$).

In addition, galvo-dithering can assist the fabrication of microstructures with smaller fabrication feature size. As shown in Figure 4.10, with the lowest laser power of 0.30 mW and galvo-dithering amplitude of $A = 3$, the structure feature size is around 200 nm. First, compensation of voxel z-direction using galvo-dithering can add extra mechanical stability to the microstructures. Second, the dithering process increases the polymerisation ratio of the photoresist and improves the mechanical stability of the structures fabricated by very small laser power.

4.4.3.3 Steiner tree structures with various relative densities

A series of Steiner tree structures are fabricated by tuning the fabrication conditions, such as laser power P , writing speed s , and galvo-dithering diameter D . Our fabricated results are characterised by SEM to determine the beam diameter and structure size after the fabrication. The relative density of our fabricated results is mathematically calculated out using the formula in Section 4.2.3. As what we can see, each of our fabricated structures maintained very good structural integrity. The fabrication feature sizes (beam diameter) are 220 nm, 288 nm, 324 nm, 346 nm, 394 nm, and 431 nm, corresponding to the relative densities of 5.05%, 6.81%, 8.73%, 10.70%, 12.81% and 14.84%.

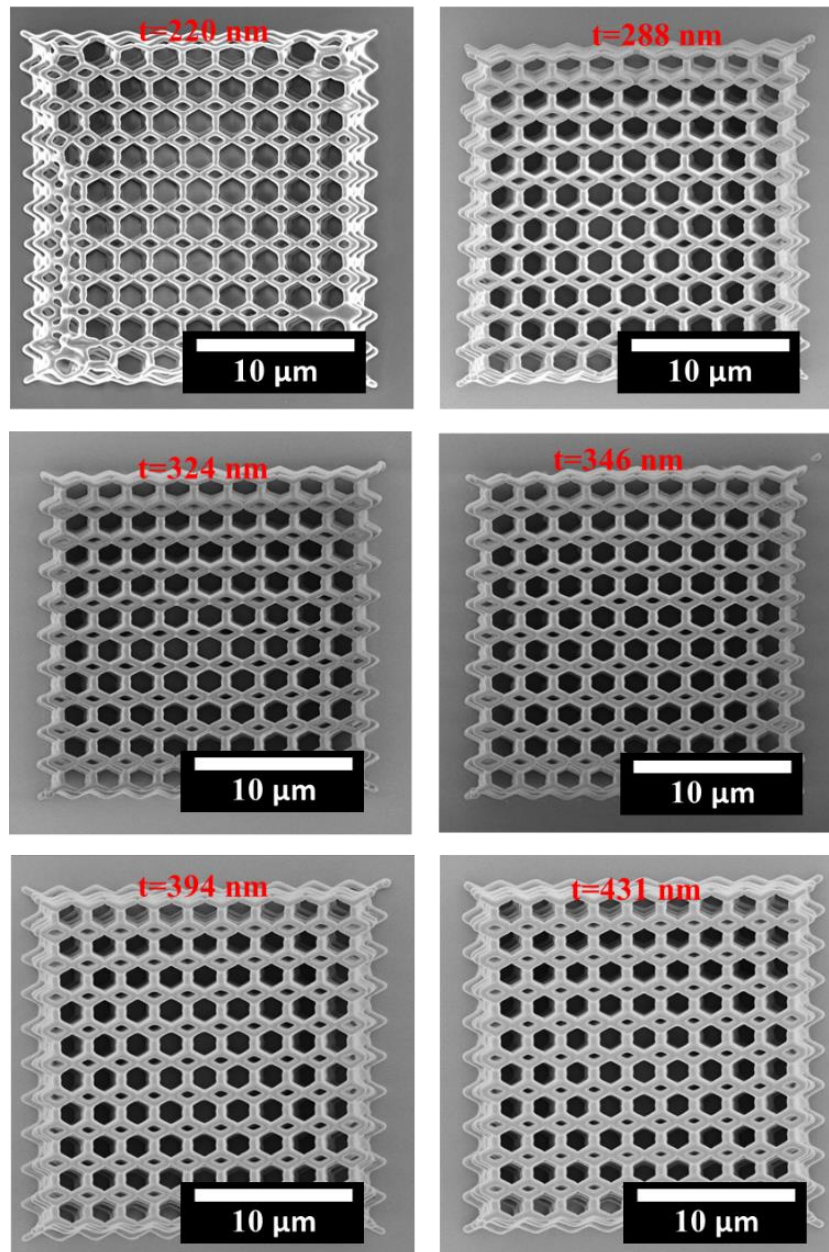


Figure 4.11: Fabrication results of Steiner tree structures with different relative densities. Unit size of 2 μm (scale bar 10 μm). Corresponding beam diameters are 220 nm, 288 nm, 324 nm, 346 nm, 394 nm, and 431 nm.

4.5 Characterisation of Mechanical Properties of 3D Steiner Tree Structures

To characterise the mechanical properties of our fabricated Steiner tree structures, it is essential to understand the mechanism in mechanical properties for artificial 3D low-density structures. In this section, we introduce the principle in defining the properties

and discuss factors that influence the mechanical properties and rigidity of Steiner tree structures.

4.5.1 Theoretical discussion of mechanical properties of Steiner tree structures

Similar to previous low-density structures or 3D architected lattice structures, such as low-density foams and low-density lattices, which have been investigated in great detail over the past several decades, the mechanical properties of Steiner tree lattices rely on the properties of constituent material, geometry of the structures and relative density. Two significant mechanical characteristics, Young's modulus and yield strength, are known to follow a power law scaling with the relative density as

$$E \sim B \times E_s \times \bar{\rho}^m \quad (4.3)$$

$$\sigma_s \sim C \times \sigma_{ys} \times \bar{\rho}^n \quad (4.4)$$

Here, E_s is the Young's modulus of the constituent material, and σ_{ys} is the yield strength, B and C are proportional coefficient constants and the exponents m and n are defined by the distribution of constructing beams in the geometry. Classical theories of the mechanics of 3D low-density structures are built on the assumption that the mechanical properties of constituent material remain scale-invariant, which means that the relative Young's modulus and yield strength of a given structure with the same geometry and constituent material remains unchanged regardless of its absolute size. Therefore, the mechanical characteristics of our Steiner tree structures rely on the following three aspects:

- the properties of the bulk material of which the lattice is made
- the geometry and shape of the cell struts and faces
- the relative density, $\bar{\rho}/\rho_s$, of the lattice structure, where $\bar{\rho}$ is the density of the lattice structure and ρ_s is the density of the constituent material.

However, as discussed in the literature review, the value of the exponents in Equations (4.3) and (4.4) rely on the rigidity of the lattice structure. In the following section, a discussion of the rigidity of Steiner tree structure is given.

4.5.2 Theoretical discussion of the rigidity of Steiner tree structures

According to traditional 3D low-density structure theories, two main categories of geometries exist with different mechanical responses: stretching-dominated (rigid structures) and bending-dominated (non-rigid structure). As the most important concept in defining the mechanical behaviour of low-density materials, a stretching-dominated structure is stiffer and stronger for a given mass, while a bending-dominated structure is relatively soft but absorbs energy better when compressed. To understand the rigidity of a Steiner tree structure and determine whether it is stretching-dominated or bending-dominated, a general principle, the Maxwell stability criterion, needs to be introduced.

The Maxwell stability criterion was introduced in 1864 by James Maxwell [93]. It describes the stability of a structure consisting of bars connected by pin-joints. The argument behind the Maxwell stability criterion is that, for a given structure with joints and beams, rigidity depends on the kinematic constraints in dimensions or the connectivity between the struts.

As described in the Maxwell criterion, a structure with j frictionless joints and b beams subject to k kinematic constraints in d dimensions is considered. With these, a structure has the potential to be rigid if it satisfies the equation:

$$dj - b - k \leq 0 \begin{cases} d = 2 \text{ in } 2D \\ d = 3 \text{ in } 3D \end{cases} \quad (4.5)$$

This equation is a necessary but not a sufficient condition to determine the rigidity of a low-density structure. To make the equation more accurate, structural mechanisms and states of self-stress must be accounted for [94]. For a structure with m mechanisms and s states of self-stress, Equation (4.5) can be generalised to:

$$dj - b - k = m - s \quad (4.6)$$

A structure that is rigid will have $m = 0$, and a structure is non-rigid will have $m > 0$. It is not possible to determine the number of mechanisms or states of self-stress from this equation, but if either is known, it is possible to determine the other.

In the case of the Steiner tree structure, as we can see from Equation (4.5):

$$dj - b - k = 16 > 0 \quad (4.7)$$

Our designed Steiner tree structure is a bending-dominated structure, corresponding to a non-rigid mechanical property. With this in mind, it is possible to assess the mechanical properties of Steiner tree structures from experiment tests and mathematical simulations.

4.5.3 Finite element simulation of the Young's modulus of Steiner tree structures

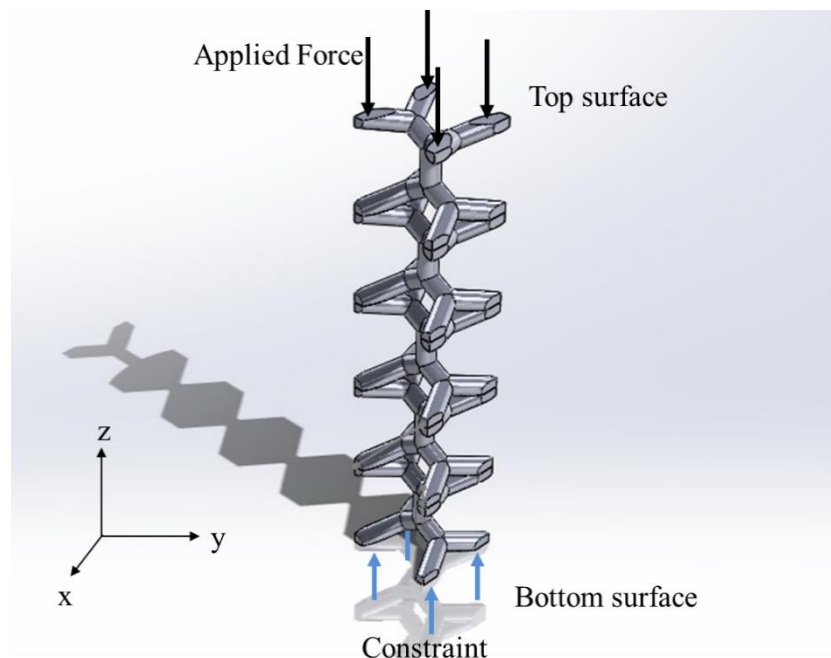


Figure 4.12: Simplified 5×1 unit structure modelled by Solidworks used in FEM and illustration of the simulation set up of the force and constraint on the simplified 5×1 unit structure.

FEM simulations of the uniaxial compression of our Steiner tree structure were performed using software ABAQUS, a commercial finite element simulation software. Full-scale simulations of lattice structures consume prohibitive computational memory, therefore, our 5×1 cells were chosen to simulate 5×1 cell structures (see Figure 4.12) along with periodic boundary conditions. The linear elastic solver in ABAQUS was chosen to simulate the Young's modulus of our lattice structures. The structure was modelled using CAD Solidworks to obtain a geometry

that is precise enough and can represent the real structure. A C3D10 10-node quadratic tetrahedral element was chosen to mesh the model during the simulation (the Young's modulus of the constituent polymer was obtained using atomic force microscope (AFM) in Appendix B). A constraint boundary condition was applied to the bottom surface of the simulated structure (see Figure 4.12) according to the following steps:

1. For each node on X^- face: find matching node on X^+ face.
2. Constraint in-plane displacements: $U_x^+ = U_x^-$, $U_y^+ = U_y^-$.
3. Repeat this process for Y faces.

Rotational degrees of freedom were not considered for solid structures. The Young's modulus of the simulated structure was defined as the ratio between the average strain and the average stress of the unit cell in the z-direction, where F is the applied force on the structure and L is the height of the structure:

$$E = \frac{\sigma_{avg}}{\varepsilon_{avg}} = \frac{F}{L\Delta z} \quad (4.8)$$

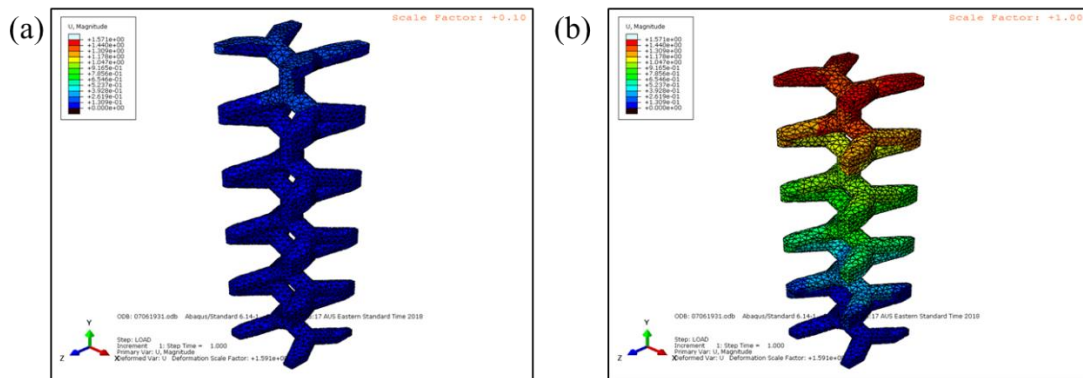


Figure 4.13: Finite element analysis of a 5x1 simplified structure with the beam diameter of 430 nm with relative density of 15%. (a) Meshed model for FEM simulation, with 5x1 unit structure when no compression force is applied. (b) 5x1 unit structure after linear elastic compression using external force.

As observed during the FEM simulations, the 5x1 simplified lattice structure experienced the linear compression deformation along the z-direction under the

applied force of 10000 μN , which is the same as our experimental condition. In addition, the Young's modulus of the material in our simulation was defined as 2 GPa for the polymer material. The Poisson ratio is 0.3. The size of the designed unit in our simulation is 2 μm . It is important to note that ABAQUS is a dimensionless simulation software; therefore, all values used in our FEM simulation are defined as proportional and consistent with each other.

Table 4.1: FEM simulation results of the Young's modulus of the microstructures.

Diameter (nm)	Relative density	Δz	Calculated modulus (MPa)
430	0.15	43.04	286.45
390	0.13	22.33	179.77
345	0.11	13.68	149.87
325	0.09	9.25	98.55
280	0.07	6.68	58.30
220	0.05	5.05	28.87

Our theoretical simulation results are summarised and shown in Table 4.1. As can be seen, the calculated modulus of the Steiner tree structures changes with relative density. Structures with smaller relative densities experience larger shape change in the z-direction compared with those with larger relative densities, corresponding to smaller modulus from our calculation. This is in agreement with our theoretical discussion in Section 4.5.1.

4.5.4 Experimental characterisation of Steiner tree structures

4.5.4.1 Experimental set up of measurement of Steiner tree microstructures using nano-indentation

For the experimental characterisation of 3D Steiner tree microstructures, we use the Hysitron TI 950 TriboIndenter. The Hysitron TI 950 nanoindenter system incorporates a powerful measurement module and advanced control module, which dramatically enhance the accuracy of mechanical measurement and provide unprecedented low-noise performance.

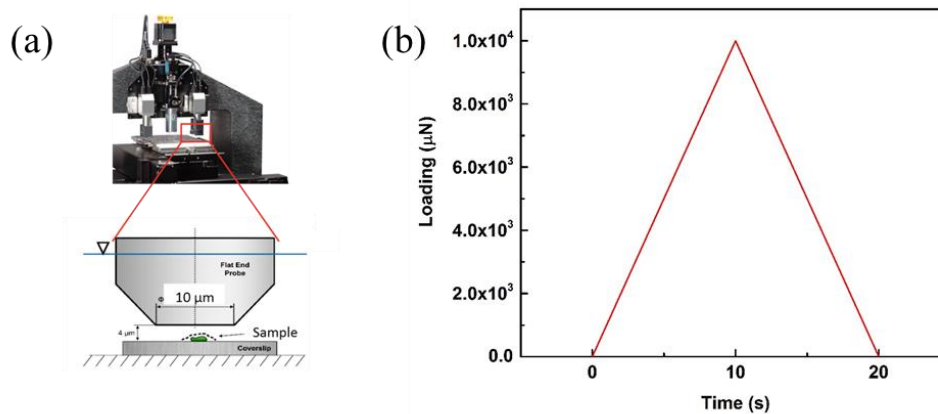


Figure 4.14: Illustration of the measurement of Steiner tree microstructures. (a) Experimental set up of the measurement of the Steiner tree microstructures using a flat-end probe. (b) Definition of the loading force as a function of time during the test used in nanoindentation.

As can be seen from Figure 4.14 (a), we used a flat-end punch from Bruker to test the whole structure's response to the loading force (shown in (a)). The loading force is defined as a function of time, with a loading speed around $1000 - 2000\ \mu\text{N}/\text{s}$ (depending on the tested sample). By collecting the load-displacement/stress-strain signal from the nanoindentation, the mechanical properties of the microstructures can be obtained.

4.5.4.2 Experimental results

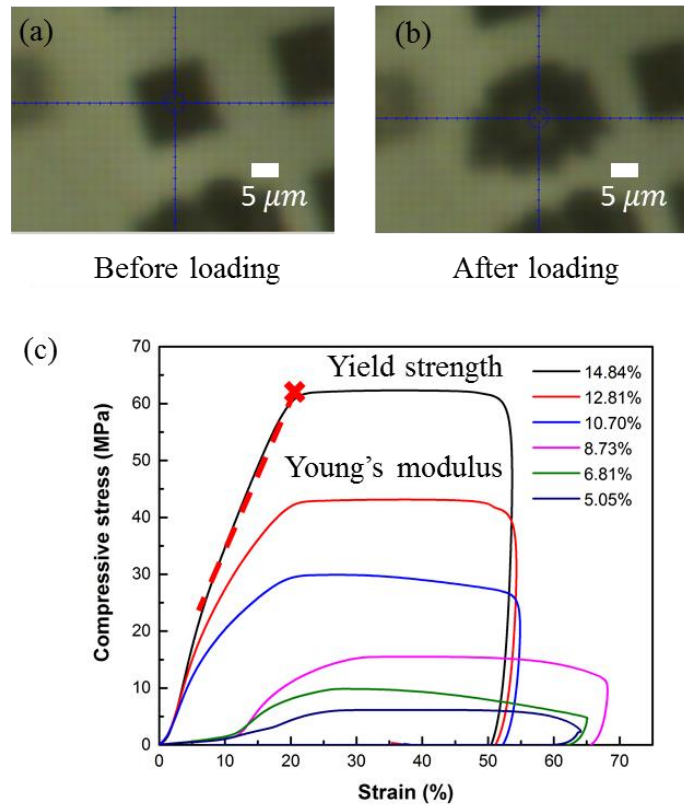


Figure 4.15: Experimental characterisation results of microstructures. (a) Undeformed structure under the built-in optical microscope before the compression test. (b) Deformed structure after the yield point indicated in the graph. (c) Compressive stress-strain data obtained from nanoindentation system for Steiner tree microstructures with different relative densities, corresponding to microstructures shown in Figure 4.11.

As shown in Figure 4.15(c), the compressive stress and strain curves showed that all samples with different relative densities have similar mechanical behaviours. In Samples 1–6, the compressive-strain curve of each sample starts with a toe region, the result of the mismatch between the probe and the sample. Afterwards, a linear elastic pattern is found in each sample. When the strain increases to a certain point, around 20% of the size of the structure (corresponding to peak stress), a catastrophic collapsing phenomenon can be observed. This large strain displacement demonstrates that the nanoindenter controller was unable to keep the probe at the prescribed displacement rate, which is a result of the inertia of the testing system. The before- and post-deformation images of the structure show our micro-lattice structures

experienced the whole process of nanoindentation. The elastic modulus, or the Young's modulus, of the structures were defined by the slope of the compressive stress-strain data in the linear region. The yield strength of the structures is defined as the largest load value before the collapsing of the structures (see Figure 4.15).

Here, we introduced a consistent criterion to measure the Young's modulus of the data obtained from the compression experiments, because the data obtained have varied stress-strain responses. As shown in Figure 4.15, the compressive stress-strain curves for samples tested consist three different regions: toe, linear and failure regions. At the beginning of the loading process, there is a nonlinear segment of the data called "the toe region", which arises from the misalignments and imperfections between the sample and the indenter probe. After the toe region, a linear region can be observed, demonstrating that the samples experienced a linear shape change along the compression direction. The Young's modulus of the structure is defined as the maximum slope of this linear region. In our samples, a 0.02% strain offset is taken to fit the Young's modulus of the samples (see Figure 4.15 (c)). The yield strength of the sample is defined as the intersection of this line and the stress-strain data.

Table 4.2: Obtained Young's modulus and yield strength data from compression test for 3D Steiner tree microstructures with different relative densities.

Relative Density (2 μm unit size)	Modulus (MPa)	Modulus Std. Dev. Average	Yield strength (MPa)	Strength Std. Dev. Average
14.84%	284.2	10.7%	61.6	15.6%
12.81%	181.4	12.3%	42.7	12.1%
10.70%	168.7	9.4%	29.7	13.5%
8.73%	87.3	13.4%	15.1	15.1%
6.81%	43.1	6.3%	9.8	19.5%
5.05%	37.1	15.6%	5.9	13.5%

Our experimental characterisation shows that samples with smaller relative densities reach their collapsing points very quickly compared with samples with larger relative densities. For instance, the sample with relative density of 14.84% experienced a linear elastic shape change until 22% of the strain, while the sample with relative density of 5.05% could only sustain less than 10% of the strain applied.

In addition, different lattice structures with different relative densities have different compressive stress-strain curves, which shows that mechanical properties rely on relative density. The lattice structure with the largest relative density of 14% (black curve) has the largest slope during loading, corresponding to a Young's modulus of $E = 287.7 \text{ MPa}$, compared with the structure with small relative density of 5% (purple curve), for which $E = 37.1 \text{ MPa}$. The Young's modulus and yield strength of the lattice structures change along with relative density. As discussed in Section 4.3, the relative density is a function of unit size and the beam diameter, and therefore, the mechanical properties such as Young's modulus and yield strength rely on the slenderness of the structure. Discussion and comparison between experimental results and simulation in the following sections confirm this.

4.5.5 Comparison between experimental results and FEM simulation

4.5.5.1 Young's modulus scaling with relative density

As can be seen from Figure 4.16, the Young's modulus of all the Steiner tree micro lattices follows a power-law scaling with relative density of $E = 0.151 \times E_s \bar{\rho}^{2.089}$. This scaling is similar to traditional lightweight and ultralight bending-dominated structural materials, whose properties scale around $E \sim E_s \bar{\rho}^2$ or $E \sim E_s \bar{\rho}^3$ [93]. The results follow the analytic prediction for an ideal non-rigid bending-dominated structure, $E \sim E_s \bar{\rho}^2$ (for further discussion, refer to Appendix C).

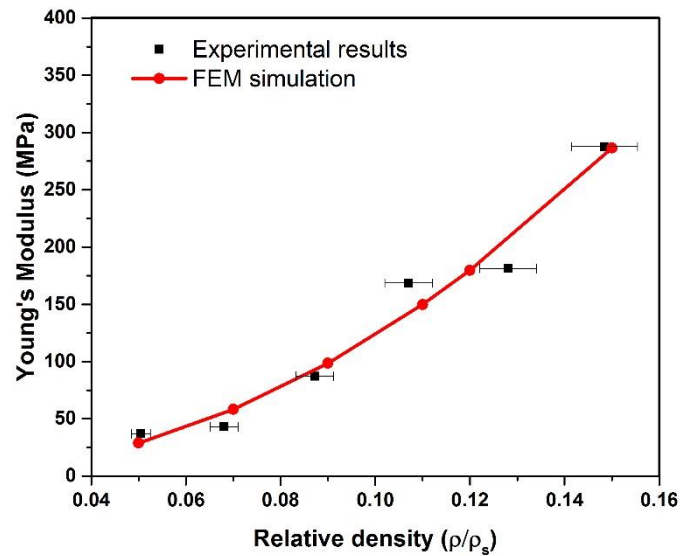


Figure 4.16: Measured Young's modulus of Steiner tree microstructures as a function of relative density. A power-law scaling with relative density can be seen.

There is very good agreement between the experimental results and the finite element method simulations of the Young's modulus of the structures. This close agreement between the experimental results and the simulation results indicates that the linear elastic model is able to sufficiently simulate the linear behaviour observed in experiment. These results of the power law scaling relationship between Young's modulus and relative density of the structure correlate well with several other research results in non-rigid structures (summarised in Appendix C). The Young's modulus of the Steiner tree structures fabricated by 3D DLW depends on the slenderness of the structure, or the diameter achieved in the fabrication process.

The difference between the FEM simulation and our experimental results can be a result of by several reasons, such as the ellipticity of the beams due to the mismatch of galvo-dithering and laser fabrication condition, structural imperfections resulting from fluctuation of the laser energy dose, and mismatch during compression probe and the samples. In our case, this deviation is primarily attributed to the joint connection of the beams, which affects the relative density of the structures, where the mathematically calculated relative density can be adjusted [100] according to the node interference.

4.5.5.2 Yield strength scaling with relative density

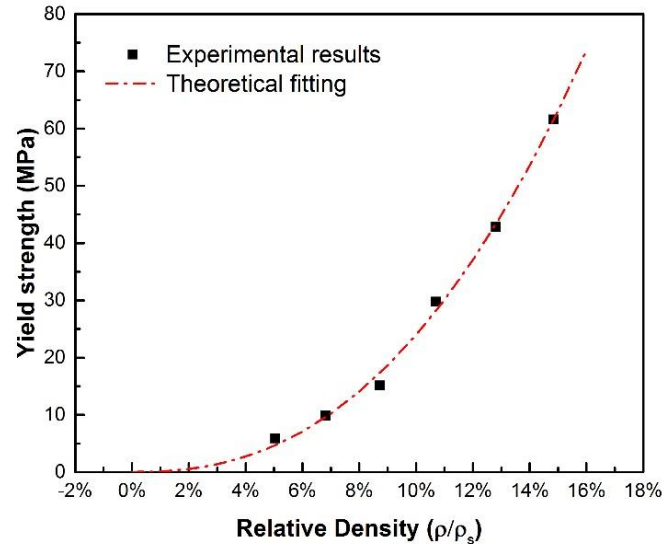


Figure 4.17: Yield strength of fabricated 3D Steiner tree microstructures as a function of relative density. Black dots are experiment results from compression test. Dashed red line is the theoretical fitting.

Similar to many research results, the yield strength of the fabricated Steiner tree microstructures follows a power-scaling law $\sigma = 5.863 \times \sigma_s \bar{\rho}^{2.388}$. This result is reasonable as the Steiner tree structure is a bending-dominated structure. As a bending-dominated structure, the yield strength of the Steiner tree structure depends on the bending and buckling of the geometry units. The yield strength of our micro-lattice structure is a result of beam buckling of a truss member [97].

4.6 Conclusion

In this chapter, we explored the design, fabrication and characterisation of the mechanical properties of neuron-inspired Steiner tree structures fabricated by 3D DLW at the sub-micrometre scale.

The biomimetic design of regarding the neuron as a mentor corresponds to the ‘Steiner tree problem’ in mathematics, described in 1876 by Swiss mathematician Jakob Steiner (1796–1863). Compared with traditional lattice structures such as Kelvin foam, gyroid structures, octet trusses, Kagome trusses and recently proposed

Shelluar structures, which are inspired by the minimal surface in nature (see Figure 2.6), neuron-inspired Steiner tree structures are designed in line with the principle of ‘shortest connection distance’. Therefore, it has the lowest relative density (four times lower) of the four traditional lattice structures. Consequently, the principle inspired by BNNs—the shortest connection distance—could be an alternative to design ultralow-density microstructures.

In addition, our proposed neuron-inspired Steiner tree structures were fabricated by 3D DLW to achieve different relative densities by tuning the beam diameter of the microstructures. The major challenges we faced in this fabrication were how to fabricate stable microstructures with smaller feature size and how to achieve a circular-shaped beam cross-section in the microstructures. By introducing a galvo-dithering DLW system based on previous work, stable Steiner tree structures with the smallest feature size of 200 nm can be fabricated with a circular-shaped beam cross-section. The relative densities of our fabricated Steiner tree structures range from 5% to 15% of the bulk material.

The size effect of our Steiner tree structures was thoroughly studied and confirmed theoretically and experimentally. The experimental and simulation characterisation of the Steiner tree structures showed that they possess tuneable mechanical properties (Young’s modulus ranges from 25 MPa to 300 MPa, and yield strength ranges from about 5 MPa to 65 MPa) that are in the range of biological neuron tissue and are promising for future applications in neuron tissue engineering. In addition, the ultralow-density features of the microstructures fabricated by galvo-dithering DLW provide a novel design for ultralow-density materials, which are of great potential in applications such as biomedical engineering, filters and energy storage.

In summary, by regarding biological neurons as mentors, we introduced a novel type of nature-inspired low-density structure: neuron-inspired Steiner tree structures. The unique structural feature of Steiner tree structures is endowed with an ultralow-density feature and mechanical properties, which are of great importance to applications in many fields.

Chapter 5: Design, Fabrication and Characterisation of Hydrogel Microstructures Using Three- dimensional Direct Laser Writing

5.1 Introduction

As an attractive biocompatible material having similar structural and biochemical characteristics to those of neuron tissues, hydrogels have been widely studied and utilised in many fields, such as biosensors and tissue engineering. In addition, hydrogels have outstanding cytocompatibility as well as low cellular damage when used in tissue engineering. In addition, hydrogels are regarded as crosslinked networks constructed by hydrophilic monomers. Due to the existence of macromolecular pores in hydrogel networks, hydrogels provide high diffusion and transportation for nutrients, oxygen and cellular waste. Moreover, the mechanical characteristics of hydrogels can be tuned to fit those of biological tissues.

Compared with conventional nanofabrication methods, 3D DLW possesses many advantages, which include cost-effective fabrication, simple design of structures and high fabrication resolution in 3D space. These advantages have enabled a vast range of applications, such as nanophotonics, biomedical engineering and solar cells.

As BNNs possess substantial complexity, it is becoming increasingly important to develop hydrogels suitable for fabrication of well-defined structures and adjustable biocompatible functions. To this end, one promising method is to utilise 3D DLW based on TPP in combination with photosensitive hydrogels. Integration of 3D DLW with biocompatible hydrogels has shown its great potential in tissue engineering applications, such as in situ cell encapsulation and spatial and temporal immobilisation of bioactive ligands.

In this chapter, based on our previous work [191] published by Dr Haibo Ding (Southeast China University), we demonstrate the design, fabrication and characterization of a novel biocompatible hydrogel and 3D hydrogel microstructures fabricated using 3D DLW based on TPP. Our biocompatible hydrogel consists of 2-hydroxy-2-methylpropiophenone (HMPP) as the photoinitiator and poly (ethylene glycol) diacrylate (PEGDA) as the monomer. The photopolymerisation properties of the hydrogel were demonstrated by fabricating various 3D microstructures. The optimal fabrication conditions of our hydrogel are confirmed by fabricating woodpile structures. The mechanical properties, such as hardness of these hydrogel microstructures depend on the degree of polymerisation, which depend on laser power and writing speed. It is also demonstrated that reversible shape changes of these microstructures fabricated by 3D DLW can be tuned by external stimulus such water concentration using the swelling behaviour of hydrogel. Therefore, our demonstrated biocompatible hydrogels open a new avenue for 3D microstructure scaffolds fabricated by 3D DLW and will promote the utilization of 3D DLW in development of neuron tissue engineering.

5.2 Selection of Photoinitiator and Hydrogel Precursors

When designing a photopolymerisation system of hydrogel for 3D DLW based on TPP, a proper combination of photoinitiator and hydrogel precursors should be carefully designed to satisfy the following principles:

- The photoinitiator needs to have a high TPA cross-section in regard to the fabrication laser source (wavelength or frequency), to maintain high radical generation efficiency.
- Both photoinitiator and the hydrogel precursor should have good water solubility.

Detailed discussion is provided in the sections below.

5.2.1 Selection and characterisation of photoinitiators

As the primary component in a photopolymerisation system, selection of an effective photoinitiator is of great importance. First, the selected photoinitiator should possess a relatively high absorption efficiency at the wavelength of the laser used, which means the absorption spectrum of the photoinitiator is required to overlap that of the laser source. Second, the photoinitiator should have high efficiency in generating free radicals. This is very important because it will influence the polymerisation process. Many photoinitiators have been studied and utilised in designing photopolymerisation hydrogels and are shown in Chapter 2.

Due to the fact that the working wavelength of our femtosecond laser beam is 535 nm, it is convenient that our synthesised hydrogel work at the same wavelength. Consequently, 2-hydroxy-2-methylpropiophenone (HMPP) is an ideal candidate for the photoinitiator. HMPP has been widely studied and utilised as a photoinitiator in optical lithography using UV light [8,9] because of its high absorption efficiency in the UV region. In addition, HMPP has proved to have a high degree of biosafety in biomedical applications.

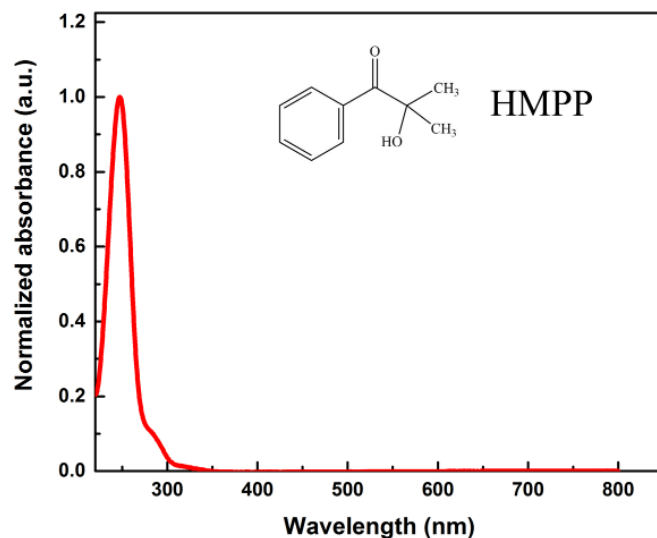


Figure 5.1: Absorption spectrum of photoinitiator HMPP measured using a UV-visible spectrometer.

As shown in Figure 5.1, HMPP has a single-photon absorption peak of 247.5 nm, corresponding to a two-photon wavelength at 495 nm, very close to our operating wavelength. The single-photon absorption spectrum of HMPP was obtained using a UV-visible spectrometer. The photoinitiator HMPP was bought from Sigma-Aldrich and used as received.

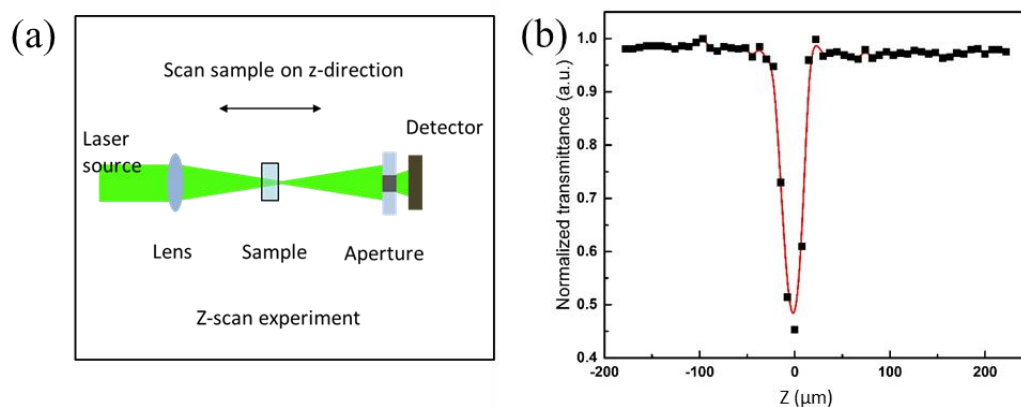


Figure 5.2: Illustration of the measurement of two-photon cross-section using the Z-scan method. (a) Set up for z-scan method. (b) Transmission spectrum of photoinitiator HMPP solution obtained using the z-scan method.

HMPP also exhibits very strong TPA at the wavelength of 535 nm. TPA cross-section of HMPP was measured using a z-scan system (see Figure 5.2). For z-scan measurements, deionised water was chosen as the solvent, as often described in the literature, to achieve a reliable reference and to test the z-scan device. Our laser source is a femtosecond laser from Fidelity with working wavelength of 535 nm, a pulse width of 270 fs and a repetition rate of 50 MHz. The incident laser power was measured using a digital power meter prior to each measurement before the sample.

Measurement of the two-photon cross-section of HMPP was conducted using the z-scan method. A schematic of the experimental set up is shown in Figure 5.2 (a). The sample solution was put between two cover glasses. A femtosecond laser beam was focused into the tested sample using a high NA objective (Olympus NA = 1.4) with a 150 mm focal length. After illuminating the sample, the transmittance signal was detected by a power meter. A Nano stage was used to move the sample along the z-direction. As shown in Figure 5.2 (b), the HMPP showed an absorption peak at the position of 0 (relative position), corresponding to the nonlinear absorption with a TPA cross-section of 4.5 GM at the excitation wavelength of 535 nm. The TPA cross-section was fitted based on the theory discussed in reference [192].

5.2.2 Selection of hydrogel precursors

In terms of chemical characteristics, the water solubility of hydrogel precursors is the primary factor when selecting precursors. To achieve this goal, polyethylene glycol (PEG) based synthetic polymers and several species of naturally achieved polymers such as gelatin and hyaluronan (HA) have drawn much attention due to their superior hydrophilicity. Second, the photoactivity of hydrogel precursors is of great importance in the fabrication capability in 3D DLW based on TPP. To fabricate a microstructure with feature sizes suitable for biomedical engineering applications (generally, millimetre to the centimetre scale), the photoactivity of precursors directly determines both laser power and writing speed during the laser fabrication process.

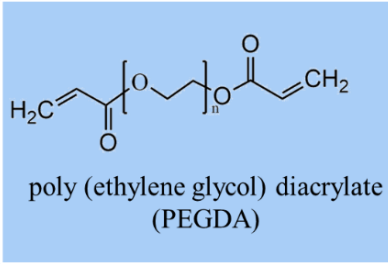
Further requirements of hydrogel precursors are summarised from a biological point of view:

- **Biocompatibility:** biocompatibility or low cytotoxicity is a favourable feature for in neuron tissue engineering applications. Hydrogel precursors used in this field are generally required to have very high biocompatibility or low cytotoxicity.
- **Bioactivity:** in addition to biocompatibility, hydrogel scaffolds produced by 3D DLW based on TPP should provide bio tissue with a physical appropriate environment and could support all bio functions that are occurring in vivo (such as cell migration, proliferation and differentiation).
- **Biodegradability:** The eventual goal of implantable hydrogel structures is to replace or repair injured bio tissues, therefore, the degradation characteristics of fabricated hydrogel structures should match the growth rate of biological tissues.

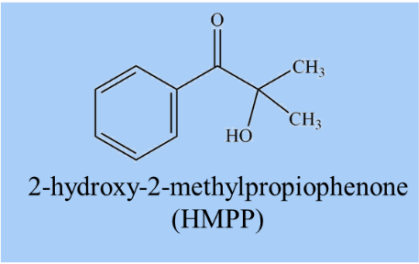
Based on these principles, we chose poly (ethylene glycol) diacrylate (PEGDA) as our hydrogel precursor. Poly (ethylene glycol) (PEG) hydrogels comprise 3D networks of polymer chains, which can swell in water and maintain their shape when dry. They have been investigated for many biological applications because of their biocompatibility, as well as the similarity of their hydration and flexibility to nature tissue. PEG is considered an excellent hydrogel material because of its low toxicity and limited immunogenic recognition following implantation or injection. PEG-based hydrogel systems are useful for a myriad of biological applications such as drug delivery carriers in pharmaceutical applications, scaffolds in tissue engineering and imaging, bioassays and biosensors in biomedical applications. Therefore, we chose PEGDA hydrogel as our precursor. PEGDA has an average molecular weight of 700 DA (see Figure 5.3 for the chemical structure).

5.3 Biocompatible Hydrogel Synthesis

components	V/V
PEGDA	59%
Deionized Water	40%
HMPP	1%



poly (ethylene glycol) diacrylate
(PEGDA)



2-hydroxy-2-methylpropiophenone
(HMPP)

Figure 5.3: Diagram showing components and volume ratio in synthesising HMPP + PEGDA hydrogel.

Our biocompatible hydrogel is a combination of HMPP as the photoinitiator (PEGDA) as the hydrogel precursor, because both has been proving to have a high degree of biosafety. The synthesis of our hydrogel follows the process described in [195]. A volume ratio of 59% of the monomer PEGDA (Sigma) is first added, and then 1% of photoinitiator HMPP (Sigma) is added into PEGDA. Afterwards, 40% of deionised water is added into the mixture. The whole mixture is then put into sonication for about 60 seconds to achieve an evenly mixed solution (components shown in Figure 5.3). The ratio of water can be tuned from lowest (0%) to highest (79%) from our tested results.

5.4 Two-photon Polymerisation Process

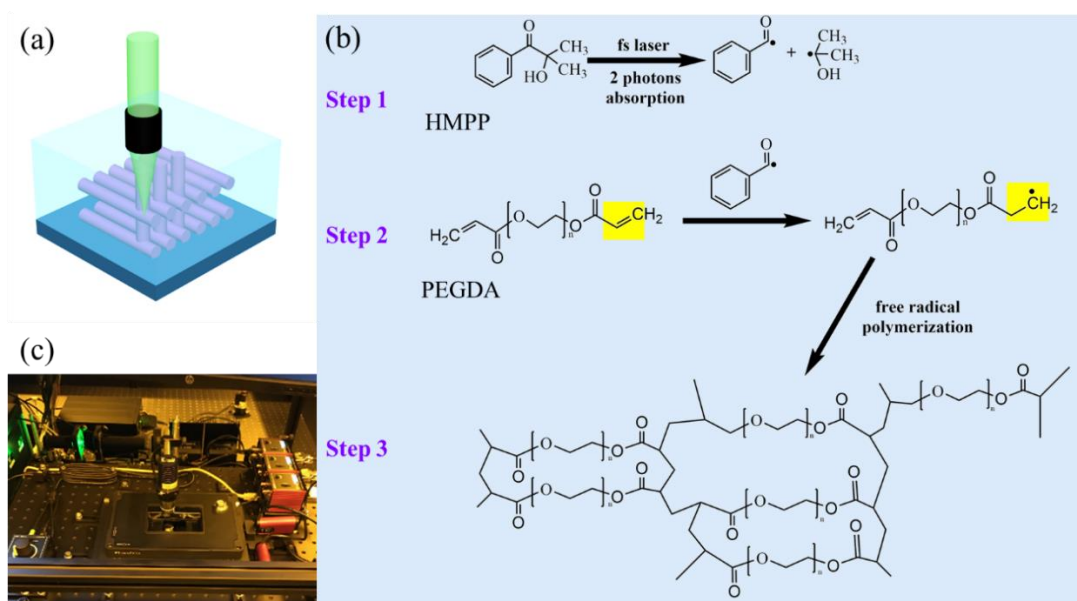


Figure 5.4: Illustration of TPP process in HMPP + PEGDA hydrogel. (a) Schematic showing 3D DLW of hydrogel. (b) Diagram showing the polymerisation process during TPP (confirmed by Haibo Ding). (c) Home-built 3D DLW system and fabrication process (LAIN RMIT).

The TPP process of PEGDA and HMPP hydrogel is achieved using our home-built 3D DLW system (see Figure 5.4 (c)). During the DLW process, a femto-second laser beam at wavelength of 535 nm is tightly focused into the hydrogel, causing the photoinitiator to absorb two-photon energy and generate radicals in the material (step 1). At the same time, the monomer PEGDA receives the radicals, causing the monomers to be polymerised through this free radical polymerisation process and generating long chains of larger molecules (steps 2 and 3). Thus, polymerised structures such as lines and dots can be fabricated in the hydrogel. After fabrication, the sample is rinsed in deionised water for 30 minutes to wash out the unpolymerised materials.

5.5 Experimental Confirmation of Two-photon Polymerisation

Hydrogel is a very sensitive material for laser fabrication. Fabrication conditions such as laser power and writing speed exert critical impacts on the fabrication of microstructures in hydrogel. First, as a thermal-sensitive material, too much laser

energy dose during fabrication gives rise to explosion of the material, resulting in bubbles and chemical decomposition. Second, the mechanical stability of microstructures fabricated in hydrogel is highly dependent on fabrication conditions. Inadequate energy dose from the laser beam will result in less crosslinked polymerisation, reducing the Young's modulus of the polymerised material and the deformation of the microstructures. Therefore, it is necessary to investigate optimal fabrication conditions in our hydrogel, such as laser power and fabrication speed, on the mechanical property of the HMPP + PEGDA hydrogel.

We chose the fabrication of woodpile structures as a demonstration to confirm the TPP process in our HMPP + PEGDA hydrogel and study the optimal fabrication conditions for our hydrogel. A 3D woodpile, a photonic crystal with tuneable structural colours, is a typical microstructure widely used in 3D DLW. The fabrication path of our woodpile structures is designed using a MATLAB code similar to those in related research.

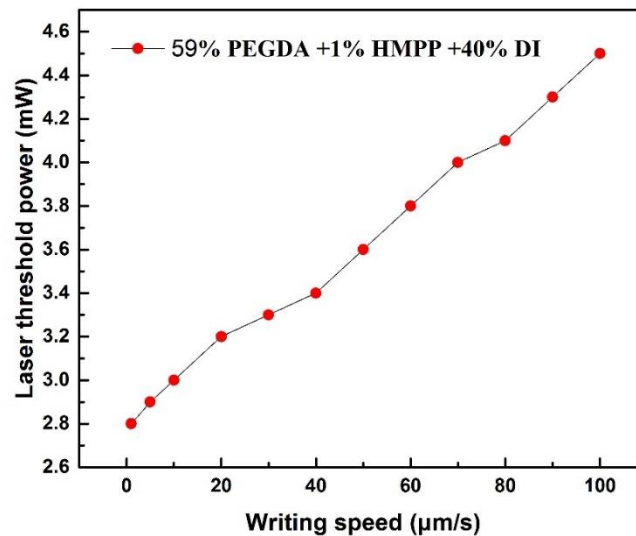


Figure 5.5: Experimental confirmation of the fabrication conditions of the HMPP + PEGDA hydrogel. Laser threshold as a function of writing speed in the HMPP + PEGDA hydrogel.

By sweeping the laser power and writing speed, the applicable fabrication conditions for our HMPP + PEGDA hydrogel are confirmed. From our experimental results,

several fabrication conditions can be used in the fabrication of microstructures in the HMPP + PEGDA hydrogel (see Figure 5.5). The HMPP + PEGDA hydrogel shows a very wide range of applicable fabrication conditions; the laser power can be adjusted from 2.8 mW to 4.5 mW and the writing speed from 1 $\mu\text{m/s}$ to 100 $\mu\text{m/s}$.

As a demonstration of the success of TPP in HMPP + PEGDA hydrogel, a series of woodpile structures were fabricated with laser power of 3.6 mW and at writing speed of 50 $\mu\text{m/s}$. Instead of choosing low fabrication speed with high power, or high speed with low power, our choice not only gave us a relatively high speed corresponding to a shorter fabrication time but provided a strong mechanical property in the microstructures. As shown in Figure 5.6, a series of woodpile structures were fabricated in the hydrogel with different periods. The woodpile structures maintained a very homogeneous shape and periods, with a very small amount of distortion resulting from the washing out process. Corresponding periods are 2 μm , 1 μm and 0.5 μm , with a whole structure size of 50 $\mu\text{m} \times 50 \mu\text{m} \times 20 \mu\text{m}$.

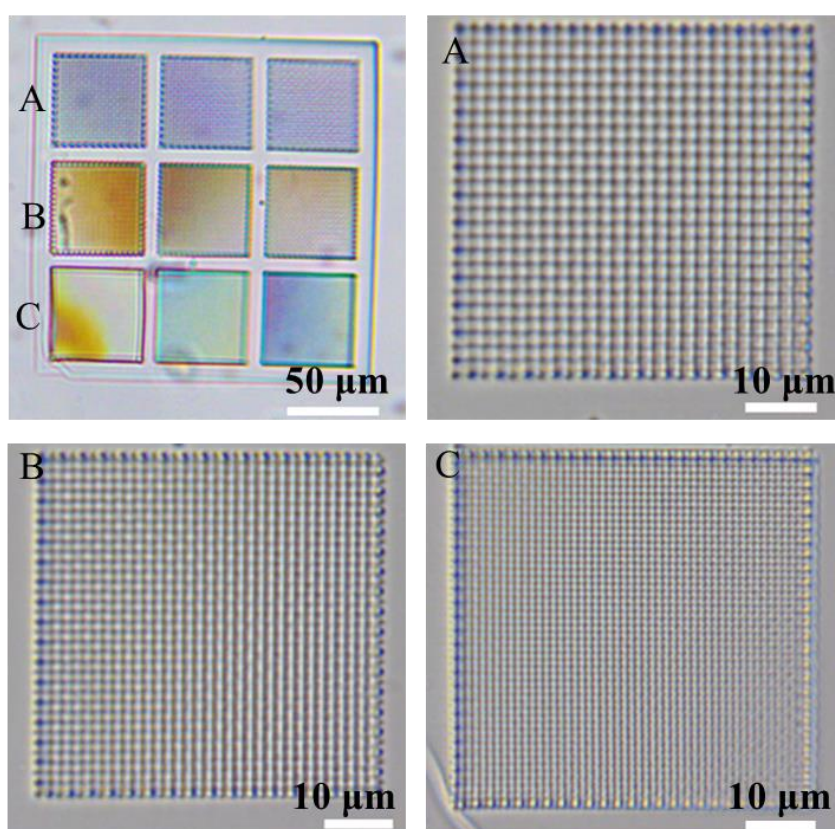


Figure 5.6: Optical images of fabricated woodpile structures with different periods in air to confirm optimal fabrication conditions for the HMPP + PEGDA hydrogel.

Fabrication conditions: laser power = 3.6 mW, writing speed = 50 $\mu\text{m/s}$. Corresponding woodpile periods are 2 μm , 1 μm , and 0.5 μm .

5.6 Characterisation of Mechanical Property of HMPP + PEGDA

Hydrogel

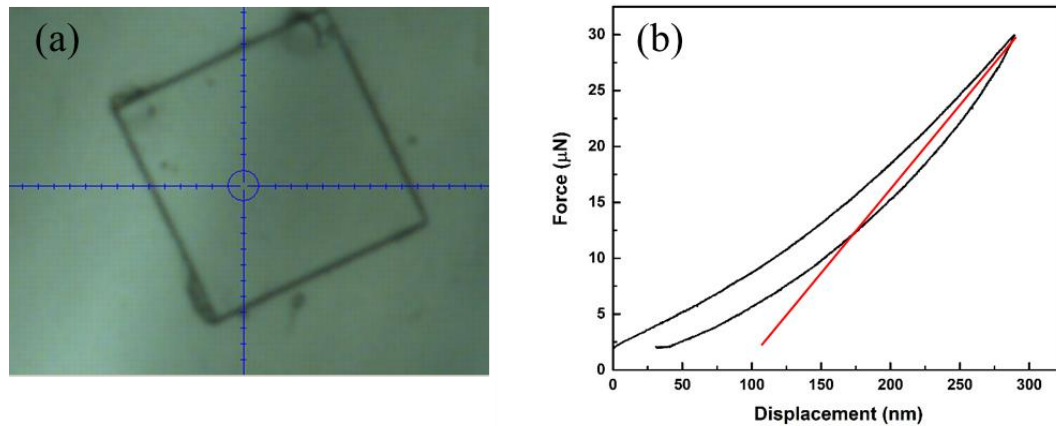


Figure 5.7: Illustration of the measurement of hardness of the HMPP + PEGDA hydrogel using nanoindentation. (a) Top view of the measurement of microcubic in Hyston nanoindentation. (b) Typical force-displacement data obtained from nanoindentation.

The mechanical property of the HMPP + PEGA hydrogel relies on the fabrication condition, such as laser power and writing speed. Therefore, microcubic structures with $60 \times 60 \times 5 \mu\text{m}^3$ (length, width and height of the cubic microstructure, respectively) were fabricated under various laser powers, to act as samples to study the Young's modulus of the hydrogel. A transmissive optical image of a 3D cubic microstructure fabricated with laser power of 3.6 mW, writing speed of $50\mu\text{m/s}$ and layer distance of 500 nm in the top view is shown in Figure 5.7 (a).

The hardness of the PEGDA hydrogel was experimentally characterised by nanoindentation (Bruker). The 5 μm Hystron flat-end probe was used. The loading force was a function of applied time with a maximum of 30 μN . All procedures follow the Hystron manual. Loading rate was 10-3 Hz. The hardness of the material is defined as the slope of the force-displacement curve during the withdrawing process (shown in the red line in Figure 5.7 (b)).

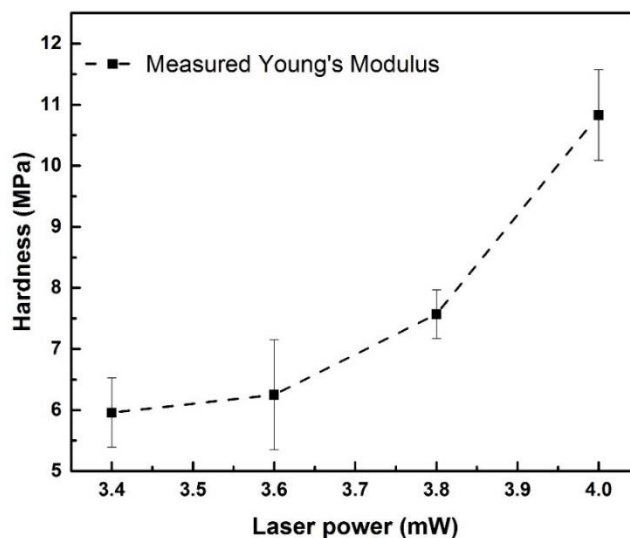


Figure 5.8: Measured hardness of PEGDA hydrogel as a function of laser power in air.

The hardness of the microcubic structures in air fabricated by different laser powers with a writing speed of 50 $\mu\text{m/s}$ in air is shown in Figure 5.8. The mean value of each data item was obtained by averaging multiple times the data at different test areas in one sample; the error bars are modulus deviations in the measurement data compared with the average value. As can be seen from Figure 5.8, the hardness of the hydrogel micro cubic structures relies on the fabrication laser power used. When the laser power increases from 3.4 mW to 4.0 mW, the hardness of the hydrogel increases from 6 MPa to around 11 MPa. In addition to our experimental results, laser power lower than 3.4 mW could not sustain the fabrication of 3D micro cubic structures because of the insufficient concentration of free radicals generated by TPA excitation, resulting in an inadequate polymerisation in the fabrication area. Theoretically, more free radicals could be generated by increasing the laser power; this would result in higher density of crosslinking and the obtained microstructure would be hard to deform. However, if the laser intensity becomes higher than 4.0 mW, micro-explosion could occur because of excessive heat from the laser source, and consequently, bubbles or even polymer decomposition would occur.

5.7 Characterisation of Swelling Property of HMPP + PEGDA Hydrogel

5.7.1 Swelling behaviour of hydrogel

The outstanding characteristic of hydrogels is their capability to shrink and swell when put in contact with a dynamically compatible solvent (water, for instance). When a hydrogel in its initial state is in contact with solvent molecules, the latter attacks the hydrogel surface and penetrates the polymeric network (as shown in Figure 5.9). Since the first time of observation of swelling and shrinking of hydrogel by Achilles et al. [142], the swelling property of hydrogel has been widely studied and utilised in many microdevice systems.

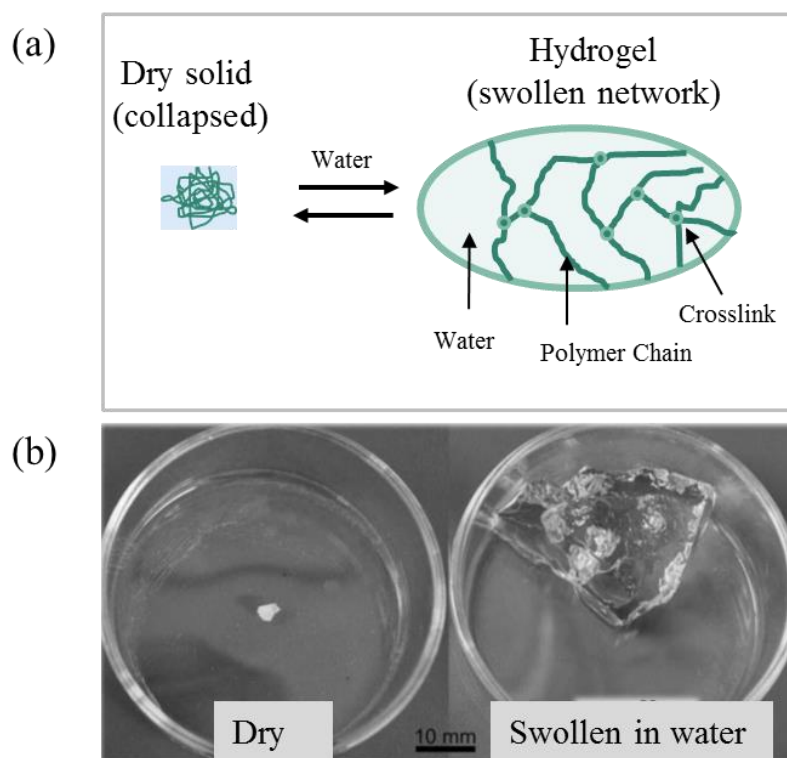


Figure 5.9: Representation of hydrogel stimuli responsive swelling and un-swollen with water content [193].

In this section, to study the swelling properties of the PEGDA hydrogel, we introduced a reversible shape microstructure fabricated by 3D DLW called a reversible ‘octagon to square’ structure. The design, fabrication and characterisation

of the microstructure was conducted along with investigation of the reversibility of the microstructure and the swelling behaviour of the PEGDA hydrogel.

5.7.2 Design of reversible ‘octagon to square’ structure

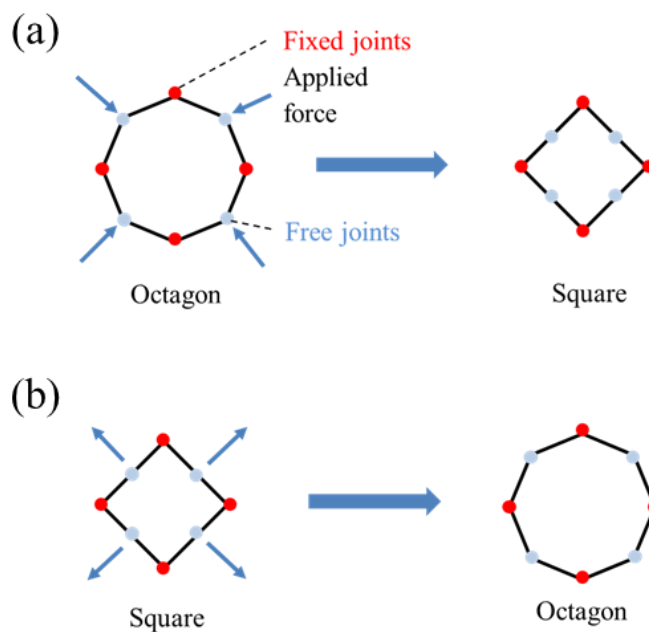


Figure 5.10: Design of ‘octagon to square’ reversible structure. (a) and (b) Mechanical analysis of reversible structures and the shape deformation process. Left: Octagon with four fixed joints and four free joints. Right: after the deformation, the octagon can change into a square.

We designed an ‘octagon to square’ reversible structure based on mechanics [194]. As shown in Figure 5.10 (a), the octagon has four fixed joints (shown in red) and four free joints (shown in light blue). When an external force is applied homogeneously on the free joints towards the inside of the octagon structure, the octagon gradually changes into a square. When external force is applied on the free joints outwards of the structure (as shown in Figure 5.10 (b)), the square changes gradually into an octagon. This behaviour is very important as, in the next sections, we show that the shrinking and swelling behaviour of the hydrogel acts as the driving force to change the structure at the micrometre scale.

5.7.3 Fabrication of reversible ‘octagon to square’ microstructures using 3D direct laser writing

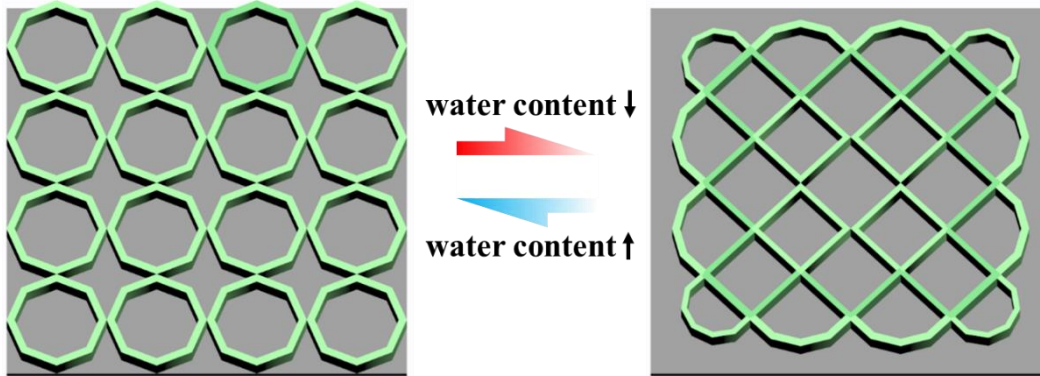


Figure 5.11: Design and fabrication of reversible ‘octagon to square’ microstructures. Each octagon is located in a $40\ \mu\text{m} \times 40\ \mu\text{m}$ square can that are connected to each other. The designed component block dimension is $5.5\ \mu\text{m}$. The designed thickness of the structures is $5.5\ \mu\text{m}$. The model is designed using Solidworks.

We designed a reversible ‘octagon to square’ microstructure that consists of an array of octagons (4×4) connected to each other (shown in Figure 5.11 (a)) using Solidworks. Each of the octagons is made of eight solid blocks connected to each other; the designed blocks have size $5.5\ \mu\text{m} \times 5.5\ \mu\text{m} \times 15\ \mu\text{m}$.

The microstructures were fabricated using a home-built 3D DLW system, which consists of the femtosecond laser operating at the wavelength of $535\ \text{nm}$ (as shown in previous chapters). The sample of our HMPP + PEGDA hydrogel was dropcasted on cover glass. By moving the sample using a piezo-nanostage, the microstructures were fabricated. The laser power we used in the fabrication was $3.6\ \text{mW}$ and writing speed was $50\ \mu\text{m/s}$. After fabrication, the sample was rinsed in de-ionised water for 15–30 minutes to wash out the unpolymerised hydrogel. The characterisation of the microstructures was performed using an optical microscope and measurement was conducted using ImageJ.

5.7.4 Fabrication results

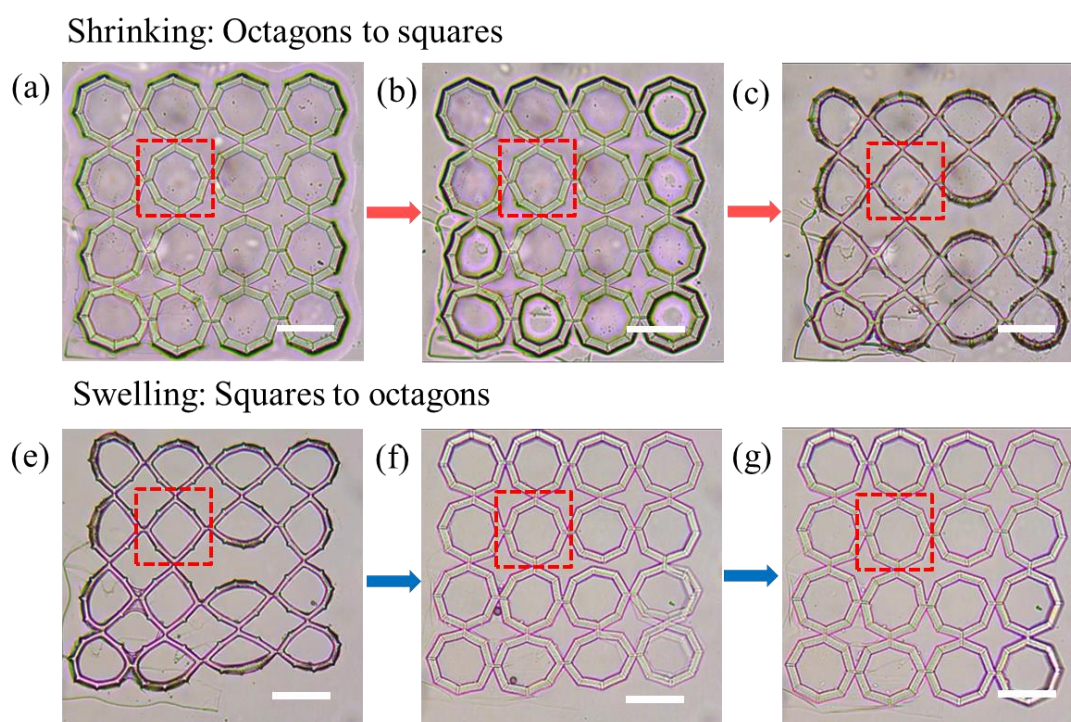


Figure 5.12: Transmissive optical images of reversible shaped microstructures fabricated by 3D DLW. (a)–(c) Shrinking process when the water content in the hydrogel is evaporating, during which, the whole structure shrinks from octagons to squares. (e)–(g) Swelling process when the hydrogel is absorbing water content, during which the whole structure swells from squares back to the original octagon shapes. Scale bar is 40 μm .

As shown in Figure 5.12, the reversible behaviour of the fabricated structures can be separated into two processes. One is from octagons to squares (from (a) to (c)) resulting from the shrinking effect of the PEGDA hydrogel, during which the water content is flowing out of the PEGDA hydrogel material. The second is from squares to octagons (from (e) to (g)) due to the swelling effect of hydrogel when water content is diffusing into the material. During the water evaporating and absorbing process of the hydrogel, the force resulting from water diffusion acts as the external force (similar to the process described in the previous section). Because of the swelling behaviour of the hydrogel material stimulated by the concentration of water content, the microstructure is expected to experience shape change as shown in Figure 5.12. Inside the microstructure, the octagons shrink into squares when the water content in the hydrogel material is evaporating. When the hydrogel material absorbs water, the

squares swell back to their octagon shapes. Therefore, a reversible shape microstructure is achieved.

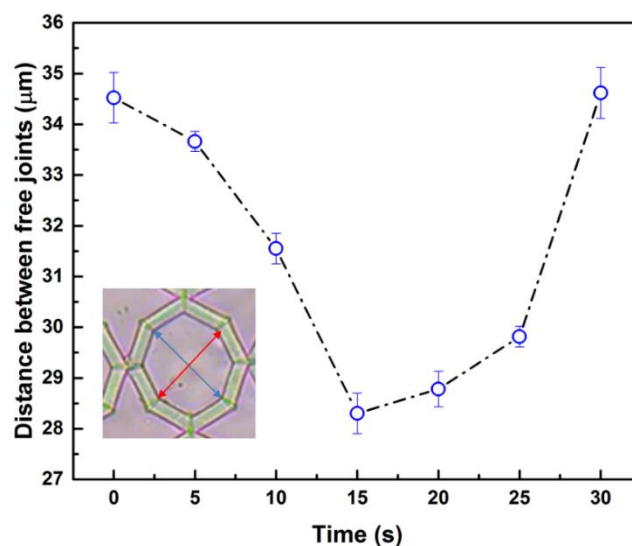


Figure 5.13: Quantitative study of reversible behaviours of ‘octagon to square’ microstructures fabricated by 3D DLW. Distance between free joints as a function of time. Inset figure: illustration of the two directions of distance between free joints.

A quantitative study of the reversible behaviour of the microstructures was performed by measuring the distance between the two free joints shown in Figure 5.13 inset microscope pic. Two different directions (shown in red and blue in Figure 5.13 inset) of measurement of the distance between free joints were obtained to achieve more reliable results in describing the shape change of our fabricated structures. As illustrated in Figure 5.8, the distance between the free joints changes with time. From $t = 0\text{s}$ to $t = 15\text{s}$, when the microstructure is shrinking due to the evaporation of water content, the distance between the free joints in the octagon changes from $34.5\ \mu\text{m}$ to $28.30\ \mu\text{m}$. From $t = 15\text{s}$ to $t = 30\text{s}$ when a drop of water is dropped on our sample, the absorption of water content in hydrogel acts as an external force applied outwards on our fabricated structures, changing the structure from square to octagon. Correspondingly, the distance between the free joints in our measured target changes from $34.5\ \mu\text{m}$, $34.5235\ \mu\text{m}$, $33.663\ \mu\text{m}$, $31.55\ \mu\text{m}$, $28.304\ \mu\text{m}$, $28.7805\ \mu\text{m}$, $29.815\ \mu\text{m}$, and $34.618\ \mu\text{m}$. The deformation rate of our fabricated structure is defined by the largest shape change divided by the original distance, $\Delta d/d=18\%$. As can be seen

from Figure 5.13, our fabricated microstructure exhibits almost 100% reversibility. The measured distance between the free joints recovered to its original value after the whole shape changing cycle.

5.7.5 Characterisation of the swelling behaviour of HMPP + PEGDA hydrogel

To understand the reversibility behaviour of our fabricated structures, it is necessary to study the swelling behaviour of the HMPP + PEGDA hydrogel. The reversibility of the microstructures relies on the water sensitivity of our hydrogel material. This property has been widely studied and utilised in describing drug release from hydrogels.

Traditionally, this property can be described by Fick's law, as set out in Equations (5.1) and (5.2) [195]:

$$J = -D \left(\frac{dc}{dx} \right) \quad (5.1)$$

$$\frac{\partial c}{\partial t} = -D \left(\frac{\partial^2 c}{\partial x^2} \right) \quad (5.2)$$

Assuming a binary system, t , c , J , and D represent time, solution concentration, mass flux and the diffusion mutual differential coefficient, respectively. For our case, the swelling kinetics of the hydrogels follows an even simple model, and the water-stimulated swelling behaviour of our HMPP + PEGDA hydrogel can be explained using Schott's second-order diffusion kinetics, which is written as Equation (5.3):

$$\frac{dM}{dt} = K_s \times (M_\infty - M)^2 \quad (5.3)$$

in which M_∞ , M and K_s are the maximum or equilibrium weight of water uptake, the water uptake at time t , and the kinetic rate of swelling (or shrinking), respectively.

However, it is very difficult to measure the weight change of our microstructures, because of the micrometre scale size. Instead of measuring the weight change of our microstructures, we measured the volume change of our fabricated structures during the shape changing process. Therefore, Equation (5.3) can be transformed into:

$$\frac{dV(t)}{dt} = K_s \times (V_\infty - V(t))^2 \quad (5.4)$$

in which V_∞ , $V(t)$ and K_s are the maximum or equilibrium volume water uptake, the water uptake at time t , and the kinetic rate of swelling or shrinking (negative for swelling and positive for shrinking process).

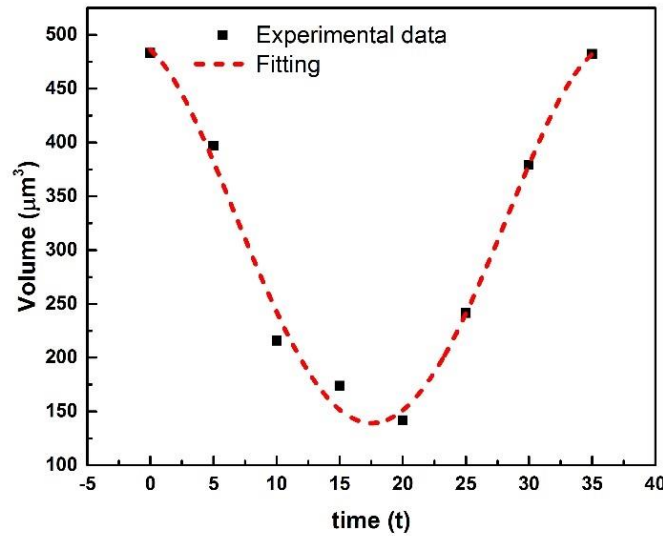


Figure 5.14: Shrinking and swelling behaviour of the PEGDA hydrogel. Volume of the microstructures as a function of time.

As shown in Figure 5.14, the volume change of the microstructure made of PEGDA hydrogel is depicted as a function of time. From $t = 0$ s to $t = 17.5$ s, a shrinking behaviour is observed, and the volume of the microstructure shrinks from $450 \mu m^3$ to $150 \mu m^3$. From $t = 17.5$ s to $t = 35$ s, a swelling behaviour of the microstructure is shown, with a volume change from the minimum $150 \mu m^3$ to maximum $450 \mu m^3$. These behaviours can be fitted into Equation (5.4), shown in the red dotted curve, corresponding to $V_\infty = 483 \mu m^3$, $K_s = 9.2716 \mu m^{-3} s^{-1}$ (close to reported values in related references 196). The swelling ratio of our PEGDA hydrogel is calculated as:

$$\text{Swelling ratio} = (V_t - V_{t_0})/V_0 \times 100 \quad (5.5)$$

Thus, the swelling ratio of our PEGDA hydrogel is around 66%. Compared with bulk PEGDA hydrogels, this value is relatively higher than the common 40%. Several

reasons may give rise to this phenomenon. First, our microstructure has a high or very high surface area to volume ratio compared with bulk materials. Second, our measurement is limited to the x-y plane; shrinkage and swelling behaviour in the z-direction is assumed to be similar to that in x and y. In reference [147], a discussion of the size effect on the swelling ratio of PEGDA hydrogel and the theoretical fitting process is discussed in detail.

5.8 Fabrication of Neuron-inspired Fractal Tree Structures

In this section, we explore the design, fabrication and characterisation of a novel neuron-inspired fractal tree structure in PEGDA hydrogel. Based on the hardness and swelling properties discussed in Section 5.7, neuron-inspired fractal tree structures can be fabricated with controlled laser power and speed.

5.8.1 Design and fabrication of neuron-inspired fractal tree model

A model to emulate the branching structures in BNNs was implemented using home-built MATLAB code. The mathematical model is based on Murray's laws [196]. This fractal tree model shares a lot of similarities of that in BNNs, which has been discussed in Chapter 3. These models permit the description of the geometrical parameters of a neural network (i.e., the length of each branch, its branching order and its branching angle).

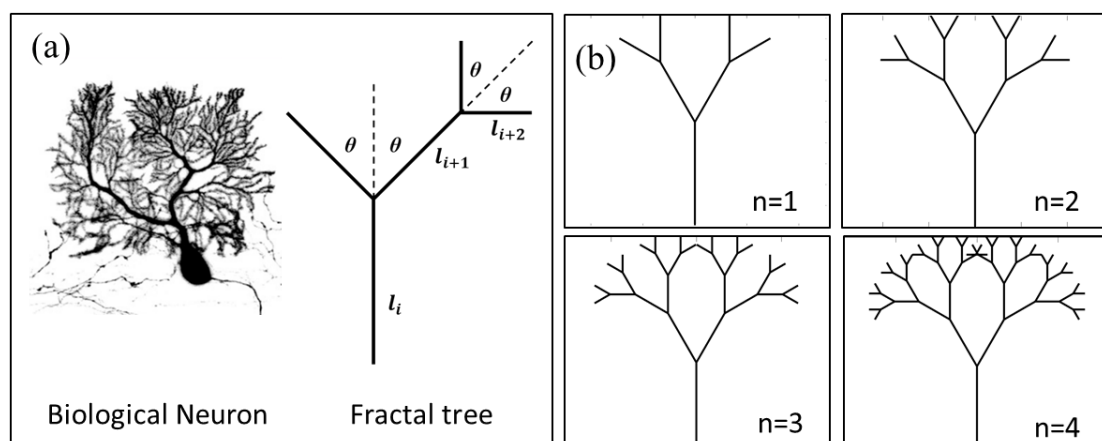


Figure 5.15: Diagrams showing the design of neuron-inspired fractal structures.

Given a branch, as illustrated in Figure 5.15 (a), with original branch l_i and sub branch length l_{i+1} with a branching angle of θ and another sub branch l_{i+2} branching off to the right at angle θ , with respective lengths l_0 , l_1 , and l_2 . Therefore, relations between different branches can be written as it was proposed by Murray [198]: $l_{i+1} = 1/2 l_i$. By increasing the branch or fractal order, different neuron-inspired fractal structures can be generated using MATLAB code based on Murray's equations. The calculated fractal tree structures are shown in Figure 5.15 (b), corresponding to $n = 1$, $n = 2$, $n = 3$ and $n = 4$.

The fabrication path is designed based on the positions calculated using the MATLAB code. To maintain strong bonding between the hydrogel structures and the cover glass, for each line in the fractal structure, we employed a layer-by-layer fabrication path.

5.8.2 Fabrication results

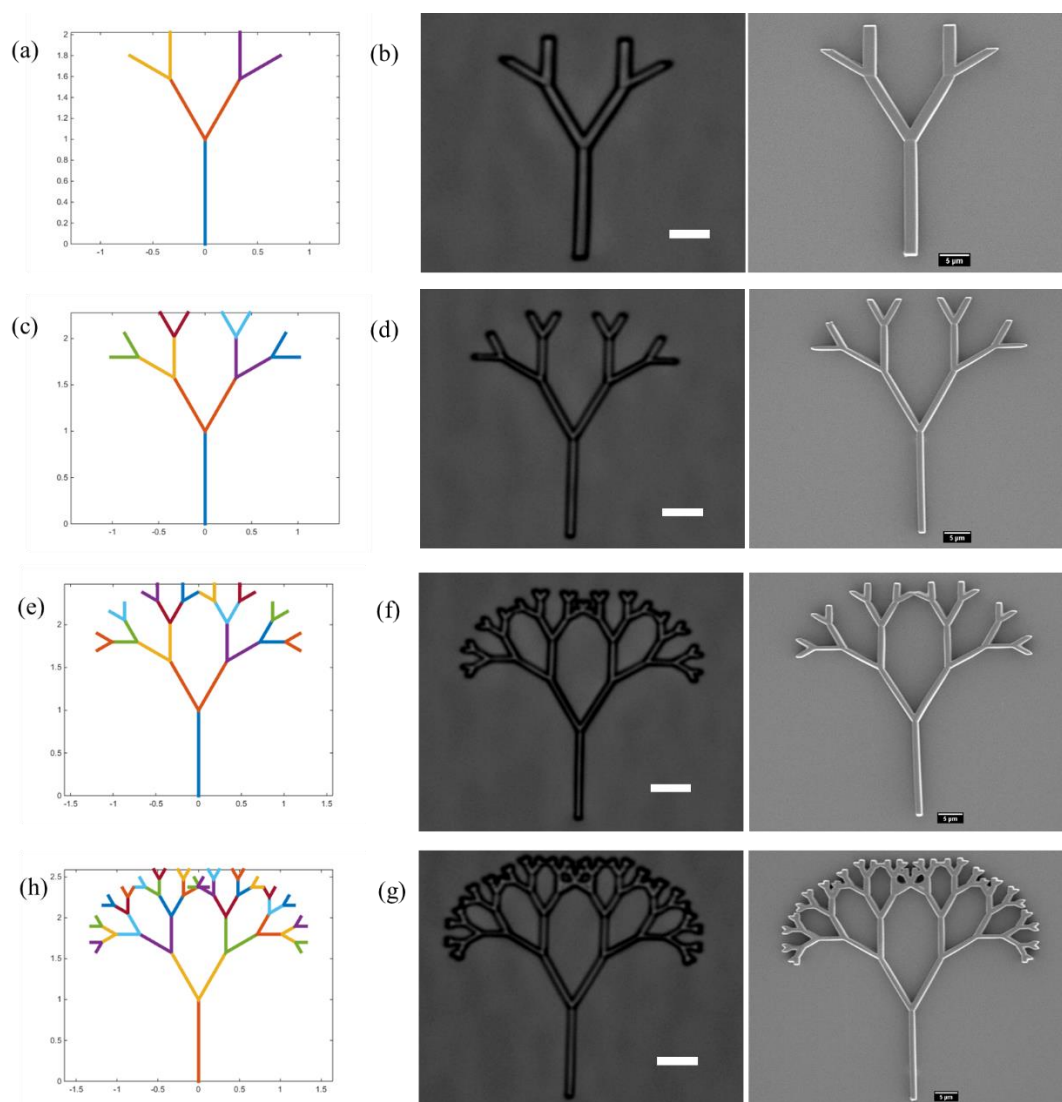


Figure 5.16: Design and fabrication results of neuron-inspired fractal structures. Neuron-inspired fractal structures with different fractal orders. (b), (d), (f), and (g) correspond to the structures designed in (a), (c), (e) and (h). Scale bar is 5 μm .

As shown in Figure 5.16, neuron-inspired fractal tree structures are fabricated in HMPP + PEGDA hydrogel. These fractal tree structures maintained perfect shape compared with the original design at a different fractal order. The smallest feature size of our fabricated structures is 1.5 μm . The images are taken from a transmissive optical microscope and a SEM.

5.9 Conclusion

In summary, this chapter developed and characterised a novel biocompatible material suitable for 3D DLW: HMPP + PEGDA hydrogel. Single-photon absorption spectrum of the photoinitiator HMPP shows an absorption peak at wavelength of 245 nm, and two-photon characterisation of photoinitiator HMPP confirms the TPA cross-section with a value of 4.5 GM.

Second, by scanning the laser threshold power and writing speed, optimal fabrication conditions are confirmed for the HMPP + PEGDA hydrogel. Stable woodpile structures with feature sizes around 1 micrometre were fabricated using our home-built 3D DLW system. The laser power ranged from 1–8 mW, and the writing speed ranged from 1–100 $\mu\text{m/s}$.

In addition, we studied the influence of laser power on the mechanical property (hardness) of the HMPP + PEGDA hydrogel. The hardness of the hydrogel material depends on laser energy dose during the fabrication and ranged from 6–12 MPa.

Based on the unique swelling response behaviour of the HMPP + PEGDA hydrogel, we investigated the design, fabrication and characterisation of reversible ‘octagon to square’ microstructures in hydrogel in Section 5.6. Shrinking and swelling behaviour for a ‘octagon to square’ structure fabricated using 3D DLW showed almost 100% reversibility. In addition, the swelling behaviour of HMPP + PEGDA hydrogel material was around 60% higher than the bulk material. A size effect can explain the difference.

In the last part of this chapter, we demonstrated a novel neuron-inspired fractal tree structure. Our fabricated structures maintained a stable and undeformed shape compared with the design, which may be very useful for future applications in neuron tissue engineering.

In summary, our results in this chapter show that our HMPP + PEGDA hydrogel photopolymerisation system is highly suitable for 3D DLW. The hydrogel performed with a very high photopolymerisation efficiency, corresponding to a wide range of

applicable laser powers and writing speeds. The mechanical property of the hydrogel is highly suitable for applications in tissue engineering.

Chapter 6: Conclusions

6.1 Thesis Conclusions

In this thesis, we theoretically and experimentally investigated the design, fabrication and characterisation of neuron-inspired biomimetic structures for a wide range of applications, such as biomedical engineering and low-density material. Our innovative biomimetic designs are based on the structural features in BNNs, and fabrication was conducted using a home-built 3D DLW system.

This PhD thesis makes several important achievements towards the development of utilising 3D DLW as a fabrication technique in achieving neuron-inspired biomimetic structures with sub-micrometre feature size in 3D space:

1. Two neuron-inspired biomimetic models were introduced based on the principles in biomimetics: a neuron-tracing model and a neuron-inspired Steiner tree structure.
2. Based on 3D DLW, 3D biomimetic structures with different geometries were fabricated.
3. For neuron-tracing structures, we experimentally demonstrated fabrication of 3D biomimetic neuron structures at scales of the sub-micrometre and tenfold smaller than biological counterparts.
4. For neuron-inspired Steiner tree structures, we experimentally characterised fluorescent behaviours of 3D biomimetic structures.

5. We introduced a novel biocompatible hydrogel material suitable for 3D DLW, and theoretically and experimentally characterised the influence of fabrication conditions on the properties of the hydrogel, such as Young's modulus and swelling behaviours.

In this thesis, we investigated a range of 3D neuron-inspired biomimetic structures based on the structural features of BNNs.

In Chapter 3, we demonstrated the fabrication of biomimetic neuron structures using 3D DLW. The influences of laser power and writing speed in fabricating biomimetic neuron structures with varied topologies were studied. The quantitative experiment results revealed that neuron structures with different average branch angles require different fabrication conditions. Based on this, in this work, the first experimental realisation of a micrometre-scale biomimetic neuron structure 10 times smaller than biological neurons has been achieved using two-photon DLW. Combining galvo-scanning devices, long-range translational stages and nano-translation stages can provide a potential method to replicate the topological features of BNNs to a larger scale and forms a new optical technology platform for applications using 3D DLW in engineered neural networks.

In Chapter 4, we explored the design, fabrication and characterisation of the mechanical properties of neuron-inspired Steiner tree structures fabricated by 3D DLW. Compared with traditional lattice structures, which are inspired by the minimal surface in nature, neuron-inspired Steiner structures are designed with the principle of shortest connection distance and have the lowest relative density among the four traditional lattice structures.

The major challenges we faced during the fabrication of the Steiner tree structures using 3D DLW were how to fabricate stable microstructures with smaller feature size and how to achieve a circular-shaped beam cross-section in the microstructures? By introducing a galvo-dithering DLW system based on previous work, stable Steiner tree structures with the smallest feature size of 200 nm were fabricated with a circular-shaped beam cross-section. The relative densities of our fabricated Steiner

tree structures range from 5–15% of the bulk material. The experimental results and simulation results showed that Steiner tree structures possess tuneable mechanical properties that are in the range of biological neuron tissue and are promising for future applications in neuron tissue engineering. In addition, the ultralow-density features of the microstructures fabricated by galvo-dithering DLW provide a novel design for ultralow-density materials, which have great potential in applications such as biomedical engineering, filters and energy storage.

In Chapter 5, we developed and characterised a novel biocompatible material suitable for 3D DLW: HMPP + PEGDA hydrogel. The single-photon absorption spectrum of the photoinitiator HMPP shows an absorption peak at the wavelength of 245 nm, and two-photon characterisation of the photoinitiator HMPP confirms a TPA cross-section of 4.5 GM. Second, optimal fabrication conditions are confirmed for PEGDA hydrogel by scanning the laser threshold power and writing speed. The laser power ranges from 1–8 mW and the writing speed ranges from 1–100 $\mu\text{m/s}$. Stable woodpile structures with feature sizes around 1 micrometre were fabricated using our home-built 3D DLW system. In addition, the Young's modulus of the hydrogel material depends on the laser energy dose during fabrication.

Based on the unique swelling response behaviour of PEGDA hydrogel, we investigated the design, fabrication and characterisation of reversible 'octagon to square' microstructures in hydrogel in Section 5.6. Shrinking and swelling behaviour in 'octagon to square' structures fabricated using 3D DLW showed almost 100% reversibility. In addition, the swelling behaviour of PEGDA hydrogel material is around 60%, higher than the bulk material. A size effect can be used to explain the difference. In the last part of this chapter, we demonstrated a novel neuron-inspired fractal tree structure, such that our fabricated structures maintained stable and undeformed shapes compared with the design, which should prove very useful for future applications in neuron tissue engineering. In summary, our results in this chapter show that our HMPP + PEGDA hydrogel photopolymerisation system is very suitable for 3D DLW. The hydrogel performed with a very high photopolymerisation efficiency, corresponding to a wide range of applicable laser powers and writing

speeds. The mechanical property of the hydrogel is highly suitable for applications in tissue engineering.

To conclude, this PhD thesis focused on the design, fabrication and characterisation of neuron-inspired biomimetic structures using 3D DLW. In particular, we studied and examined the stability and mechanical properties of these neuron-inspired microstructures fabricated by 3D DLW. The fabrication conditions involved during the fabrication process pose great influences on the stability and mechanical properties of these neuron-inspired biomimetic structures. We carefully studied the influence of laser power and writing speed on mechanical properties, such as elastic-capillary force behaviours in Chapter 3, the power-scaling law of Young's modulus in Chapter 4 and the swelling behaviour of hydrogel in Chapter 5. The knowledge generated in this PhD thesis is of great potential in many applications in biomimetics, low-density material and biomedical engineering.

6.2 Future Outlook

In this section, we discuss the future outlook of this research and propose possible research projects based on the results of this PhD thesis in three areas.

6.2.1 Three-dimensional direct laser writing for large-scale fabrication of neuron-inspired structures

Regarding the biomimetic neuron structures fabricated using single-beam two-photon DLW we introduced in Chapter 3, creation of biomimetic neuronal structures that emulate the structural features in BNNs at the micrometre scale would be of great benefit in areas of research such as engineered neural networks.

However, large-scale biomimetic neuronal structures cannot be easily achieved using 3D DLW because of the structural complexity of BNNs. This challenge can be articulated in two aspects:

1. Unachievable fabrication time. BNNs are 3D networks structures spanning at a very large scale; in the human brain, for example, the total neuron circuit length is

estimated to be 100 billion μm , resulting in a fabrication time of 1 billion seconds (roughly 31.7 years).

2. Structural data on neuronal circuits at synaptic resolution are rarely available from neuroscience.

One solution to achieve large-scale biomimetic neuronal structures is the utilisation of ‘multifocal arrays’ in 3D DLW. It has been demonstrated that large-area fabrication using fast and parallel laser processing can be obtained via multifocal array generation [85]. The vectorial Debye-based 2D or 3D Fourier-transforms can generate phase-modulated diffraction-limited volumetric multifocal arrays with diminished cross-talk, resulting in high uniformity [96]. Even though the concept generated a single structure using a multifocal array, the technique has potential to generate an array of 2D or 3D structures. Therefore, it is possible to effectively utilise this ability for the generation of an array of biomimetic neuron structures in series or parallel for large areas, which could be very useful in scaffold design in biomedical engineering.

Another solution lies in the recent use of deep-learning algorithms to aid fabrication path design in 3D DLW. First, deep learning has been a very hot research topic because of its capability in solving challenges arising from large amounts of data, such as those related to path design, population control and the economy. Similarly, the structural data of neuron networks can be regarded as a huge database, consisting of billions of positions connected with each other through a 3D network.

Therefore, we proposed a project named “Deep-learning-aided three-dimensional direct laser writing of the complete connectome of mushroom body from an insect brain” (journal publication 4) as a possible solution to solve the technique challenges in fabrication of large-scale biomimetic neuronal structures.

Future work should focus on the replication of a 3D biomimetic mushroom body from an insect brain with sub-micrometre feature size using 3D DLW aided by a deep-learning algorithm. The first complete connectome of a mushroom body in *Drosophila* was achieved in 2017 [136]. A mushroom body is a higher-order parallel neuronal circuit in many invertebrate brains and has proved essential for associative learning

and cognitive processing in adult insects. A deep-learning algorithm [142] for fabrication path optimisation is introduced to assist our laser fabrication to find the shortest fabrication time. This work provides a potential method to replicate the structural features of BNNs at a larger scale and opens a new avenue for higher-level understanding of the structure–function relationship in engineered neural networks.

6.2.2 Enhancing the mechanical properties of Steiner tree microstructures at the ultralow-density scale

The Steiner tree structures introduced in Chapter 4 were shown to possess the lowest relative density from the geometrical design due to the shortest connection distance in the unit. However, in Section 4.3, the fabrication of Steiner tree structures using single-beam two-photon DLW could not achieve ultralow-density microstructures with strong mechanical properties, such as Young’s modulus. The smallest fabrication feature size available in single-beam two-photon DLW is limited to around 150 nm in our fabrication system. While it is possible to reduce the fabrication feature size and relative density by decreasing the energy dose in laser writing, this would dramatically decrease the mechanical strength of the microstructures. Two solutions may help to enhance the mechanical properties of the Steiner tree structures at the ultralow-density scale (see Figure 6.1).

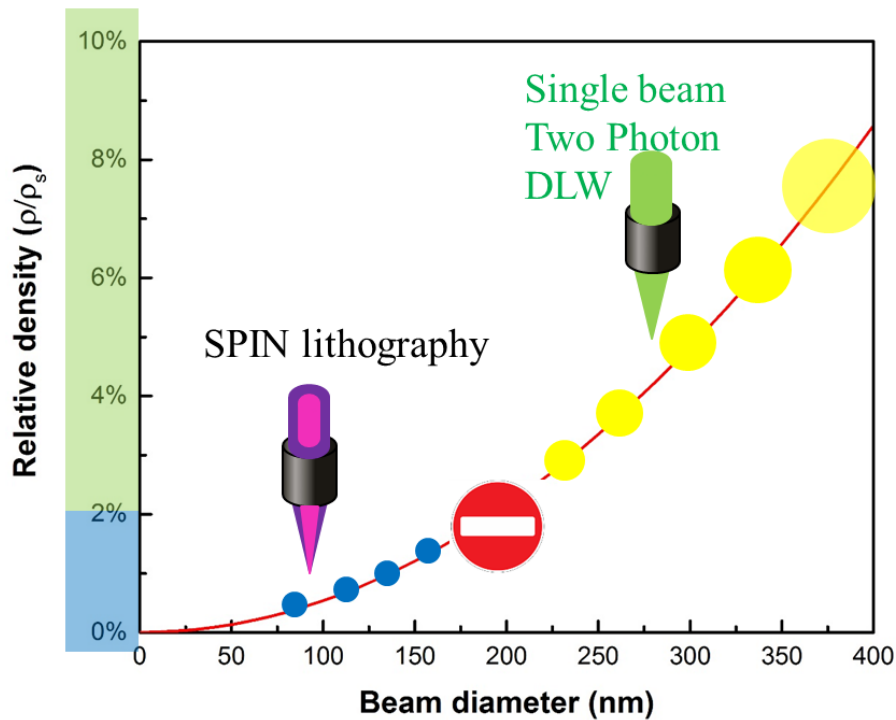


Figure 6.1: Illustration to fabricate Steiner tree structures with ultralow-density using SPIN lithography.

One solution is the recent development of two-beam SPIN lithography [197]. As discussed in Section 2.6, two-beam SPIN lithography achieves super-resolution feature sizes by tuning the shape of both the induction and inhibition beam during the focusing, and also by tuning the power of the induction and inhibition beams. The relationship between the fabrication feature size (linewidth) and the inhibition laser power can be explained via the formula,

$$\text{line width (nm)} = \frac{\alpha}{\sqrt{1 + \beta \times I_{\text{inhibition}}^4 / I_s}} \quad (6.1)$$

This formula has been proved using a photoinitiator BDCC, along with a photoinhibitor TED in a published work in 2013 [198], where a 3D optical beam lithography with 9 nm feature size and 52 nm two-line resolution in a newly developed TPA resin with high mechanical strength was achieved (see Figure 2.10).

6.2.3 Developing a hydrogel material for two-beam super-resolution direct laser writing

The utilisation of single-beam two-photon DLW enabled the fabrication of 3D microstructures with adequate or controllable characteristics to mimic *in vivo* extracellular matrix (ECM) properties (e.g., stiffness, porosity and degradability), and has emerged as a promising method in tissue engineering. However, the fabrication resolution in hydrogel materials is still limited to hundreds of nanometres in single-beam two-photon DLW. Development of a novel material as a photoinhibitor in hydrogel would be of great importance for future development of hydrogel in laser fabrication.

6.3 Summary

In summary, progressive integration of material science, biomimetics, biomedical engineering, mechanical engineering and 3D DLW techniques based on photopolymerisation has enabled the creation of 3D biomimetic microstructures for specific applications. It is critical to mention that 3D DLW is still in its early stages of application, and there is a huge number of challenges that need to be addressed. However, from the perspective of using 3D DLW to further development in neuron-related research, such as neuron-tissue engineering and neuron computing interfaces, 3D DLW is the best option compared with other fabrication methods. More research should be focused on the application of 3D DLW in these fields.

Appendix A: Synthesis of the Zirconium-based Organic–inorganic Photoresist

In this project, a zirconium-containing organic–inorganic photosensitive material doped with tertiary amine metal-binding moieties was chosen as the material for the fabrication of 3D neuron-inspired structures because of its good performance in 3D DLW [30]. Preparation, modification and processing are straightforward and, in combination with their high optical quality, post-processing chemical and electrochemical inertness, and good mechanical and chemical stability, they have found several applications in photonics and biomedical devices when structured by DLW.

Monomers in the photoresist of our project are methacryloxypropyl trimethoxysilane (MAPTMS) and 2-(dimethylamino) ethyl methacrylate (DMAEMA); 4, 4-bis(diethylamino)benzophenone (BIS) was used as the photoinitiator and zirconium propoxide (ZPO, 70% in propanol) and the alkoxy silane groups of MAPTMS served as inorganic forming moieties. Each component can be obtained from Sigma-Aldrich and does not need further purification.

Synthesis of the photoresist is as follows:

1. Mix 4.96 mL diluted water into 39 μ L HCl to achieve a solution of HCL with 0.1mol/L molecule density.
2. Mix the HCl solution with 13.03 mL MPTMS and stir at a speed of 500/300 for 5 minutes.
3. Mix 3.8 mL DMAEMA with 9.96 mL ZPO and stir at a speed of 500 for 15 minutes.
4. Mix solution 3 with solution 2 and stir for 15 minutes.
5. Finally, mix 1.89 mL diluted water in solution 4 and stir for 15 minutes.

Appendix B: Mechanical Characterisation of Zirconium-based Photoresist

To study the mechanical property of the organic–inorganic photoresist, the Young’s modulus of the 3D polymer microstructures was measured by an AFM. Combined with the characteristics of the layer-by-layer process of TPP microfabrication and the real condition of AFM measurement, cubic microstructures with $10 \times 10 \times 10 \mu\text{m}^3$ (length \times width \times height) at various laser powers and writing speeds were fabricated using a layer-by-layer writing process. As an example, SEM images of the 3D cubic microstructures fabricated with laser power of 1 mW and writing speed of $50 \mu\text{m/s}$ are shown in Figure B.1 (a2) and (a3).

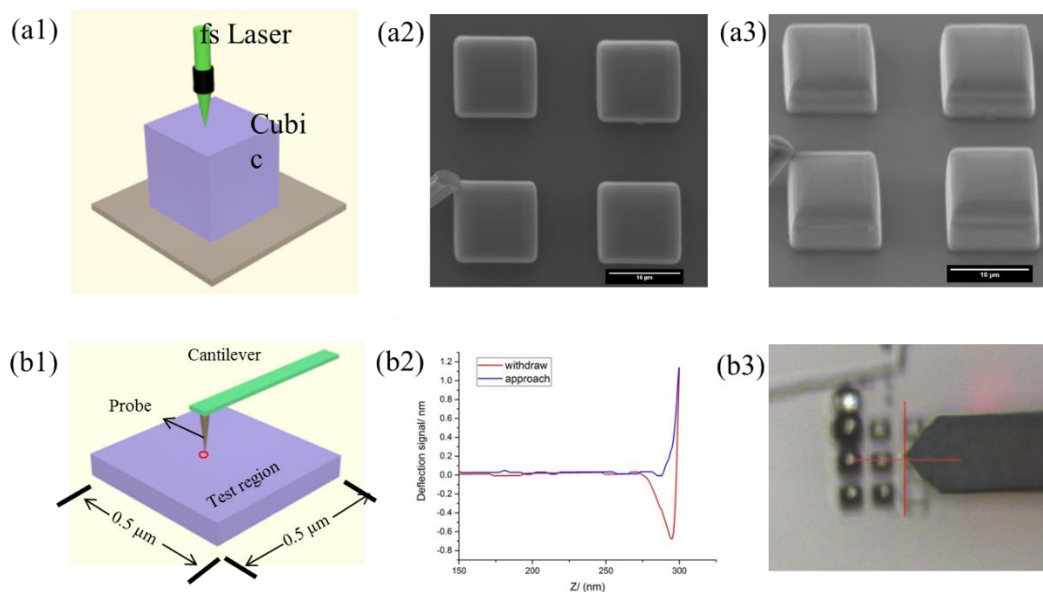


Figure B.1: Illustration of fabrication and measurement of the Young’s modulus of the photoresist. (a1), (a2) and (a3) are fabrication of micro-sized cubic structures using 3D DLW using a SEM. (b1), (b2) and (b3) are the measurement of the modulus of microstructures using an AFM. Correspondingly, (b2) is an example of the deflection signal as a function of distance during the measurement. (b3) is the real-time image of the measurement under the built-in microscope of the AFM.

To investigate the polymer’s ability to resist deformation during microfabrication, the Young’s modulus of the microstructures in air was studied. Laser power and writing speed are two important parameters for microstructure fabrication; the crosslink

density of 3D microstructures can be changed by adjusting the laser power or writing speed. First, to study the influence of laser power on the Young's modulus of organic–inorganic photoresist, cubic microstructures were fabricated with laser power ranging from 0.25–2.0 mW, and writing speed of 50 $\mu\text{m/s}$. The schematic diagram of the Young's modulus measurement is shown in Figure B.1 The AFM images of height and modulus of cubic microstructures fabricated with laser power of 1.0 mW in the test region are shown in Figure B.2 (a1) and (a2).

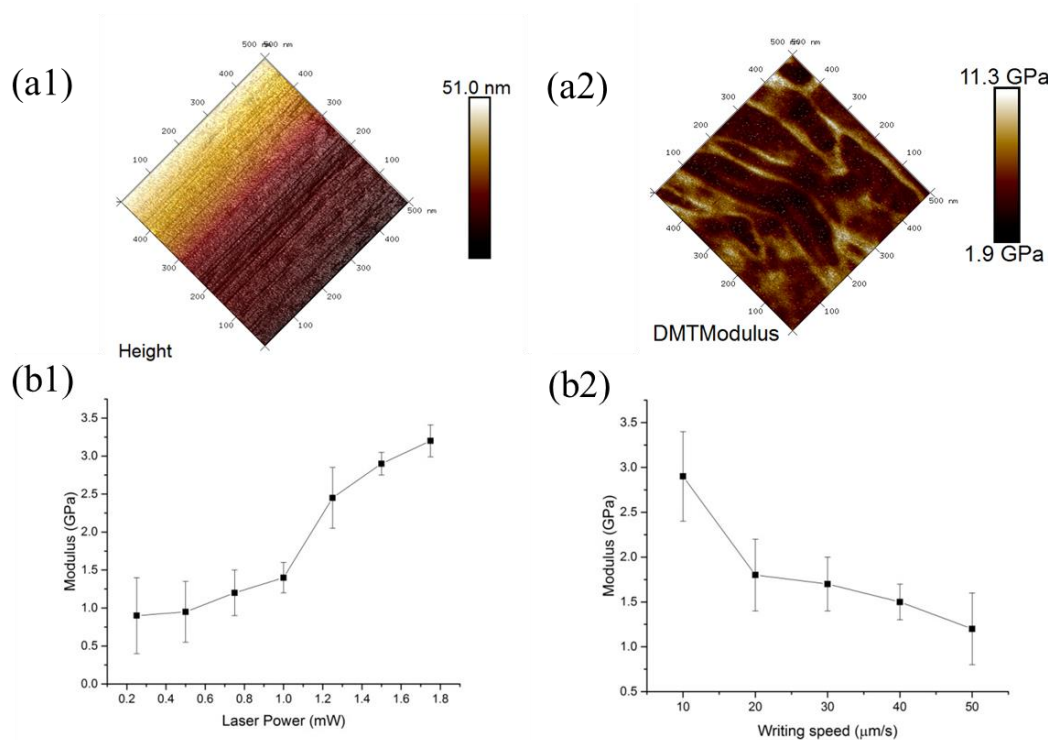


Figure B.2: The influence of laser parameters on the Young's modulus of the organic–inorganic photoresists in air. (a1) and (a2) AFM images of height and modulus of cubic microstructures fabricated with laser power of 1.0 mW in the test region. (b1) Modulus of the polymer as a function of laser power. (b2) Modulus of the polymer as a function of writing speed.

The Young's modulus of our photoresist ranges from 1–3.5 GPa, which shows that our zirconium-based photoresist is very strong. Therefore, in our theoretical calculation in Chapters 3 and 4, we chose a Young's modulus of 2 GPa for the material.

Appendix C: Properties of Low-density 3D Microstructures

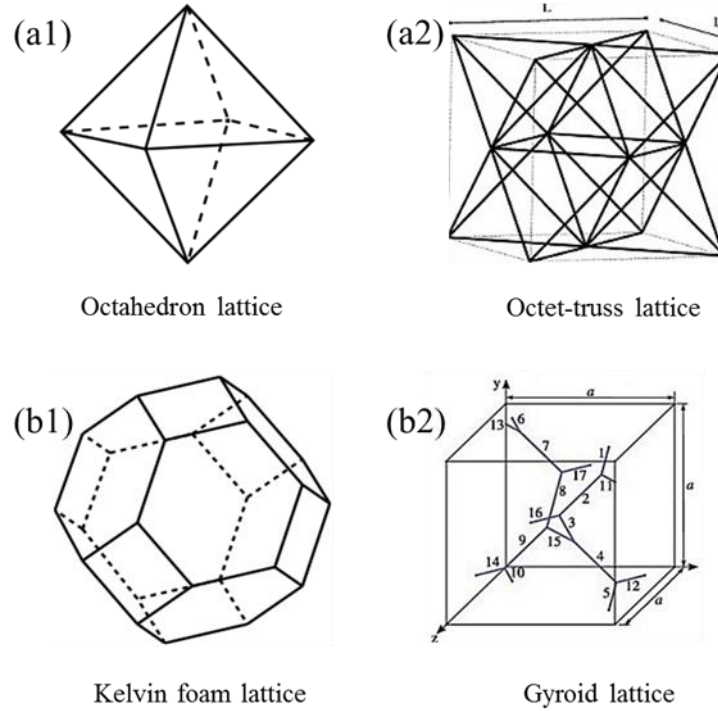


Figure C.1: Four typical low-density lattice structures. (a1) Octahedron lattice. (a2) Octet-truss lattice. (b1) Kelvin foam lattice. (b2) Gyroid lattice.

There are four kinds of architecture structures that have been widely studied in low-density lattice structures (see Figure C.1). Among these four different lattice structures, octahedron and octet-truss lattice structures are generally categorised as bending-dominated, while the Kelvin foam lattice and gyroid lattice structures are defined as stretching-dominated. The mechanical properties of these lattice structures rely on the relative density of the fabricated structures. As discussed in Section 4.5.1, the Young's modulus and yield strength of the lattice structures follow a power-scaling law with relative density:

$$E \sim B \times E_s \times \bar{\rho}^m \quad (4.3)$$

$$\sigma_s \sim C \times \sigma_{ys} \times \bar{\rho}^n \quad (4.4)$$

in which E_s and σ_{ys} are the Young's modulus and yield strength of the constituent material, and the exponents m and n are defined by the cell geometry. B and C are proportionality coefficients also defined by the cell geometry. Here, we summarise the experimental results of these four lattice structures from the literature [199]. Even though the results are sometimes not in agreement, there is some general understanding of the mechanical properties of the structures. Steiner tree lattice structure is also showed in this table.

Table C.1: Summary of the scaling constant (m and n) and proportionality constants (B and C) of the Young's modulus and the yield strength scaling relationships respectively for each lattice structure made of polymers.

Rigidity	Lattice	B	m	C	n
Rigid	Octahedron	0.57	1.1	1.59	1.92
Rigid	Octet-truss	0.82	1.77	1.31	1.88
Nonrigid	Kelvin foam	0.57	2.0	0.84	1.63
Nonrigid	Gyroid	0.32	2.0	0.315	1.5
Nonrigid	Steiner tree	0.15	2.08	5.86	2.39

As seen in Table C.1, lattice structures with different topologies have different exponents in the power-scaling law with relative density. Steiner tree structures show a similar scaling behaviour as Kelvin foam, which proves that Steiner tree structures are dominated by the bending of the beams in terms of the scaling constants and proportionality constants.

We also summarised the mathematical formulas of different lattice structures, shown in Table C.1. Compared with the other four lattice structures (octahedron, octet-truss, Kelvin foam and gyroid), Steiner tree lattice structures have the smallest relative density given the same unit size W and beam diameter t .

Table C.2: Summary of the mathematical formulas of relative densities of different lattice structures.

Lattice type	Relative density (ρ/ρ_s)
8 points Steiner tree lattice	$\left(\frac{3\sqrt{3} + 1}{4}\right)\pi \times \frac{t^2}{W^2}$
Octahedron lattice	$3\sqrt{2}\pi \times \frac{t^2}{W^2}$
Octet-truss lattice	$3\sqrt{2}\pi \times \frac{t^2}{W^2}$
Kelvin foam lattice	$6(\sqrt{2} - 1)\pi \times \frac{t^2}{W^2}$
Gyroid lattice	$\frac{3\sqrt{2}}{2}\pi \times \frac{t^2}{W^2}$

References

- [1] <https://www.braininitiative.org/>
- [2] <https://www.humanbrainproject.eu/en/>
- [3] <https://brainminds.jp/en/>
- [4] Poo, M. M., Du, J. L., Ip, N. Y., Xiong, Z. Q., Xu, B., & Tan, T. (2016). China brain project: basic neuroscience, brain diseases, and brain-inspired computing. *Neuron*, 92(3), 591-596.
- [5] <https://www.brainalliance.org.au/>
- [6] Aebbersold, M. J., Dermutz, H., Forro, C., Weydert, S., Thompson-Steckel, G., Vörös, J., & Demko, L. (2016). “Brains on a chip”: Towards engineered neural networks. *TrAC Trends in Analytical Chemistry*, 78, 60-69.
- [7] Berdichevsky, Y., Staley, K. J., & Yarmush, M. L. (2010). Building and manipulating neural pathways with microfluidics. *Lab on a Chip*, 10(8), 999-1004.
- [8] Roth, S., Bisbal, M., Brocard, J., Bugnicourt, G., Saoudi, Y., Andrieux, A., ... & Villard, C. (2012). How morphological constraints affect axonal polarity in mouse neurons. *PloS one*, 7(3), e33623.
- [9] D. Kleinfeld, K. H. Kahler, and P. E. Hockberger, “Controlled outgrowth of dissociated neurons on patterned substrates,” *J. Neurosci.* 8(11), 4098-4120 (1988).
- [10] H. Dermutz, R. R. Grüter, A. M. Truong, L. Demkó, J. Vörös, and T. Zambelli, “Local polymer replacement for neuron patterning and in situ neurite guidance,” *Langmuir* 30(23), 7037-7046 (2014).

-
- [11] Yi, Y., Park, J., Lim, J., Lee, C. J., & Lee, S. H. (2015). Central nervous system and its disease models on a chip. *Trends in biotechnology*, 33(12), 762-776.
- [12] D'avanzo, C., Aronson, J., Kim, Y. H., Choi, S. H., Tanzi, R. E., & Kim, D. Y. (2015). Alzheimer's in 3D culture: challenges and perspectives. *Bioessays*, 37(10), 1139-1148.
- [13] Hasan, M., & Berdichevsky, Y. (2016). Neural circuits on a chip. *Micromachines*, 7(9), 157.
- [14] Fromherz, P. (2006). Three levels of neuroelectronic interfacing: silicon chips with ion channels, nerve cells, and brain tissue. *Annals of the New York Academy of Sciences*, 1093(1), 143-160.
- [15] Fromherz, P. (2008). Physical problems of brain-computer interfacing. In *Contemporary Physics* (pp. 71-85).
- [16] McDougal, R. A., & Shepherd, G. M. (2015). 3D-printer visualization of neuron models. *Frontiers in neuroinformatics*, 9, 18.
- [17] Norman, J. J., & Desai, T. A. (2006). Methods for fabrication of nanoscale topography for tissue engineering scaffolds. *Annals of biomedical engineering*, 34(1), 89-101.
- [18] Tang-Schomer, M. D., White, J. D., Tien, L. W., Schmitt, L. I., Valentin, T. M., Graziano, D. J., ... & Kaplan, D. L. (2014). Bioengineered functional brain-like cortical tissue. *Proceedings of the National Academy of Sciences*, 111(38), 13811-13816.
- [19] Hribar, K. C., Soman, P., Warner, J., Chung, P., & Chen, S. (2014). Light-assisted direct-write of 3D functional biomaterials. *Lab on a chip*, 14(2), 268-275.
- [20] Zhu, W., Ma, X., Gou, M., Mei, D., Zhang, K., & Chen, S. (2016). 3D printing of functional biomaterials for tissue engineering. *Current opinion in biotechnology*, 40, 103-112.

- [21] Sporns, O., Tononi, G., & Kötter, R. (2005). The human connectome: a structural description of the human brain. *PLoS computational biology*, 1(4), e42.
- [22] Gill, A. A., Ortega, Í., Kelly, S., & Claeysens, F. (2015). Towards the fabrication of artificial 3D microdevices for neural cell networks. *Biomedical microdevices*, 17(2), 27.
- [23] Boyd, R. W. (2003). *Nonlinear optics*. Elsevier.
- [24] LaFratta, C. N., Fourkas, J. T., Baldacchini, T., & Farrer, R. A. (2007). Multiphoton fabrication. *Angewandte Chemie International Edition*, 46(33), 6238-6258.
- [25] Anscombe, N. (2010). *Direct laser writing*.
- [26] Li, L., & Fourkas, J. T. (2007). Multiphoton polymerization. *Materials Today*, 10(6), 30-37.
- [27] Maruo, S., Nakamura, O., & Kawata, S. (1997). Three-dimensional microfabrication with two-photon-absorbed photopolymerization. *Optics letters*, 22(2), 132-134.
- [28] Goi, E., Mashford, B. S., Cumming, B. P., & Gu, M. (2016). Tuning the Refractive Index in Gyroid Photonic Crystals via Lead-Chalcogenide Nanocrystal Coating. *Advanced Optical Materials*, 4(2), 226-230.
- [29] Melissinaki, V., Gill, A. A., Ortega, I., Vamvakaki, M., Ranella, A., Haycock, J. W., ... & Claeysens, F. (2011). Direct laser writing of 3D scaffolds for neural tissue engineering applications. *Biofabrication*, 3(4), 045005.
- [30] Thekkekara, L. V., Jia, B., Zhang, Y., Qiu, L., Li, D., & Gu, M. (2015). On-chip energy storage integrated with solar cells using a laser scribed graphene oxide film. *Applied Physics Letters*, 107(3), 031105.
- [31] Gu, M., Li, X., & Cao, Y. (2014). Optical storage arrays: a perspective for future big data storage. *Light: Science & Applications*, 3(5), e177.
- [32] Sun, H. B., Matsuo, S., & Misawa, H. (1999). Three-dimensional photonic crystal structures achieved with two-photon-absorption photopolymerization of resin. *Applied physics letters*, 74(6), 786-788.

- [33] Ovsianikov, A., Viertl, J., Chichkov, B., Oubaha, M., MacCraith, B., Sakellari, I., ... & Fotakis, C. (2008). Ultra-low shrinkage hybrid photosensitive material for two-photon polymerization microfabrication. *Acs Nano*, 2(11), 2257-2262.
- [34] Li, J., Jia, B., Zhou, G., & Gu, M. (2006). Fabrication of three-dimensional woodpile photonic crystals in a PbSe quantum dot composite material. *Optics express*, 14(22), 10740-10745.
- [35] Melissinaki, V., Gill, A. A., Ortega, I., Vamvakaki, M., Ranella, A., Haycock, J. W., ... & Claeysens, F. (2011). Direct laser writing of 3D scaffolds for neural tissue engineering applications. *Biofabrication*, 3(4), 045005.
- [36] Gou, X., Zheng, M., Zhao, Y., Dong, X., Jin, F., Xing, J., & Duan, X. (2017). Mechanical property of PEG hydrogel and the 3D red blood cell microstructures fabricated by two-photon polymerization. *Applied Surface Science*, 416, 273-280.
- [37] Hu, Y., Lao, Z., Cumming, B. P., Wu, D., Li, J., Liang, H., ... & Gu, M. (2015). Laser printing hierarchical structures with the aid of controlled capillary-driven self-assembly. *Proceedings of the National Academy of Sciences*, 112(22), 6876-6881.
- [38] Panchuk, N. (2006). An exploration into biomimicry and its application in digital & parametric [architectural] design (Master's thesis, University of Waterloo).
- [39] Rah, J. C., Feng, L., Druckmann, S., Lee, H., & Kim, J. (2015). From a meso- to micro-scale connectome: array tomography and mGRASP. *Frontiers in neuroanatomy*, 9, 78.
- [40] Roman, B., & Bico, J. (2010). Elasto-capillarity: deforming an elastic structure with a liquid droplet. *Journal of Physics: Condensed Matter*, 22(49), 493101.
- [41] Meza, L. R. (2016). Design, Fabrication, and Mechanical Property Analysis of 3D Nanoarchitected Materials (Doctoral dissertation, California Institute of Technology).

- [42] Ashby, M. F. (2005). The properties of foams and lattices. *Philosophical Transactions of the Royal Society A: Mathematical, Physical and Engineering Sciences*, 364(1838), 15-30.
- [43] Koch, C., & Segev, I. (2000). The role of single neurons in information processing. *Nature neuroscience*, 3(11s), 1171.
- [44] <https://www.nobelprize.org/prizes/medicine/1906/cajal/biographical/>
- [45] Chklovskii, D. B. (2004). Synaptic connectivity and neuronal morphology: two sides of the same coin. *Neuron*, 43(5), 609-617.
- [46] Murre, J. M. J., & Sturdy, D. P. (1995). The connectivity of the brain: multi-level quantitative analysis. *Biological cybernetics*, 73(6), 529-545.
- [47] Vogt, A. K., Wrobel, G., Meyer, W., Knoll, W., & Offenhäusser, A. (2005). Synaptic plasticity in micropatterned neuronal networks. *Biomaterials*, 26(15), 2549-2557.
- [48] Jungblut, M., Knoll, W., Thielemann, C., & Pottek, M. (2009). Triangular neuronal networks on microelectrode arrays: an approach to improve the properties of low-density networks for extracellular recording. *Biomedical microdevices*, 11(6), 1269.
- [49] Corey, J. M., Wheeler, B. C., & Brewer, G. J. (1991). Compliance of hippocampal neurons to patterned substrate networks. *Journal of neuroscience research*, 30(2), 300-307.
- [50] Taylor, A. M., Blurton-Jones, M., Rhee, S. W., Cribbs, D. H., Cotman, C. W., & Jeon, N. L. (2005). A microfluidic culture platform for CNS axonal injury, regeneration and transport. *Nature methods*, 2(8), 599.
- [51] S. Yoshida, T. Teshima, K. Kuribayashi-Shigetomi, S. Takeuchi, Single neural cells on mobile micro plates for precise neural network assembly, *Proc. 15th Int. Conf. Miniaturized Syst. Chem. Life Sci.* 1 (2011) 1749–1751. F
- [52] Onoe, H., & Takeuchi, S. (2008). Microfabricated mobile microplates for handling single adherent cells. *Journal of Micromechanics and Microengineering*, 18(9), 095003.

- [53] Merz, M., & Fromherz, P. (2005). Silicon chip interfaced with a geometrically defined net of snail neurons. *Advanced Functional Materials*, 15(5), 739-744.
- [54] Li, W., Xu, Z., Huang, J., Lin, X., Luo, R., Chen, C. H., & Shi, P. (2014). NeuroArray: a universal interface for patterning and interrogating neural circuitry with single cell resolution. *Scientific reports*, 4, 4784.
- [55] Yamada, A., Vignes, M., Bureau, C., Mamane, A., Venzac, B., Descroix, S., ... & Malaquin, L. (2016). In-mold patterning and actionable axo-somatic compartmentalization for on-chip neuron culture. *Lab on a Chip*, 16(11), 2059-2068.
- [56] Yanagawa, F., Sugiura, S., & Kanamori, T. (2016). Hydrogel microfabrication technology toward three dimensional tissue engineering. *Regenerative Therapy*, 3, 45-57.
- [57] Forró, C., Thompson-Steckel, G., Weaver, S., Weydert, S., Ihle, S., Dermutz, H., ... & Vörös, J. (2018). Modular microstructure design to build neuronal networks of defined functional connectivity. *Biosensors and Bioelectronics*, 122, 75-87.
- [58] Tang-Schomer, M. D., White, J. D., Tien, L. W., Schmitt, L. I., Valentin, T. M., Graziano, D. J., ... & Kaplan, D. L. (2014). Bioengineered functional brain-like cortical tissue. *Proceedings of the National Academy of Sciences*, 111(38), 13811-13816.
- [59] Lozano, R., Stevens, L., Thompson, B. C., Gilmore, K. J., Gorkin III, R., Stewart, E. M., ... & Wallace, G. G. (2015). 3D printing of layered brain-like structures using peptide modified gellan gum substrates. *Biomaterials*, 67, 264-273.
- [60] Gill, A. A., Ortega, Í., Kelly, S., & Claeysens, F. (2015). Towards the fabrication of artificial 3D microdevices for neural cell networks. *Biomedical microdevices*, 17(2), 27.
- [61] Millet, L. J., & Gillette, M. U. (2012). New perspectives on neuronal development via microfluidic environments. *Trends in Neurosciences*, 35(12), 752-761.

- [62] Hardelauf, H., Sisnaiske, J., Taghipour-Anvari, A. A., Jacob, P., Drabiniok, E., Marggraf, U., ... & West, J. (2011). High fidelity neuronal networks formed by plasma masking with a bilayer membrane: analysis of neurodegenerative and neuroprotective processes. *Lab on a Chip*, 11(16), 2763-2771.
- [63] Taylor, A. M., Blurton-Jones, M., Rhee, S. W., Cribbs, D. H., Cotman, C. W., & Jeon, N. L. (2005). A microfluidic culture platform for CNS axonal injury, regeneration and transport. *Nature methods*, 2(8), 599.
- [64] Takayama, Y., Kotake, N., Haga, T., Suzuki, T., & Mabuchi, K. (2012). Formation of one-way-structured cultured neuronal networks in microfluidic devices combining with micropatterning techniques. *Journal of bioscience and bioengineering*, 114(1), 92-95.
- [65] Merz, M., & Fromherz, P. (2005). Silicon chip interfaced with a geometrically defined net of snail neurons. *Advanced Functional Materials*, 15(5), 739-744.
- [66] Onoe, H., & Takeuchi, S. (2008). Microfabricated mobile microplates for handling single adherent cells. *Journal of Micromechanics and Microengineering*, 18(9), 095003.
- [67] Yoshida, S., Teshima, T., Kuribayashi-Shigetomi, K., & Takeuchi, S. (2011). Single neural cells on mobile micro plates for precise neural network assembly. In *Proc. 15th International Conference on Miniaturized Systems for Chemistry and Life sciences* (pp. 1749-1751).
- [68] Gill, A. A., Ortega, Í., Kelly, S., & Claeysens, F. (2015). Towards the fabrication of artificial 3D microdevices for neural cell networks. *Biomedical microdevices*, 17(2), 27.
- [69] Liu, J., Cai, B., Zhu, J., Ding, G., Zhao, X., Yang, C., & Chen, D. (2004). Process research of high aspect ratio microstructure using SU-8 resist. *Microsystem Technologies*, 10(4), 265-268.
- [70] Teshima, T., Onoe, H., Kuribayashi - Shigetomi, K., Aonuma, H., Kamiya, K., Ishihara, H., ... & Takeuchi, S. (2014). Parylene mobile microplates integrated with an enzymatic release for handling of single adherent cells. *Small*, 10(5), 912-921.

- [71] Suri, S., & Schmidt, C. E. (2010). Cell-laden hydrogel constructs of hyaluronic acid, collagen, and laminin for neural tissue engineering. *Tissue Engineering Part A*, 16(5), 1703-1716.
- [72] Phillips, J. B., Bunting, S. C., Hall, S. M., & Brown, R. A. (2005). Neural tissue engineering: a self-organizing collagen guidance conduit. *Tissue engineering*, 11(9-10), 1611-1617.
- [73] Li, M., Guo, Y., Wei, Y., MacDiarmid, A. G., & Lelkes, P. I. (2006). Electrospinning polyaniline-contained gelatin nanofibers for tissue engineering applications. *Biomaterials*, 27(13), 2705-2715.
- [74] Nicodemus, G. D., & Bryant, S. J. (2008). Cell encapsulation in biodegradable hydrogels for tissue engineering applications. *Tissue Engineering Part B: Reviews*, 14(2), 149-165.
- [75] Cheng, T. Y., Chen, M. H., Chang, W. H., Huang, M. Y., & Wang, T. W. (2013). Neural stem cells encapsulated in a functionalized self-assembling peptide hydrogel for brain tissue engineering. *Biomaterials*, 34(8), 2005-2016.
- [76] Knippers, J., & Speck, T. (2012). Design and construction principles in nature and architecture. *Bioinspiration & biomimetics*, 7(1), 015002.
- [77] Fratzl, P. (2007). Biomimetic materials research: what can we really learn from nature's structural materials?. *Journal of the Royal Society Interface*, 4(15), 637-642.
- [78] Trask, R. S., & Bond, I. P. (2006). Biomimetic self-healing of advanced composite structures using hollow glass fibres. *Smart Materials and Structures*, 15(3), 704.
- [79] Sleytr, U. B., Messner, P., Pum, D., & Sára, M. (1999). Crystalline bacterial cell surface layers (S layers): from supramolecular cell structure to biomimetics and nanotechnology. *Angewandte Chemie International Edition*, 38(8), 1034-1054.
- [80] Turner, M. D., Schröder-Turk, G. E., & Gu, M. (2011). Fabrication and characterization of three-dimensional biomimetic chiral composites. *Optics Express*, 19(10), 10001-10008.

-
- [81] Bronzino, J. D., & Peterson, D. R. (2015). *The Biomedical Engineering Handbook: Four Volume Set*. CRC press.
- [82] Kalyanasundaram, K., & Graetzel, M. (2010). Artificial photosynthesis: biomimetic approaches to solar energy conversion and storage. *Current opinion in Biotechnology*, 21(3), 298-310.
- [83] Zhang, M., Hou, C., Halder, A., Wang, H., & Chi, Q. (2017). Graphene papers: smart architecture and specific functionalization for biomimetics, electrocatalytic sensing and energy storage. *Materials Chemistry Frontiers*, 1(1), 37-60.
- [84] Gan, Z., Turner, M. D., & Gu, M. (2016). Biomimetic gyroid nanostructures exceeding their natural origins. *Science Advances*, 2(5), e1600084.
- [85] Benyus, J. M. (1997). *Biomimicry: Innovation inspired by nature*.
- [86] Gruber, P., Bruckner, D., Hellmich, C., Schmiedmayer, H. B., Stachelberger, H., & Gebeshuber, I. C. (Eds.). (2011). *Biomimetics-Materials, Structures and Processes: Examples, Ideas and Case Studies*. Springer Science & Business Media.
- [87] Hu, Y., Lao, Z., Cumming, B. P., Wu, D., Li, J., Liang, H., ... & Gu, M. (2015). Laser printing hierarchical structures with the aid of controlled capillary-driven self-assembly. *Proceedings of the National Academy of Sciences*, 112(22), 6876-6881.
- [88] Thekkekara, L. V., & Gu, M. (2017). Bioinspired fractal electrodes for solar energy storages. *Scientific reports*, 7, 45585.
- [89] Jang, D., Meza, L. R., Greer, F., & Greer, J. R. (2013). Fabrication and deformation of three-dimensional hollow ceramic nanostructures. *Nature materials*, 12(10), 893.
- [90] Aldersey-Williams, H. (2004). Towards biomimetic architecture. *Nature materials*, 3(5), 277.
- [91] Ashby, M. F., & Medalist, R. M. (1983). The mechanical properties of cellular solids. *Metallurgical Transactions A*, 14(9), 1755-1769.

- [92] Khaderi, S. N., Deshpande, V. S., & Fleck, N. A. (2014). The stiffness and strength of the gyroid lattice. *International Journal of Solids and Structures*, 51(23-24), 3866-3877.
- [93] Deshpande, V. S., Fleck, N. A., & Ashby, M. F. (2001). Effective properties of the octet-truss lattice material. *Journal of the Mechanics and Physics of Solids*, 49(8), 1747-1769.
- [94] Han, Lee, et al. "A new type of low-density material: shellular." *Advanced Materials*, (2015): 27(37), 5506-5511.
- [95] Bauer, J., Hengsbach, S., Tesari, I., Schwaiger, R., & Kraft, O. (2014). High-strength cellular ceramic composites with 3D microarchitecture. *Proceedings of the National Academy of Sciences*, 111(7), 2453-2458.
- [96] Meza, L. R., Das, S., & Greer, J. R. (2014). Strong, lightweight, and recoverable three-dimensional ceramic nanolattices. *Science*, 345(6202), 1322-1326.
- [97] Meza, L. R., Philipot, G. P., Portela, C. M., Maggi, A., Montemayor, L. C., Comella, A., ... & Greer, J. R. (2017). Reexamining the mechanical property space of three-dimensional lattice architectures. *Acta Materialia*, 140, 424-432.
- [98] Thekkekara, L. V., Jia, B., Zhang, Y., Qiu, L., Li, D., & Gu, M. (2015). On-chip energy storage integrated with solar cells using a laser scribed graphene oxide film. *Applied Physics Letters*, 107(3), 031105.
- [99] Maruo, S., Nakamura, O., & Kawata, S. (1997). Three-dimensional microfabrication with two-photon-absorbed photopolymerization. *Optics letters*, 22(2), 132-134.
- [100] Cao, Y., Gan, Z., Jia, B., Evans, R. A., & Gu, M. (2011). High-photosensitive resin for super-resolution direct-laser-writing based on photoinhibited polymerization. *Optics express*, 19(20), 19486-19494.
- [101] Yu, Y., Fu, F., Shang, L., Cheng, Y., Gu, Z., & Zhao, Y. (2017). Bioinspired helical microfibers from microfluidics. *Advanced Materials*, 29(18), 1605765.
- [102] Wong, S., Deubel, M., Pérez - Willard, F., John, S., Ozin, G. A., Wegener, M., & von Freymann, G. (2006). Direct laser writing of three-dimensional

- photonic crystals with a complete photonic bandgap in chalcogenide glasses. *Advanced materials*, 18(3), 265-269.
- [103] Cumming, B. P., Jesacher, A., Booth, M. J., Wilson, T., & Gu, M. (2011). Adaptive aberration compensation for three-dimensional micro-fabrication of photonic crystals in lithium niobate. *Optics express*, 19(10), 9419-9425.
- [104] Cumming, B. P., Turner, M. D., Schröder-Turk, G. E., Debbarma, S., Luther-Davies, B., & Gu, M. (2014). Adaptive optics enhanced direct laser writing of high refractive index gyroid photonic crystals in chalcogenide glass. *Optics express*, 22(1), 689-698.
- [105] Tabrizi, S., Cao, Y., Cumming, B. P., Jia, B., & Gu, M. (2016). Functional optical plasmonic resonators fabricated via highly photosensitive direct laser reduction. *Advanced Optical Materials*, 4(4), 529-533.
- [106] Xing, J. F., Dong, X. Z., Chen, W. Q., Duan, X. M., Takeyasu, N., Tanaka, T., & Kawata, S. (2007). Improving spatial resolution of two-photon microfabrication by using photoinitiator with high initiating efficiency. *Applied physics letters*, 90(13), 131106.
- [107] Kawata, S., Sun, H. B., Tanaka, T., & Takada, K. (2001). Finer features for functional microdevices. *Nature*, 412(6848), 697.
- [108] Malinauskas, M., Farsari, M., Piskarskas, A., & Juodkazis, S. (2013). Ultrafast laser nanostructuring of photopolymers: A decade of advances. *Physics Reports*, 533(1), 1-31.
- [109] Fischer, J., & Wegener, M. (2013). Three-dimensional optical laser lithography beyond the diffraction limit. *Laser & Photonics Reviews*, 7(1), 22-44.
- [110] Fourkas, J. T., & Petersen, J. S. (2014). 2-Colour photolithography. *Physical Chemistry Chemical Physics*, 16(19), 8731-8750.
- [111] Paz, V. F., Emons, M., Obata, K., Ovsianikov, A., Peterhänsel, S., Frenner, K., ... & Osten, W. (2012). Development of functional sub-100 nm structures with 3D two-photon polymerization technique and optical methods for characterization. *Journal of Laser Applications*, 24(4), 042004.

- [112] Fischer, J., & Wegener, M. (2013). Three-dimensional optical laser lithography beyond the diffraction limit. *Laser & Photonics Reviews*, 7(1), 22-44.
- [113] Wegener M. (2017) 3D Optical Laser Lithography. In: Di Bartolo B., Collins J., Silvestri L. (eds) *Nano-Optics: Principles Enabling Basic Research and Applications*. NATO Science for Peace and Security Series B: Physics and Biophysics. Springer, Dordrecht.
- [114] Serbin, J., & Gu, M. (2006). Experimental evidence for superprism effects in three-dimensional polymer photonic crystals. *Advanced materials*, 18(2), 221-224.
- [115] Staude, I., Thiel, M., Essig, S., Wolff, C., Busch, K., Von Freymann, G., & Wegener, M. (2010). Fabrication and characterization of silicon woodpile photonic crystals with a complete bandgap at telecom wavelengths. *Optics letters*, 35(7), 1094-1096.
- [116] Thiel, M., Rill, M. S., von Freymann, G., & Wegener, M. (2009). Three-dimensional bi-chiral photonic crystals. *Advanced Materials*, 21(46), 4680-4682.
- [117] Sun, H. B., Tanaka, T., & Kawata, S. (2002). Three-dimensional focal spots related to two-photon excitation. *Applied Physics Letters*, 80(20), 3673-3675.
- [118] Ovsianikov, A., Viertl, J., Chichkov, B., Oubaha, M., MacCraith, B., Sakellari, I., ... & Fotakis, C. (2008). Ultra-low shrinkage hybrid photosensitive material for two-photon polymerization microfabrication. *Acs Nano*, 2(11), 2257-2262.
- [119] Ovsianikov, A., Shizhou, X., Farsari, M., Vamvakaki, M., Fotakis, C., & Chichkov, B. N. (2009). Shrinkage of microstructures produced by two-photon polymerization of Zr-based hybrid photosensitive materials. *Optics Express*, 17(4), 2143-2148.
- [120] Deubel, M., Von Freymann, G., Wegener, M., Pereira, S., Busch, K., & Soukoulis, C. M. (2004). Direct laser writing of three-dimensional photonic-crystal templates for telecommunications. *Nature materials*, 3(7), 444.

- [121] Thiel, M., Decker, M., Deubel, M., Wegener, M., Linden, S., & von Freymann, G. (2007). Polarization Stop Bands in Chiral Polymeric Three - Dimensional Photonic Crystals. *Advanced Materials*, 19(2), 207-210.
- [122] Li, Y., Qi, F., Yang, H., Gong, Q., Dong, X., & Duan, X. (2008). Nonuniform shrinkage and stretching of polymerized nanostructures fabricated by two-photon photopolymerization. *Nanotechnology*, 19(5), 055303.
- [123] Sun, H. B., Suwa, T., Takada, K., Zaccaria, R. P., Kim, M. S., Lee, K. S., & Kawata, S. (2004). Shape precompensation in two-photon laser nanowriting of photonic lattices. *Applied physics letters*, 85(17), 3708-3710.
- [124] Wu, D., Fang, N., Sun, C., & Zhang, X. (2006). Stiction problems in releasing of 3D microstructures and its solution. *Sensors and Actuators A: Physical*, 128(1), 109-115.
- [125] Hell, S. W., & Wichmann, J. (1994). Breaking the diffraction resolution limit by stimulated emission: stimulated-emission-depletion fluorescence microscopy. *Optics letters*, 19(11), 780-782.
- [126] Li, L., Gattass, R. R., Gershgoren, E., Hwang, H., & Fourkas, J. T. (2009). Achieving $\lambda/20$ resolution by one-color initiation and deactivation of polymerization. *Science*, 324(5929), 910-913.
- [127] Scott, T. F., Kowalski, B. A., Sullivan, A. C., Bowman, C. N., & McLeod, R. R. (2009). Two-color single-photon photoinitiation and photoinhibition for subdiffraction photolithography. *Science*, 324(5929), 913-917.
- [128] Andrew, T. L., Tsai, H. Y., & Menon, R. (2009). Confining light to deep subwavelength dimensions to enable optical nanopatterning. *Science*, 324(5929), 917-921.
- [129] Gan, Z., Cao, Y., Evans, R. A., & Gu, M. (2013). Three-dimensional deep sub-diffraction optical beam lithography with 9 nm feature size. *Nature communications*, 4, 2061.
- [130] Cumming, B. P., Debbarma, S., Luther-Davis, B., & Gu, M. (2013). Simultaneous compensation for aberration and axial elongation in three-

- dimensional laser nanofabrication by a high numerical-aperture objective. *Optics express*, 21(16), 19135-19141.
- [131] Jesacher, A., Marshall, G. D., Wilson, T., & Booth, M. J. (2010). Adaptive optics for direct laser writing with plasma emission aberration sensing. *Optics express*, 18(2), 656-661.
- [132] Goi, E., Cumming, B., & Gu, M. (2018). Impact of Cubic Symmetry on Optical Activity of Dielectric 8-srs Networks. *Applied Sciences*, 8(11), 2104.
- [133] Pruzinsky, S. A., & Braun, P. V. (2005). Fabrication and Characterization of Two-Photon Polymerized Features in Colloidal Crystals. *Advanced Functional Materials*, 15(12), 1995-2004.
- [134] Kato, J. I., Takeyasu, N., Adachi, Y., Sun, H. B., & Kawata, S. (2005). Multiple-spot parallel processing for laser micronanofabrication. *Applied physics letters*, 86(4), 044102.
- [135] Mills, B., Grant-Jacob, J. A., Feinaeugle, M., & Eason, R. W. (2013). Single-pulse multiphoton polymerization of complex structures using a digital multimirror device. *Optics express*, 21(12), 14853-14858.
- [136] Lin, H., Jia, B., & Gu, M. (2011). Dynamic generation of Debye diffraction-limited multifocal arrays for direct laser printing nanofabrication. *Optics letters*, 36(3), 406-408.
- [137] Li, X., Cao, Y., Tian, N., Fu, L., & Gu, M. (2015). Multifocal optical nanoscopy for big data recording at 30 TB capacity and gigabits/second data rate. *Optica*, 2(6), 567-570.
- [138] Blasco, E., Müller, J., Müller, P., Trouillet, V., Schön, M., Scherer, T., ... & Wegener, M. (2016). Fabrication of Conductive 3D Gold-Containing Microstructures via Direct Laser Writing. *Advanced Materials*, 28(18), 3592-3595.
- [139] Zhang, Y., Guo, L., Wei, S., He, Y., Xia, H., Chen, Q., ... & Xiao, F. S. (2010). Direct imprinting of microcircuits on graphene oxides film by femtosecond laser reduction. *Nano today*, 5(1), 15-20.

- [140] Fu, F., Chen, Z., Zhao, Z., Wang, H., Shang, L., Gu, Z., & Zhao, Y. (2017). Bio-inspired self-healing structural color hydrogel. *Proceedings of the National Academy of Sciences*, 114(23), 5900-5905.
- [141] Xie, Z., Li, L., Liu, P., Zheng, F., Guo, L., Zhao, Y., ... & Gu, Z. (2015). Self-Assembled Coffee-Ring Colloidal Crystals for Structurally Colored Contact Lenses. *Small*, 11(8), 926-930.
- [142] Campagnola, P. J., Delguidice, D. M., Epling, G. A., Hoffacker, K. D., Howell, A. R., Pitts, J. D., & Goodman, S. L. (2000). 3-dimensional submicron polymerization of acrylamide by multiphoton excitation of xanthene dyes. *Macromolecules*, 33(5), 1511-1513.
- [143] Dietliker, K., Hüsler, R., Birbaum, J. L., & Wolf, J. P. (2010). U.S. Patent No. 7,732,504. Washington, DC: U.S. Patent and Trademark Office.
- [144] Bahney, C. S., Lujan, T. J., Hsu, C. W., Bottlang, M., West, J. L., & Johnstone, B. (2011). Visible light photoinitiation of mesenchymal stem cell-laden bioresponsive hydrogels. *European cells & materials*, 22, 43.
- [145] Ovsianikov, A., Mironov, V., Stampfl, J., & Liska, R. (2012). Engineering 3D cell-culture matrices: multiphoton processing technologies for biological and tissue engineering applications. *Expert review of medical devices*, 9(6), 613-633.
- [146] Li, Z., Torgersen, J., Ajami, A., Mühleder, S., Qin, X., Husinsky, W., ... & Liska, R. (2013). Initiation efficiency and cytotoxicity of novel water-soluble two-photon photoinitiators for direct 3D microfabrication of hydrogels. *Rsc Advances*, 3(36), 15939-15946.
- [147] Jang, T. S., Jung, H. D., Pan, M. H., Han, W. T., Chen, S., & Song, J. (2018). 3D printing of hydrogel composite systems: Recent advances in technology for tissue engineering.
- [148] Accardo, A., Blatché, M. C., Courson, R., Loubinoux, I., Vieu, C., & Malaquin, L. (2018). Two-photon lithography and microscopy of 3D hydrogel scaffolds for neuronal cell growth. *Biomedical Physics & Engineering Express*, 4(2), 027009.

- [149] Selimis, A., Mironov, V., & Farsari, M. (2015). Direct laser writing: Principles and materials for scaffold 3D printing. *Microelectronic Engineering*, 132, 83-89.
- [151] Ajeti, V., Lien, C. H., Chen, S. J., Su, P. J., Squirrell, J. M., Molinarolo, K. H., ... & Campagnola, P. J. (2013). Image-inspired 3D multiphoton excited fabrication of extracellular matrix structures by modulated raster scanning. *Optics Express*, 21(21), 25346-25355.
- [152] Klein, F., Striebel, T., Fischer, J., Jiang, Z., Franz, C. M., von Freymann, G., ... & Bastmeyer, M. (2010). Elastic Fully Three-dimensional Microstructure Scaffolds for Cell Force Measurements. *Advanced materials*, 22(8), 868-871.
- [153] Merz, M., & Fromherz, P. (2002). Polyester microstructures for topographical control of outgrowth and synapse formation of snail neurons. *Advanced Materials*, 14(2), 141-144.
- [154] Fromherz, P. (2006). Three levels of neuroelectronic interfacing. *Annals of the New York Academy of Sciences*, 1093(1), 143-160.
- [155] Lozano, R., Stevens, L., Thompson, B. C., Gilmore, K. J., Gorkin III, R., Stewart, E. M., ... & Wallace, G. G. (2015). 3D printing of layered brain-like structures using peptide modified gellan gum substrates. *Biomaterials*, 67, 264-273.
- [156] McDougal, R. A., & Shepherd, G. M. (2015). 3D-printer visualization of neuron models. *Frontiers in neuroinformatics*, 9, 18.
- [157] Berdichevsky, Y., Staley, K. J., & Yarmush, M. L. (2010). Building and manipulating neural pathways with microfluidics. *Lab on a Chip*, 10(8), 999-1004.
- [158] Roth, S., Bisbal, M., Brocard, J., Bugnicourt, G., Saoudi, Y., Andrieux, A., ... & Villard, C. (2012). How morphological constraints affect axonal polarity in mouse neurons. *PloS one*, 7(3), e33623.
- [159] Kleinfeld, D., Kahler, K. H., & Hockberger, P. E. (1988). Controlled outgrowth of dissociated neurons on patterned substrates. *Journal of Neuroscience*, 8(11), 4098-4120.

- [160] Dermutz, H., Grüter, R. R., Truong, A. M., Demkó, L., Vörös, J., & Zambelli, T. (2014). Local polymer replacement for neuron patterning and in situ neurite guidance. *Langmuir*, 30(23), 7037-7046.
- [161] Yi, Y., Park, J., Lim, J., Lee, C. J., & Lee, S. H. (2015). Central nervous system and its disease models on a chip. *Trends in biotechnology*, 33(12), 762-776.
- [162] D'avanzo, C., Aronson, J., Kim, Y. H., Choi, S. H., Tanzi, R. E., & Kim, D. Y. (2015). Alzheimer's in 3D culture: challenges and perspectives. *Bioessays*, 37(10), 1139-1148.
- [163] Hasan, M., & Berdichevsky, Y. (2016). Neural circuits on a chip. *Micromachines*, 7(9), 157.
- [164] Rah, J. C., Feng, L., Druckmann, S., Lee, H., & Kim, J. (2015). From a meso- to micro-scale connectome: array tomography and mGRASP. *Frontiers in neuroanatomy*, 9, 78.
- [165] Sporns, O., Tononi, G., & Kötter, R. (2005). The human connectome: a structural description of the human brain. *PLoS computational biology*, 1(4), e42.
- [166] Straub, M., & Gu, M. (2002). Near-infrared photonic crystals with higher-order bandgaps generated by two-photon photopolymerization. *Optics letters*, 27(20), 1824-1826.
- [167] Gan, Z., Cao, Y., Evans, R. A., & Gu, M. (2013). Three-dimensional deep sub-diffraction optical beam lithography with 9 nm feature size. *Nature communications*, 4, 2061.
- [168] Schmidt, V., & Belegatis, M. (2016). *Laser technology in biomimetics*. Springer-Verlag Berlin An.
- [169] Yu, H., Zhang, Q., & Gu, M. (2018). Three-dimensional direct laser writing of biomimetic neuron structures. *Optics express*, 26(24), 32111-32117.
- [170] Stam, C. J., Van Straaten, E. C. W., Van Dellen, E., Tewarie, P., Gong, G., Hillebrand, A., ... & Van Mieghem, P. (2016). The relation between structural

- and functional connectivity patterns in complex brain networks. *International Journal of Psychophysiology*, 103, 149-160.
- [171] Yang, S. A., Yoon, J., Kim, K., & Park, Y. (2017). Measurements of morphological and biophysical alterations in individual neuron cells associated with early neurotoxic effects in Parkinson's disease. *Cytometry part A*, 91(5), 510-518.
- [172] Engelbrecht, A. P. (2007). *Computational intelligence: an introduction*. John Wiley & Sons.
- [173] Markram, H. (2013). Seven challenges for neuroscience. *Functional neurology*, 28(3), 145.
- [174] Sengupta, B., & Stemmler, M. B. (2014). Power consumption during neuronal computation. *Proceedings of the IEEE*, 102(5), 738-750.
- [175] Cuntz, H., Forstner, F., Borst, A., & Häusser, M. (2010). One rule to grow them all: a general theory of neuronal branching and its practical application. *PLoS computational biology*, 6(8), e1000877.
- [176] DeFelipe, J. (2015). The anatomical problem posed by brain complexity and size: a potential solution. *Frontiers in neuroanatomy*, 9, 104.
- [177] Guidolin, D., Tortorella, C., De Caro, R., & Agnati, L. F. (2016). Does a Self-Similarity Logic Shape the Organization of the Nervous System? In *the Fractal Geometry of the Brain* (pp. 137-156). Springer, New York, NY.
- [178] Schierwagen, A. (2008). Neuronal morphology: Shape characteristics and models. *Neurophysiology*, 40(4), 310-315.
- [179] Isaeva, V. V., Pushchina, E. V., & Karetin, Y. A. (2004). The quasi-fractal structure of fish brain neurons. *Russian Journal of Marine Biology*, 30(2), 127-134.
- [180] Chklovskii, D. B. (2004). Synaptic connectivity and neuronal morphology: two sides of the same coin. *Neuron*, 43(5), 609-617.
- [181] Groves, T. R., Wang, J., Boerma, M., & Allen, A. R. (2017). Assessment of hippocampal dendritic complexity in aged mice using the Golgi-cox method. *Journal of visualized experiments: JoVE*, (124).

- [182] Hu, Y., Lao, Z., Cumming, B. P., Wu, D., Li, J., Liang, H., ... & Gu, M. (2015). Laser printing hierarchical structures with the aid of controlled capillary-driven self-assembly. *Proceedings of the National Academy of Sciences*, 112(22), 6876-6881.
- [183] DeSimone, J. M. (2002). Practical approaches to green solvents. *Science*, 297(5582), 799-803.
- [184] Zhou, X., Hou, Y., & Lin, J. (2015). A review on the processing accuracy of two-photon polymerization. *AIP Advances*, 5(3), 030701.
- [185] Martineau, C., Anémian, R., Andraud, C., Wang, I., Bouriau, M., & Baldeck, P. L. (2002). Efficient initiators for two-photon induced polymerization in the visible range. *Chemical physics letters*, 362(3-4), 291-295.
- [186] https://it.wikipedia.org/wiki/Jakob_Steiner
- [187] Brazil, M., Graham, R. L., Thomas, D. A., & Zachariasen, M. (2014). On the history of the Euclidean Steiner tree problem. *Archive for history of exact sciences*, 68(3), 327-354.
- [188] Zelikovsky, A. Z. (1992). An 11/6-approximation algorithm for the Steiner problem on graphs. In *Annals of Discrete Mathematics (Vol. 51, pp. 351-354)*. Elsevier.
- [189] Turner, M. D., Saba, M., Zhang, Q., Cumming, B. P., Schröder-Turk, G. E., & Gu, M. (2012, October). Fabrication and characterisation of chiral beamsplitters via galvo-dithered direct laser writing. In *Frontiers in Optics (pp. FW1F-3)*. Optical Society of America.
- [190] Ding, H., Zhang, Q., Gu, Z., & Gu, M. (2018). 3D computer-aided nanoprinting for solid-state nanopores. *Nanoscale Horizons*, 3(3), 312-316.
- [191] Turner, M. D. (2013). Biomimetic chiral gyroids for photonic microstructures.
- [192] Ding, H., Zhang, Q., Gu, Z., & Gu, M. (2017, September). Two-Photon Polymerization of Biocompatible Hydrogels. In *Frontiers in Optics (pp. FTu5B-3)*. Optical Society of America.

- [193] Sheik-Bahae, M., Said, A. A., Wei, T. H., Hagan, D. J., & Van Stryland, E. W. (1990). Sensitive measurement of optical nonlinearities using a single beam. *IEEE journal of quantum electronics*, 26(4), 760-769.
- [194] Liu, M., Zeng, G., Wang, K., Wan, Q., Tao, L., Zhang, X., & Wei, Y. (2016). Recent developments in polydopamine: an emerging soft matter for surface modification and biomedical applications. *Nanoscale*, 8(38), 16819-16840.
- [195] Nayfeh, A. H., & Pai, P. F. (2008). *Linear and nonlinear structural mechanics*. John Wiley & Sons.
- [196] Ganji, F., Vasheghani, F. S., & VASHEGHANI, F. E. (2010). Theoretical description of hydrogel swelling: a review.
- [197] Sherman, T. F. (1981). On connecting large vessels to small. The meaning of Murray's law. *The Journal of general physiology*, 78(4), 431-453.
- [198] Cao, Y., Gan, Z., Jia, B., Evans, R. A., & Gu, M. (2011). High-photosensitive resin for super-resolution direct-laser-writing based on photoinhibited polymerization. *Optics express*, 19(20), 19486-19494.
- [199] Gan, Z., Cao, Y., Evans, R. A., & Gu, M. (2013). Three-dimensional deep sub-diffraction optical beam lithography with 9 nm feature size. *Nature communications*, 4, 2061.

Author's Publications

Journal Publications

1. **Haoyi Yu**, Qiming Zhang, & Min Gu. Three-dimensional direct laser writing of biomimetic neuron structures. *Optics express*, 26(24), 32111-32117 (2018).
2. Qiming Zhang, **Haoyi Yu**, Martina Barbiero, Baokai Wang and Min Gu. Artificial neural networks enabled by nanophotonics. *Light: Science & Applications*, 8(1), 42 (2019).
3. **Haoyi Yu**, Qiming Zhang, & Min Gu. Neuron-inspired 3D Steiner tree network structures and the mechanical property study. (In preparation)
4. **Haoyi Yu**, Haibo Ding, Qiming Zhang, Zhongze Gu & Min Gu. Two-photon direct laser writing of biocompatible hydrogel material. (In preparation)

Conference Publications

1. **Haoyi Yu**, Qiming Zhang, Zengji Yue, & Min Gu. Three-dimensional direct laser writing of neuron-inspired structures. In *Frontiers in Optics* (pp. FTu5D-2). Optical Society of America. (2017)
2. **Haoyi Yu**, Qiming Zhang, & Min Gu. Three-dimensional Direct Laser Writing of Ultra-Low-Density Neuron-inspired Steiner Tree Structures. In *Frontiers in Optics* (pp. FM3D-2). Optical Society of America. (2018)
3. **Haoyi Yu**, Qiming Zhang, & Min Gu. Three-dimensional Direct Laser Writing of Ultra-Low-Density Neuron-inspired Steiner Tree Structures. *23rd Australian Institute of Physics Congress*. (2018)
4. **Haoyi Yu**, Wei Shao, Qiming Zhang, Flora D Salim & Min Gu. Deep-Learning-aided three-dimensional direct laser writing of the complete connectome of mushroom body from an insect brain. *CLEO/Europe-EQEC 2019*. European Physical Society. (2019)

Author's Awards

1. Finalist of the Emil Wolf Student Paper Competition (2018). This award recognises innovation, research and presentation excellence of students presenting their work during Frontiers in Optics (FiO) by Optical Society of America.
2. IONS KOALA Travel Grant (2017). Sponsored by The Optical Society (OSA) to honour PhD students' innovation, research and presentation excellence in presenting their work during the IONS KOALA conference.
3. IONS KOALA Travel Grant (2018). Sponsored by The Optical Society (OSA) to honour PhD students' innovation, research and presentation excellence in presenting their work during the IONS KOALA conference.

